NANOPARTICLE-COATED POLY(3-HYDROXYBUTYRATE) GRANULES FOR BIOMEDICAL APPLICATIONS

A Dissertation

Presented to the Faculty of the Graduate School

of Cornell University

In Partial Fulfillment of the Requirements for the Degree of

Doctor of Philosophy

by

Diego Rey

August 2012

NANOPARTICLE-COATED POLY(3-HYDROXYBUTYRATE) GRANULES FOR BIOMEDICAL APPLICATIONS

Diego Rey, Ph. D.

Cornell University 2012

Poly(3-hydroxybutyrate) (PHB) is a biodegradable and biocompatible polymer produced by many bacteria as a stored carbon source. Recent reviews have recently recognized PHB granules as a biomaterial that can be functionalized for use in various biomedical applications. The studies in this dissertation describe a novel means of producing nanoparticle-coated PHB granules that expands the capabilities of functionalized PHB granules through harnessing versatile properties of inorganic nanoparticles.

PHA synthase was conjugated to gold nanoparticles (AuNP) and superparamagnetic iron oxide nanoparticles (SPION) and upon the addition of 3-hydroxybutyrate-CoA (3HB-CoA), these nanoparticle-PHA synthase conjugates produce poly(3-hydroxybutyrate) (PHB) which aggregate to form nano- to micron-sized nanoparticle-coated PHB granules. The resulting nanoparticle-polymer hybrid-materials are shown to exhibit unique properties to those of PHB and the nanoparticles alone and are a result of the rearrangement of the nanoparticles on the PHB granule surface.

SPION-coated PHB granules are potential enhanced MRI contrast agents exhibiting ~2-fold improvement in spin-spin (T2) relaxivity (168 s^{-1} $mmol^{-1}$ Fe) when compared to free SPION conjugated to PHA synthase (87.5 s^{-1} $mmol^{-1}$ Fe). Control of the SPION-coated PHB granule size is also demonstrated via the addition of the

surfactant Tween 20 that allows for producing PHB granules as small as 100 nm in diameter offering the possibility of controlling their biodistribution. Furthermore, SPION-PHA synthase is shown to also allow for controlled retention of SPION within porous matrices via PHB polymerization where *in situ* polymerization of PHB from SPION-PHA synthase within agarose gel was shown retain up to 4.2-times greater amount of SPION when compared to SPION-PHA synthase samples that did not undergo polymerization.

Similarly, gold nanoparticle-coated PHB granules also exhibit unique properties that may be suitable in biomedical applications. AuNP-coated PHB granules are potential theranostic agents that have enhanced imaging capabilities, including surface-enhanced Raman scattering (SERS) and enhanced fluorescence, and can generate localized heating upon near-infrared (NIR) laser irradiation. The AuNP-coated PHB exhibited 11-fold enhancement in SERS over AuNP-PHA synthase particles prior polymerization. In addition, AuNP-coated PHB stained with the fluorophore Nile red exhibited a 6-fold enhancement in fluorescence intensity as well as a 1.3-fold decrease in photobleaching rate when compared to PHB granules alone. The granules were also shown to emit heat when illuminated at 808 nm with a 3.9-fold increase in heating rate when compared to AuNP-PHA synthase alone. In addition, NIR laser illumination of fluorescent doxorubicin (Dox)-loaded AuNP-PHB granules resulted in loss of fluorescence due to destruction of the PHB granule structure, providing a potential means of laser-triggered drug delivery from AuNP-PHB granules.

BIOGRAPHICAL SKETCH

Diego Rey was born in Bariloche, Argentina and came with his immediate family to the San Francisco Bay Area at the age of seven. What was to be a one-year trip to the U.S. turned into permanent residence and ultimately U.S. citizenship. Diego grew up in Palo Alto, CA and went on to earn his Bachelors of Science Degree in Electrical Engineering at the University of California at Santa Barbara. While at Santa Barbara, Diego was fortunate to participate in a Research Experience for Undergraduates program at Cornell for two consecutive summers. Drawn by his research experience at Cornell, nostalgic about the winters in Bariloche, and taking constant perfect weather for granted, Diego joined the Biomedical Engineering Ph.D. Program at Cornell in 2004, the year that Cornell's Biomedical Engineering Department was formed.

DEDICATION

To my parents who constantly provide me with the ultimate example in life and one that I strive to follow.

ACKNOWLEDGMENTS

Many individuals have contributed directly and indirectly to my thesis work and to my overall graduate school experience. These interactions are the most valuable aspect of my time at Cornell and of my path moving forward.

I first need to acknowledge Professor Carl Batt and the Batt Laboratory. There were two major aspects of the Batt Lab that made me want to join Carl's group. First, Carl has built a diverse and interdisciplinary team of students and postdocs creating an environment with a tremendous breadth of expertise under one roof – biology, chemistry, physics, and engineering blended together seamlessly in the Batt Lab. This provided an awesome learning environment. Second, Carl has a passion for education beyond the graduate program and reaching out to K-12 students including those in disadvantaged communities. This is a passion that I share and, in my opinion, this was an essential component to my graduate experience.

Throughout my experience in the Batt Lab it was always clear that Carl is most interested in the personal growth of his students creating an environment where this growth can be maximized. This is something that I am truly grateful for.

Many other individuals deserve full acknowledgement including – All members of my thesis committee: Professors Scott Blanchard, George Malliaras, and Emmanuel Giannelis – Fellow Batt Labbers: Kyle Anderson, Cameron Bardliving, Magnus Bergkvist, Parijat Bhatnagar, Nate Cady, Rishard Chen, Leonardo Damasceno, Soazig Delamare, Jeri Galvachin, Jack Huang, Ines López-calleja Díaz, Adam Lowe, Matt Kennedy, Dickson Kirui, Clarissa Lui, Sonny Mark, Andy Melnychenko, Brian Newton, Nutawee Niamsiri, Stephannie Parker, Denise Payne, Yajaira Sierra, Sofia Sotiropoulou, Scott Stelick, Aaron Strickland, and Leonardo Teixeira – Collaborators: Carlos Hipolito Villa and Freddy Enrique – and Friends: Claudia Villalta, Jason Springs, Abhishek Ramkumar, Tunde Babalola, and Satish

Degala. Finally, none of this would have been possible for me without the support of my mom Emma Rocchi, my dad Juan Carlos Rey, and my brother Javier Rey.

TABLE OF CONTENTS

LIST OF FIGURES

LIST OF TABLES

LIST OF ABBREVIATIONS

3HB	3-hydroxybutyrate
3HB-CoA	3-hydroxybutyryl coenzyme A
Au	gold
AuNP	gold nanoparticle
cc	cubic centimeters
CCD	charged coupled device
CoA	coenzyme A
DLS	dynamic light scattering
DMSO	dimethyl sulfoxide
DNA	deoxyribonucleic acid
DNTB	5,5'-dithiobis(2-nitrobenoic acid)
Dox	doxorubicin
EDC	1- ethyl-3-[3- dimethylaminopropyl] carbodiimide hydrochloride
ELISA	enzyme-linked immunosorbent assay
ESIP	enzymatic surface initiated polymerization
FACS	fluorescence-activated cell sorting
FDA	United States Food and Drug Administration
FOV	field of view
GAP	granule associated protein
hr	hour
ICP	inductively-coupled plasma
IgG	immunoglobulin G
IMAC	immobilized metal ion chromatography
IPTG	isopropyl β-D-1-thiogalactopyranoside

MEF	metal-enhanced fluorescence
MES	(2-(N-morpholino)ethanesulfonic acid)
min	minute
MOG	myelin oligodendrocyte glycoprotein
MR	magnetic resonance
MRI	magnetic resonance imaging
nd	not determined
NEX	number of excitations
NHS	NHydroxysulfosuccinimide
NIH	United States National Institutes of Health
Ni-NTA	nickel nitrilotriacetate
NIR	near-infrared
OD	optical density
PCR	polymerase chain reaction
PEG	polyethylene glycol
PHA	polyhydroxyalkanoate
PHB	poly(3-hydroxybutyrate)
PL-PEG-COOH	carboxy-terminated PEGylated phospholipid
R2	1/T2
RES	reticuloendothelial system
RPM	revolutions per minute
SARS-CoV	severe acute respiratory syndrome coronavirus
SDS-PAGE	sodium dodecyl sulfate polyacrylamide gel electrophoresis
SEC	size exclusion chromatography
sec	seconds
SEF	surface-enhanced fluorescence

SERS	surface-enhanced Raman scattering/spectroscopy
SPIO	superparamagnetic iron oxide
SPION	superparamagnetic iron oxide nanoparticle
SPR	surface plasmon resonance
T	tesla
T2	proton spin-spin relaxation time
TE	echo time
TEM	transmission electron microscopy
TR	repetition time

Chapter 1 – Background

1.1. Polyhydroxyalkanoates

Polyhydroxyalkanoates (PHAs) are polyesters that are synthesized from (R)-3-hydroxyacyl-CoA by many bacteria(*1-6*) under conditions of limited nutrients and excess carbon(*7-10*) for conditions of carbon starvation(*11, 12*) (Figure 1.1). The primary enzymes involved in PHA synthesis are PHA synthases accompanied by several granule associated proteins (GAPs) which are designated to four classes: PHA synthases, PHA depolymerases, regulatory proteins, and phasins. PHA is stored as granular inclusions in the cytoplasm and can make up over 80% of a bacteria's dry weight(*13*). Two predominant models for *in vivo* granule formation have been proposed(*14*) and the resulting granule structure has been characterized(*15*). Figure 1.2 depicts the general process of granule formation in which PHA synthase binds its substrate and then dimerizes before elongation of the PHA chain. Because PHA is water insoluble, polymerizing PHA synthase dimers exhibit an amphiphilic character and begin to coalesce via hydrophobic interactions between the polymer chains. This structure eventually takes a granular shape in which PHA synthase remains at the granule surface and continues polymerize PHA into the granule core. Available granule surface provides docking space for other GAPs which are regulated based on their affinity to the granule surface and the space available on the granule surface for their binding(*16*).

At least 91 different repeat units occur in PHAs(*17*), and over 90 genera of bacteria, both Gram-negative and Gram-positive, have been found that produce PHA(*18*). Among the most common PHAs is poly(3-hydroxybutyrate) (PHB) that is formed by PHA synthase from the substrate 3-hydroxybutyryl coenzyme A (3HB-CoA) and whose side chain (R in Figure 1.1) is a methyl group.

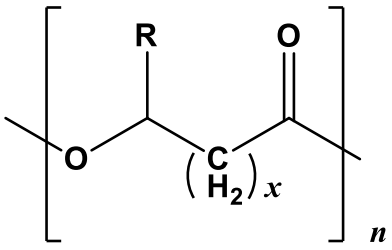

R = H, CH_3, C_2H_5, C_3H_7 – $C_{13}H_{27}$

***x* = 1 – 4**

Figure 1.1: Polyhydroxyalkanoates formula

Among polyhydroxyalkanoates (PHAs), poly(3-hydroxybutyrate) (PHB) is the most common. For PHB, R = CH_3 and x = 1. The molecular weight of in vitro polymerized PHB is on the order of 12 MDa(19), i.e. n ~ 141042.

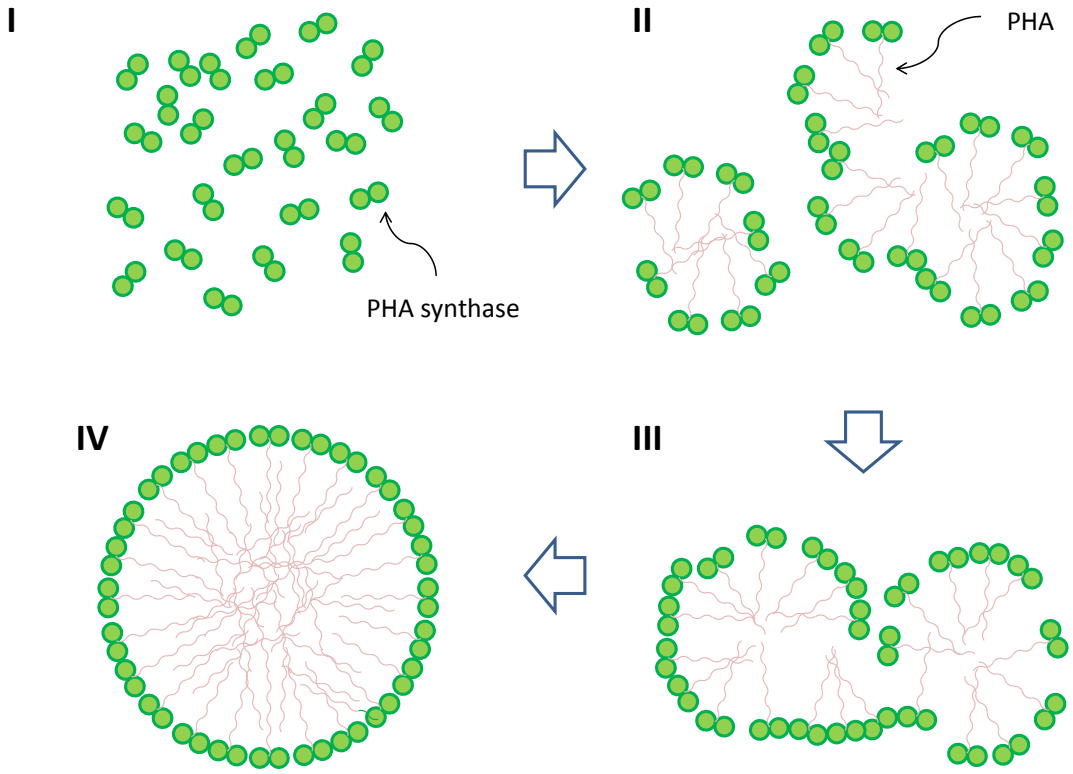

Figure 1.2: Model for *in vitro* PHA granule formation

(I) PHA synthase binds its substrate and then dimerizes before (II) elongation of the PHA chain. Because PHA is water insoluble, polymerizing PHA synthase dimers exhibit an amphiphilic character causing them to aggregate via hydrophobic interactions between the polymer chains. The resulting structures eventually take a granular shape (III) stabilized by PHA synthase that remains on their surface. Collisions between these nascent granules cause them to combine resulting in the formation of mature granules (IV) where PHA synthase on the surface of the granule continues polymerize PHA into the granule core(14, 15).

PHAs have drawn considerable attention as a potential substitutes for petrochemical-based plastics(*18*). Much effort has focused on tailoring the physical properties of bulk PHA-based plastics to match those of commodity materials such as polypropylene through modifying PHA synthase(*20, 21*), tailoring substrates(*21*), and incorporating additives(*22, 23*). Commercial efforts to commoditize PHA-based materials are well under way(*24*).

1.2. PHB biodegradation and biocompatibility

PHAs degrade to water and carbon dioxide in the environment via hydrolysis(*25*). *In vivo*, initial degradation has been shown to be caused by hydrolysis followed by macrophage-induced enzymatic attack(*26*). PHB degrades to (D)-3-hydroxybutyric acid *in vivo*, which is a constituent of human blood(*27*). (DL)-3-hydroxybutyrate has even been used as a nutritional supplement for obese subjects on low-energy diets or undergoing therapeutic starvation(*28*). Administration of PHB *in vivo* has shown low toxicity and in fact, PHB itself has been found to be a ubiquitous component in human blood(*29*). Several studies have investigated cell interactions with solvent-cast PHB both in animals and in animal cell cultures and have shown favorable biocompatibility of the material(*30-32*). In our laboratory's own studies, Niamsiri, et al. observed the biocompatible properties of surface polymerized PHB using mouse embryonic fibroblast cells(*33*). In these studies, PHB was shown to promote cell attachment and growth when compared to unmodified planar gold surfaces.

Overall, studies have shown that PHAs perform favorably in clinical applications(*34*). These studies have demonstrated the biocompatibility of PHAs and the polymers are now being incorporated in products such as sutures, bandages, and implants(*35*).

1.3. PHB granules

Recently, the use of PHB in its granule form has emerged as a promising new nanoparticle for biomedical applications and these advances have been recently reviewed(*15*). Thus far, most of PHB granule functionalization strategies have employed *in vivo* self-assembly using GAP-fusion constructs(*36-45*) or modification of the granule post-synthesis where either extracted *in vivo* produced granules were directly modified with GAP-tagged proteins or extracted PHB bulk material was used to produce synthetic PHB beads that were then modified with GAP-tagged proteins(*46-49*). An additional avenue for developing functional PHB nanoparticles employed chemical addition of functional groups to the PHB polymer chain of extracted PHB(*50, 51*). Furthermore, because PHA synthase is the only GAP that is required for granule formation(*19*), *in vitro* production of PHB granules using PHA synthase-fusion proteins provides a straight forward means of producing functionalized PHA granules(*52*). These modified PHB granules have shown promise in protein purification systems, immunedetection, and drug delivery(*15*). Table 1.1 summarizes the various approaches to PHB granule functionalization and their respective applications and a review of these functionalization approaches follows:

Medium	Granule formation	Functionalization strategy	Application
in vivo	Self-assembly	Phasin fusion	Protein purification(*36, 37*) FACS (*38*) ELISA(*38*) Fluorescence microscopy(*38*)
		PHA synthase fusion	Fundamental research(*39*) Biocatalyst*(*40, 41*) IgG purification from Serum(*42*) Antigen purification*(*43*) ELISA(*38, 41*) DNA purification(*41*) FACS(*38, 41, 44*) Contrast agent*(*45*) Fluorescence microscopy(*38*)
in vitro		PHA synthase fusion	Drug delivery*(*52*)
	Synthetic	PHA synthase fusion	Drug delivery*(*53*)
		Phasin fusion	Protein purification(*46*) Fertilizer*(*47*)
		PHA depolymerase fusions	Immunoassay(*48*) Drug delivery*(*49*) Protein microarrays*(*49*) Protein purification*(*49*)
		Polymer modification	Gene therapy(*50, 51*)

Table 1.1: PHB granule functionalization strategies and their applications

The recent recognition of PHB granules as nanoparticles that can be functionalized to suit various applications has resulted in studies for the development of diagnostics and therapeutics that employ PHB granules. Table 1.1 summarizes the various PHB modification strategies that have been employed to date and their respective applications. The listed applications have been demonstrated in the respective cited references with the exception of those marked with an asterisk (*) for which the applications have been proposed.

1.3.1. In vivo self-assembly and functionalization via GAP-fusion constructs

1.3.1.1.Phasin fusions

Phasins are amphiphilic GAPs that serve to stabilize PHB granules and prevent their coalescence as well as the nonspecific binding to their milieu(*54*). The hydrophobic region of phasins associates with the outer surface of a PHB granule and can thus be exploited for the coating of granules. Banki, et al. produced *in vivo* self-assembled derivitized PHB granules by introducing two plasmids into *Escherichia coli*; one expressing three enzymes necessary for transforming metabolic acetyl-CoA to PHB: α-ketothiolase (encoded by the *phaA* gene), a stereo-specific reductase (*phaB*), and PHA synthase (*phaC*), and another plasmid expressing a target protein fused to phasin (*phaP*) through a self-cleaving intein(*36*). In this manner, target protein-coated PHB granules were produced *in vivo*. The authors used this system to purify the target protein by lysing the expressing cell then separating and cleaning the derivitized PHB granules before cleaving the intein and releasing the target protein. Barnard, et al. developed a similar protein purification system in *Ralstonia eutropha*, a natural PHB producer, thus omitting the need for introducing exogenous PHB production genes into the host(*37*).

1.3.1.2.PHA synthase fusions

Fusions to PHA synthase have also been utilized for the production of modified PHB granules in vivo. Peters, et al. used *in vivo* PHB granule formation from PHA synthase-GFP (*39*) and PHA synthase-β-galactosidase(*40*) fusions, thereby producing fluorescent and enzyme-coated PHB granules. Similarly, Brockelbank, et al. fused the immunoglobulin G (IgG) binding ZZ domain of protein A from *S. aureus*(*42*), Grage, et al. fused an anti-β-galactosidase single-chain variable fragment antibody(*43*), and Peters, et al. fused mature full length, core and monomeric

streptavidin to the PHA synthase(*41*), each imparting analyte affinity to PHA granules. Bäckström, et al. developed multifunctional PHB granules through PHA fusions to the eukaryotic mouse myelin oligodendrocyte glycoprotein (MOG) and interleukin-2(*44*). In a similar manner, multifunctional PHB granules were obtained by Jahns, et al. in which an IgG binding ZZ domain of protein A in addition to two genetically engineered proteins designed to bind gold and silica(*45*) were fused to PHA synthase. In addition, multifunctional PHB granules used in FACS, ELISA, and fluorescent microscopy were produced by Atwood et al. where double-fusion constructs were prepared with GFP and murine myelin oligodendrocyte glycoprotein fused to the N- and C-terminus of both PHA synthase and phasin(*38*).

1.3.2. In vitro self-assembly and functionalization via GAP-fusion constructs

1.3.2.1.PHA synthase fusions

In addition to *in vivo* approaches, self-assembled modified PHB granules have also been produced via *in vitro* polymerization although only one example of this approach has been previously published. Kim, et al. used purified PHA synthase fused to RGD peptides and produced RGD-coated granules via *in vitro* polymerization from the fusion constructs(*52*). These granules were fluorescently labeled by loading the granule with the hydrophobic dye Nile red and were shown to specifically bind to breast cancer cells that constitutively express $\alpha_v\beta_3$ integrins thus showing promise as drug delivery vehicles.

1.3.3. In vitro derivatization of PHB via GAP-fusion constructs

1.3.3.1.PHA-synthase fusions

PHA synthase fusions have also been employed in in vitro derivatization of synthetically produced PHB particles. Lee, et al. developed an approach where the coupling between the hydrophobic surface of PHB nanoparticles and PHB chains

grown from PHA synthase fused with the tumor-specific ligand RGD4C allowed for functionalizing PHB nanoparticles(*53*). PHB nanoparticles loaded with Nile red were prepared through a solvent evaporation method and were then functionalized by the addition of RGD4C-PHA synthase fusions and 3HB-CoA which decorated the PHB nanoparticles with the fusions due to hydrophobic interactions between the particles and nascent PHB chains attached to the PHA synthase. The group demonstrated the specific affinity of the functionalized PHB nanoparticles to MDA-MB 231 breast cancer cells and proposed that this approach could be expanded as a drug-delivery method targeting specific cells.

1.3.3.2.Phasin fusions

Phasin-fusions have also been employed in the in vitro derivatization of PHB. Wang, et al. produced PHB granules *in vitro* from chemically extracted bulk PHA and mixed these with crude cell lysate containing phasin-tagged proteins produced in *Escherichia coli*(*46*). The system was then used to purify the tagged proteins from crude lysates by pelleting and washing the PHB granules via centrifugation. In contrast to the in vivo approach discussed in section 1.3.1.1, by separately producing PHB granules and the GAP-tagged protein fusions, the system could allow for the incorporation of a broader range of target proteins that may require eukaryotic expression systems. Moldes, et al. took a similar approach in attaching phasin-fusions to already synthesized PHB granules, though in this case granules were extracted from *P. putida* and used directly as-synthesized by the organism(*47*).

1.3.3.3.PHA depolymerase fusions

Lee, et al. tagged green and red fluorescent proteins as well as severe acute respiratory syndrome coronavirus (SARS-CoV) envelope protein with the substrate binding domain of PHA depolymerase from *A. faecalis* and decorated synthetic PHB

beads produced from extracted PHB bulk material(*48*). Similarly, Ihssen, et al. fused proteins to inactive extracellular PHA depolymerase from *P. fluorescens* and decorated synthetically produced granules of Poly[(3-hydroxyoctanoate)-co-(3-hydroxyhexanoate)] derived from *P. putida*(*49*).

1.3.4. In vitro chemical modification of PHA

An alternative approach towards developing functional PHA granules is to modify the polymer backbone to include specific functional groups. Sparks, et al. reported the synthetic production of the first cationic PHA, poly(β-hydroxyoctanoate)-co-(β-hydroxy-11-(bis(2-hydroxyethyl)-amino)-10-hydroxyundecanoate) (PHON)(*50*) by chemically modifying poly(β-hydroxyoctanoate)-co-(β-hydroxyundecenoate) extracted from *P. putida GPo1*. More recently the authors reported the use of this polymer as a plasmid DNA delivery system(*51*).

1.4. PHB particle-based drug delivery

PHB associates with other macromolecules via hydrogen bonding to the polymer chain(*55*). Cations can also coordinate with the carbonyl groups on the structure(*55*). In addition, the spacing of electron-donating groups along the polymer chain allows for multiple bonding interactions which permits the binding of proteins and the formation of complexes with salts(*27*).

Several studies have explored the potential of using PHB particles as drug release formulations(*56, 57*). Table 1.2 outlines the use of PHB as a microencapsulation agent where anticancer drugs (CCNU, lastet, and 2',3'-diacyl-5-fluoro-2'-deoxyuridine)(*58-60*), the contraceptive progesterone(*61*), the antimicrobials sulfamethizole(*62*) and netilmicin(*27, 63*), and the dyes dichlorofluoroscein(*64*) and Nile red(*52*) have been encapsulated.

The majority of microencapsulation approaches have employed solvent evaporation processes though encapsulation has also been demonstrated using *in vitro* PHB polymerization(*27, 52, 63*). Nobes, et al. encapsulated the antibiotic netilmicin by dissolving netilmicin in phosphate buffer, adding 3HB-CoA, and PHA synthase(*27, 63*). The maximum encapsulation efficiency was found to be approximately 4.5%, comparing favorably with the encapsulation efficiency of anionic and cationic liposomes(*65*).

The rate of release from encapsulating PHB microspheres has also been studied and varies widely depending on the encapsulated material. When comparing the rate of release with that of poly(lactic acid), one of the most widely used biodegradable polymers, some materials exhibit a much higher rate of release for PHB(*58*) while others materials exhibit a very slow rate of release(*59*).

Substance type	Substance	Encapsulation process	Size (µm)	Release	Ref
Anticancer drug	1 -(2 chloroethyl)-3-cyclohexylnitrosourea	Solvent evaporation	1-5	90% in 10 h	(*58*)
	Alcarubicin	Solvent evaporation	158-214	10% in 120 h	(*59*)
	Lastet	Solvent evaporation	15-25	Variable	(*66*)
	2',3'-Diacyl-5-fluoro-2'-deoxyuridine	Solvent evaporation	101-326	Variable	(*60*)
	Retinoic acid	Solvent dialysis	50 nm	nd	(*57*)
Contraceptive	Progesterone	Solvent evaporation	nd	Variable	(*61*)
Vaccine	Staphylococcal enterotoxin B	Solvent evaporation	1-10	Variable	(*67*)
Dye	Dichlorofluorescein	Solvent evaporation	nd	94% in 3 h	(*68*)
	Nile red	*In vitro* polymerization	70-600 nm	nd	(*52*)
		Solvent evaporation	~200 nm	nd	(*53*)
Antimicrobial	Netilmicin	*In vitro* polymerization	nd	nd	(*27, 63*)
	Sulfamethizole	Solvent evaporation	53-2000	50% in 12 h	(*62*)

Table 1.2: Microencapsulated substances in polyhydroxyalkanoates

Various substances have been microencapsulated in polyhydroxyalkanoates particles as potential drug release formulations. The majority of microencapsulation approaches have employed solvent evaporation processes though encapsulation has also been demonstrated using in vitro PHB polymerization. The rate of release from encapsulating PHB microspheres has also been studied and varies widely depending on the encapsulated material. Table 1.2 has been adapted from Nobes, et al.(27).

1.5. Overview of dissertation

PHB granules are emerging as a promising nanomaterial for a variety of biomedical applications. These granules benefit from a biocompatible and biodegradable core that may be loaded with molecules that impart imaging and therapeutic capabilities and the granule surface may be modified for a wide range of functionalities.

This dissertation describes the development, characterization, and potential applications of nanoparticle-coated PHB granules. Chapter 2 describes the development of gold (AuNP) and superparamagnetic iron oxide nanoparticle (SPION)-PHA synthase conjugates that produce nanoparticle-coated PHB granules upon the addition of 3HB-CoA. The properties and potential applications of the resulting nanoparticle-coated PHB granules are discussed in Chapters 3 and 4 and the dissertation concludes with general conclusions and future directions discussed in Chapter 5.

In the past, a wide range of biomolecules have been immobilized on the surface of PHB granules that have allowed for using functionalized granules in applications ranging from protein purification(*42, 105*) to cancer cell targeting(*44, 52*). Of the PHB granule functionalization strategies employed to date, only one approach has allowed for coating PHB granules with inorganic materials(*45*) requiring the subsequent decoration of *in vivo*-produced and extracted granules and resulting in sparsely coated nanoparticle-PHB granule hybrid materials that were not further characterized. In contrast to *in vivo* granule formation, our *in vitro* approach allows for the direct assembly of nanoparticle-coated PHB granules in a single-step process allowing for straightforward means of controlling PHB granule size and resulting in densely nanoparticle-coated PHB granules. These improved nanoparticle-PHB

granule hybrid materials exhibit unique properties to those of PHB and the nanoparticles alone as a result of the arrangement of the nanoparticles on the PHB granule surface.

The studies in this dissertation describe a novel means of producing nanoparticle-coated PHB granules that expands the capabilities of functionalized PHB granules through harnessing versatile properties of inorganic nanoparticles. The SPION-coated PHB granules that are potential MRI contrast agents with enhanced imaging capabilities afforded by PHB mediated aggregation of SPION that resulted in SPION-coated PHB while AuNP-coated PHB granules are potential theranostic agents that have enhanced imaging capabilities and are also capable of heating upon near-infrared (NIR) laser irradiation. In general, both of these materials may be suitable as multifunctional theranostic agents with imaging (MRI, fluorescence/SERS, enhanced fluorescence) and therapeutic (drug delivery/photothermal heating) capabilities.

Chapter 2 – Nanoparticle-PHA synthase conjugates

2.1. Abstract

Polyhydroxyalkanoate (PHA) synthase was conjugated to gold nanoparticles (AuNP) and superparamagnetic iron oxide nanoparticles (SPION) resulting in PHA synthase-nanoparticle conjugates with a hydrodynamic diameter of ~45 nm as determined via dynamic light scattering. Upon the addition of 3-hydroxybutyrate-CoA (3HB-CoA), these nanoparticle-PHA synthase conjugates produced poly(3-hydroxybutyrate) (PHB) and then coalesce to form nano- to micron-sized nanoparticle-coated PHB granules. The granule formation mechanism is thought to occur in a manner analogous to native *in vitro* PHB granule formation in which PHA synthase remains on the granule surface. The nanoparticle-PHA synthase conjugates described in this work offer a novel means of producing nanoparticle-coated PHB granules that may exhibit useful physical properties derived from their nanoparticle-coating.

2.2. Introduction

Previous work in the Batt laboratory has employed PHA synthase through enzymatic surface initiated polymerization (ESIP) for applications in bottom-up nano/microfabrication on a variety of micropatterned surfaces as well as on microbeads(*8, 69-73*). In this prior work, the introduction of a histidine tag to PHA synthase also allowed for the site-specific and reversible functionalization of the enzyme onto surfaces via their modification with nickel nitrilotriacetate (Ni-NTA). Kim, et al. constructed PHB-coated agarose microbeads from Ni-NTA derivitized agarose beads resulting in uniformly coated structures(*70, 71*). Additionally, PHB could be released from the bead surface by the addition of imidazole, which out-

competes the imidazole side chains of histidine bound to Ni-NTA thus releasing the His-tagged PHA synthase along with the PHB polymer chain.

In this current study, we thought to expand our repertoire of ESIP-derived structures by functionalizing nanoparticles with PHA synthase, providing a novel platform – nanoparticles – from which to polymerize PHB. Based on the natural PHB granule structure (Figure 1.2), those produced from nanoparticle-PHA synthase conjugates were expected to result in nanoparticle-coated granules that would lead to the possibility of exploiting effects caused by the nanoparticle aggregation on the granule surface. Gold and superparamagnetic iron oxide nanoparticles (AuNP and SPION, respectively) were first conjugated to PHA synthase and PHB polymerization was then initiated from these conjugates resulting in nanoparticle-coated PHB granules.

AuNP and SPION were chosen based on their respective properties that make these materials candidates for a wide range of advanced diagnostic and therapeutic applications. These properties are summarized below:

2.2.1. SPION: MRI contrast enhancement

Local variations in the magnetic properties within a medium give rise to MRI contrast gradients arising from variations in the transverse relaxation times (T2) of nearby protons. Tissue susceptibility gradients may exist when either endogenous or exogenous paramagnetic materials accumulate locally within tissues. Endogenously occurring paramagnetic substances include deoxyhemoglobin, methemoglobin, hemosiderin, melanin, and ferritin(*74*). Exogenous materials such as superparamagnetic iron oxide-based contrast agents consist of suspended colloids of iron oxide nanoparticles that shorten the T2 relaxation times of absorbing protons in tissues thereby enhancing the MR contrast of these tissues(*75*). A single SPIO particle consists of large amounts of iron and results in several orders of magnitude higher

relaxivities than the more common gadolinium-based contrast agents. SPIO nanoparticles are among the few FDA approved nanomaterials and several SPION, typically 50 nm in diameter, are currently in clinical use as MRI contrast agents(*76*).

2.2.2. AuNP: optical and photothermal properties

2.2.2.1.Raman spectroscopy

Raman spectroscopy is a branch of vibrational spectroscopy in which the transitions between molecular vibrational states are studied using the scattered radiation produced when a molecule absorbs a photon of light(*77*). A valuable extension of Raman spectroscopy is derived from a substantial Raman signal enhancement factor (on the order of 10^6) that can be achieved when molecules are physisorbed or chemisorbed to metallic nanostructures(*78*). The enhancement is primarily derived from an increase in the electric field around the molecule due to surface plasmon resonances (SPR) generated by the excitation of conduction electrons on the surface of nanoparticles(*79, 80*). Gold and silver are typical metals for SERS experiments because their SPR frequencies fall within wavelengths of visible and NIR light(*81*).

2.2.2.2.*Enhanced fluorescence*

In contrast to SERS phenomena, when a fluorophore is localized to metal particles or surfaces at less than ~5 nm, its emission is quenched by energy transfer to the metal(*82*). However, at further distances (between 5 and 70 nm), increases in fluorescence by factors of up to 1000 can be observed(*82-85*). Two phenomena can contribute to this fluorescent enhancement including surface enhanced fluorescence (SEF) in which the metal particles concentrate the local excitation intensity and metal enhanced fluorescence (MEF) in which the electric field felt by a fluorophore is affected by interaction of the fluorophore oscillating dipole with the metal surface(*85-*

88). In the latter case, there is an increase in the radiative rate of the fluorophore that results in an increased intensity and, since the fluorophore will spend less time in the excited state for each excitation, the extent of photobleaching of the fluorophore also decreases.

2.2.2.3.*Photothermal heating*

AuNPs usually exhibit a significant absorption peak from 500 to 550 nm, due to their surface plasmon that arises from the oscillation of the valence electrons in resonance with incident photons(*81*). The resonating surface plasmon decays by radiating its energy resulting in light scattering or conversion of absorbed light to heat(*89*). This later nonradiative component of the extinction is efficiently converted via electron-electron and electron-phonon relaxations to heat on the order of picoseconds(*90-93*) allowing for localized heating of the medium immediately surrounding the nanoparticle(*94*). As a result, AuNPs can convert absorbed light to heat at efficiencies that are far greater than that of conventional dyes(*95*). A particular advantage of using gold nanoparticles in photothermal applications is the possibility of using an NIR illumination source that exploits the 'water window' in the wavelength regions between 600-1100 nm. At these wavelengths there is a lack of efficient endogenous absorbers in cells and tissues allowing for high light penetration depth and decreased laser damage to non-target tissue(*96, 97*).

2.3. Experimental

2.3.1. Expression and purification of PHA synthase

His_{10}-tagged *PHA synthase* of *Ralstonia eutropha* H16 (DSM428) (His_{10}-tagged $PhaC_{Re}$) was expressed from a recombinant *Escherichia coli* strain developed using the BL21 (DE3) pLysS (Novagen)/pET-CO1 expression system (EMD

Chemicals Inc./Merck KGaA, Darmstadt, Germany) as described elsewhere(*69*). Overnight cultures from frozen recombinant *Escherichia coli* stocks were first grown at 37°C on solid LB media containing 100 µg/mL of ampicillin. Overnight liquid cultures were then grown from single colonies taken the overnight cultures and used to inoculate 5 mL of LB and 100 µg/mL of ampicillin incubated shaking at 250 RPM and at 37°C. This 5 mL pre inoculum was then used to inoculate 500 mL of LB containing 100 µg/mL of ampicillin. The 500 mL cultures were grown in a shaking incubator at 37°C and 250 RMP to an OD_{600nm} of 0.4-0.6 (1-3 hrs) and then induced to express PHA synthase with the addition of 200 µM isopropyl β-D-1-thiogalactopyranoside (IPTG). After culturing the cells for an additional 5 hrs in a shaking incubator at 30°C and 250 RMP, the cells were pelleted by centrifugation (4,000 x g, 10 min, 4°C), the supernatant was discarded and the cell pellet was resuspended in lysis buffer (50 mM Na-phosphate buffer, pH 7, 10 mM imidazole). Following resuspension, the cells were homogenized (Emulsiflex-C3, Avestin, Ottawa, Canada) with the addition of DNAse (TURBO, DNAse, Applied Biosystems, Carlsbad, CA), centrifuged (13,000 x g, 30 min, 4°C), and the cell lysate supernatant was collected and filtered using a 0.22 µm vacuum filter. The filtrate was then combined with Ni(II)-charged immobilized metal ion chromatography (IMAC) resin (Chelating Sepharose Fast Flow, GE Healthcare, Uppsala, Sweden) at a volume to volume ratio of 1:4 (resin:lysate), and allowed to mix for 15 min at room temperature with gentle rocking. The lysate-resin mix was then placed in a glass gravity-flow column and the flow-though was eluted and collected. The resin was washed with 2-column volume of lysis buffer and 4 column volumes of wash buffer (50 mM Na-phosphate buffer, pH 7, 20 mM imidazole). One column volume of elution buffer (50 mM Na-phosphate buffer, pH 7, 300 mM imidazole) was then added to the washed resin and allowed to mix in the column for 15 min at room temperature. The flow-though was then eluted and another

column volume of elution buffer was added to the column and immediately allowed to flow though. Next, an additional column volume of elution buffer was added to the column flowed through the column with the addition of pressure using a 20 cc syringe. All washes and elutions were collected for analysis via SDS-PAGE and Western blot.

The total amount of purified protein was determined via the Bradford assay following the manufacturer's protocol (Bio-Rad Protein Assay, Bio-Rad Laboratories, Hercules, CA). The purity of PHA synthase was analyzed by SDS-PAGE and elution fractions at greater than 50% purity were concentrated to 1 mg/mL by centrifugation using 30 kDa-cutoff spin filter units (Amicon Ultra-15 Centrifugal Filter Unit with Ultracel-30 membrane, Millipore, Billerica, MA). The concentrated purified PHA synthase was then buffer exchanged from elution buffer into 50 mM Na phosphate buffer, pH 7 via size exclusion chromatography (SEC).

Size exclusion chromatography was performed using a C 16/70 column packed with Superdex 200 resin connected to an AKTÄ Explorer fast protein liquid chromatography system (GE Healthcare, Uppsala, Sweden). The column was calibrated using Aqueous SEC 1 protein molecular weight standards following the manufacturer's protocol (Phenomenex, Torrance, California). The mobile phase was 50 mM Na phosphate buffer, pH 7, the flow rate was 1 mL/min, and sample injections were 500 µL.

2.3.2. Synthesis of 3HB-CoA

3HB-CoA was synthesized from the reaction of *β*-butyrolactone with free coenzyme A (CoA) following the method of Simon, et al.(*98*). Twenty five mg (32.6 µmoles) of coenzyme A lithium salt (Sigma Aldrich, St. Louis, MO) was dissolved in 1.25 mL of a 0.2 M $KHCO_3$ solution within a glass container including a magnetic stir bar. The container was placed in an ice bath and 28 mg (326 µmoles) of *β*-butyrolactone (molar ratio of CoA to lactone 1:10) was dripped into the container

while stirring. Following Song, et al.(*99*), the reaction was allowed to continue for 120 min then excess lactone was removed by three extractions with ether. The solution was then lyophilized and stored at -20°C.

Ellman's reagent, 5,5'-dithiobis(2-nitrobenoic acid) (DNTB) (Thermo Fisher Scientific, Rockford, IL), was used for determining the concentration of free CoA in the final reaction solution to determine the yield of the reaction (see *In vitro* Polymerization of 3HB-CoA).

2.3.3. Nanoparticle synthesis

2.3.3.1.SPION

Particles were synthesized following Sun, et al. Briefly, Fe_3O_4 nanoparticles were made mixing $Fe(acac)_3$ (2 mmol) in phenyl ether (20 mL), 1,2-hexadecanediol (10 mmol), oleic acid (6 mmol), and oleylamine (6 mmol) under nitrogen then heating to 260^{o}C and refluxed for 30 minutes(*76*). After cooling to room temperature, black colored magnetite crystals were isolated by adding an excess amount of ethanol followed by centrifugation. The ethanol was then discarded and the precipitant dried at room temperature. The dried SPIO particles were then resuspended in chloroform at a concentration of 50 mg/mL and stored at -20 °C.

2.3.3.2.AuNP

Particles were synthesized following Presa, et al. Briefly, Au nanoparticles were made mixing gold acetate $Au(ac)_3$ (0.27 mmol), 1,2- hexadecanediol (1.9 mmol), and phenyl ether (30 mL) in a three neck flask then heating to 80°C under N_2 before adding oleic acid (1 mmol) and oleylamine (1 mmol) then refluxing at 260°C for 30 min(*100*). After cooling to room temperature, purple colored gold crystals were isolated by adding an excess amount of ethanol followed by centrifugation. The ethanol was then discarded and the precipitant dried at room temperature. The dried

Au particles were then resuspended in chloroform at a concentration of 50 mg/mL and stored at -20°C.

2.3.4. Nanoparticle functionalization

The nanoparticle functionalization is depicted in Figure 2.1. Oleic acid/oleylamine-coated nanoparticles were made water soluble following Dubertret, et al.(*101*). Briefly, 17 mg of nanoparticle-oleic acid/oleylamine in chloroform was mixed with 5.5 μmoles of 1,2-Distearoyl-sn-Glycero-3-Phosphoethanolamine-N-[Carboxy(Polyethylene Glycol)2000] (PL-PEG-COOH) (Avanti Polar Lipids, Alabaster, AL) in chloroform. PL-PEG-COOH consists of phospholipids attached to 45-unit polyethylene glycol (PEG) with a carboxylic acid at its terminus that can be used for further chemical modification. The mixture was sonicated in a bath sonicator (Branson Sonifier 250, Branson Ultrasonics, Danbury, CT) (200 watts, 30 min) and was then placed in a fume hood until the chloroform was completely evaporated. Next, 1 mL of reagent grade water (Nerl Diagnostics, East Providence, RI) was added and the mixture was again sonicated for 30 min and the resulting suspension was ultracentrifuged at 500,000 x g for two hrs to remove empty phospholipid micelles. The supernatant was then discarded and the pellet was reconstituted in 1 mL of reagent grade water then passed through a 0.1 μm filter to remove aggregates and the suspension was then stored at 4°C.

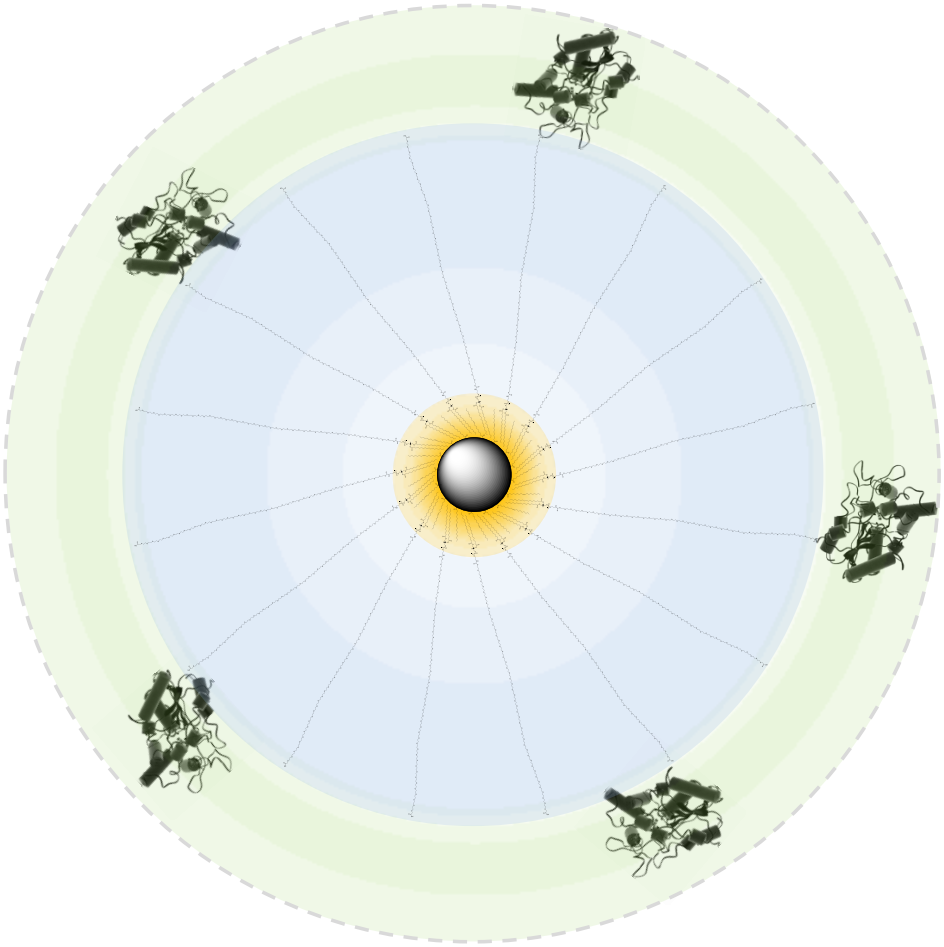

Figure 2.1: Nanoparticle functionalization

The figure depicts the composition and structure of nanoparticle-PHA synthase conjugates employed in this study. Oleic acid/oleylamine-coated nanoparticles (orange shaded area) were made water soluble through coating the particles with carboxy-terminated PEGylated phospholipids (blue area). The carboxyl groups on the surface of these now water soluble particles were then converted to primary amine-reactive NHS-esters which were subsequently reacted with PHA synthase forming a covalent bond between the PEG on the particle and primary amines of PHA synthase (green area). The dimensions of these structures are outlined in Figure 2.8.

Next, the carboxyl groups of the nanoparticle-PL-PEG-COOH were converted to primary amine-reactive NHS-esters using 1-ethyl-3-[3-dimethylaminopropyl] carbodiimide hydrochloride (EDC) and NHydroxysulfosuccinimide (sulfo-NHS) (Thermo Fisher Scientific, Rockford, IL). Briefly, an aliquot containing of nanoparticle-PL-PEG-COOH was added to 0.1 M (2-(N-morpholino)ethanesulfonic acid) (MES) and 9% NaCl at pH 4.7. EDC and sulfo-NHS were then added to this mixture at 4 mM and 10 mM, respectively at a final volume of 0.5 mL and the mixture was allowed to react for 30 min at room temperature. Excess EDC and sulfo-NHS was then removed separated from nanoparticle-PL-PEG-NHS-ester via size exclusion with 50 mM Na-phosphate buffer at pH 7 as the mobile phase and the purified particles were concentrated to 0.5 mL using a 30 kDa spin column. Immediately after purification, the nanoparticle-PL-PEG-NHS-ester suspension was mixed with PHA synthase in 50 mM Na-phosphate buffer at pH 7 at a 1:1 nanoparticle:PHA synthase mass to mass ratio. This mixture was allowed to react for two hours at room temperature then excess unconjugated protein was separated from nanoparticle-PL-PEG-PHA synthase conjugates via SEC with 50 mM Na-phosphate buffer at pH 7 as the mobile phase. Finally, the purified conjugates were again concentrated to 0.5 mL using a 30 kDa spin column.

2.3.5. Particle size analysis

The sizes of the nanoparticle cores were determined by transmission electron microscopy (TEM) and dynamic light scattering (DLS). Transmission electron microscopy was conducted using a Philips EM-201 (Royal Philips Electronics, Amsterdam, Netherlands) operating at 80 keV. Samples were prepared for imaging by dipping 200 mesh copper formvar coated grids stabilized with evaporated carbon (Electron Microscopy Sciences, Hatfield, PA) in 5 uL drops of sample for 30 min followed by washing the grid by dipping it in reagent-grade water then drying the grid

by wicking away excess liquid. Dynamic light scattering measurements were performed on a Zetasizer Nano ZS system (Malvern Instruments, Worcestershire, United Kingdom). Samples were passed through a 0.22 μm filter prior to placement in 1 mL polypropylene cuvettes for measurement. Measurement results of the most abundant species in the sample were summarized by the number statistics analysis performed by the Zetasizer software.

TEM image analysis was performed using Image J (National Institutes of Health, Bethesda, Maryland). Because the TEM samples are unstained, only the electron-dense AuNP and SPION cores can be readily observed in the TEM image. Particles were analyzed using Image J's particle analysis feature in which a threshold was first set that resolved the nanoparticles then the diameters of nanoparticles were determined for particles selected by the software. The particle selection criteria screened for particles with a circularity of 0.9, defined as the following: circularity = $4\pi(\text{area}/\text{perimeter}^2)$, where a circularity value of 1.0 indicates a perfect circle and values approaching zero indicate an increasingly elongated polygon. This value of circularity was chosen to avoid counting closely spaced particles as a single large particle and furthermore, the results of the analysis were verified visually to ensure only individual particles were included in the measurement.

The resulting size distribution data of 100 particles was summarized as a histogram with the bin size chosen using a histogram bin size optimization tool developed by Shimazaki (2010)(*102*). The histogram data for each measurement was then plotted using OriginPro 7.5 (OriginLab Corporation, Northampton, MA) and fit using OriginPro's non-linear curve fitting feature employing the software's peak function algorithms. Fits for which the resulting coefficient of determination was closest to a value of 1 were chosen used to determine the median nanoparticle size.

The diameter of nanoparticles coated with oleic acid/oleylamine, PL-PEG-COOH, and PL-PEG-PHA synthase were all measured via DLS using the appropriate buffer (chloroform or 50 mM sodium phosphate buffer, pH 7). The DSL instrument provided a histogram of the diameters of the most abundant species in the sample with the bin size automatically chosen by the instruments algorithm. The resulting histogram data for each measurement was then plotted using OriginPro 7.5 and fit using OriginPro's non-linear curve fitting feature employing the software's peak function algorithms. Fits for which the resulting coefficient of determination was closest to a value of 1 were chosen used to determine the median nanoparticle size.

2.3.6. *In vitro polymerization of 3HB-CoA*

In vitro polymerization of PHB from nanoparticle-PL-PEG-PHA synthase conjugates was carried out by mixing samples of nanoparticle-PL-PEG-PHA synthase suspended in 50 mM Na-phosphate buffer, pH 7 with 3HB-CoA dissolved in reagent-grade water to a final 3HB-CoA concentration of 2.5 mM. The mixtures were allowed to react for two hours at room temperature. For samples prepared for fluorescent microscopy analysis of polymerization, Nile red dissolved in DMSO was also added along with 3HB-CoA to a final Nile red concentration of 50 μg/mL.

2.4. Results and discussion

2.4.1. Nanoparticle synthesis

The SPIO and gold nanoparticle synthesis produced oleic acid/oleylamine-coated particles with a median core diameter of 3.45 nm for SPION (Figure 2.2A) and 5.05 nm for AuNP (Figure 2.2B) as determined via TEM. The median diameter of the oleic acid/oleylamine-coated particles was measured to be 9.25 nm for SPION (Figure 2.3A) and 9.50 nm for AuNP (Figure 2.3B) as determined by DLS, a size increase that

is consistent taking into account a monolayer coating of oleic acid/oleylamine around the nanoparticles (1.8 nm) and the chloroform solvent layer (0.64 nm).

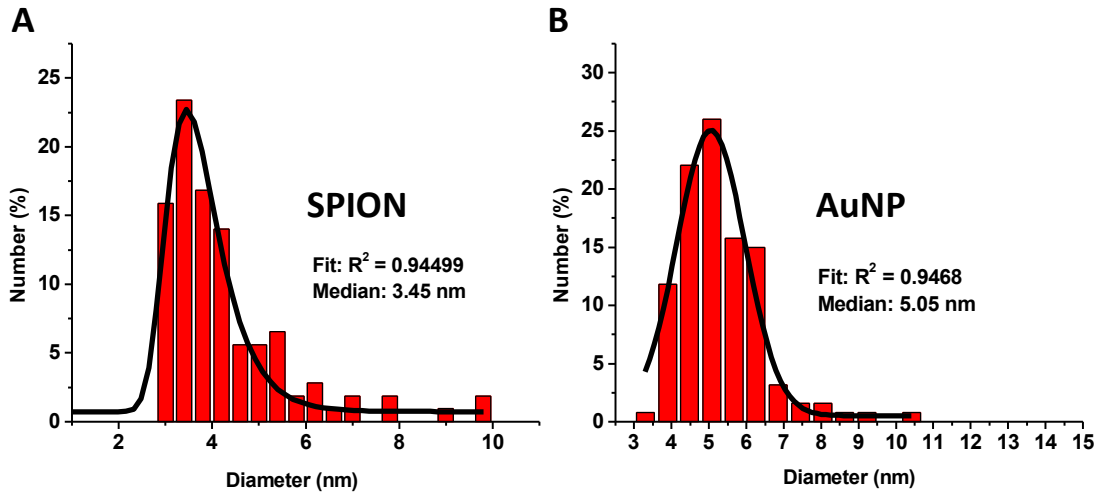

Figure 2.2: Nanoparticle core diameter

The diameters of 100 nanoparticle cores were determined via TEM image analysis using Image J's particle analysis algorithm. The resulting size distribution data is summarized as a histogram with the bin size chosen using a histogram bin size optimization tool(102). A peak function fit of the data for which the resulting coefficient of determination was closest to a value of 1 was used to determine a median particle size. Based on the curve fit, the median SPION core diameter (A) was determined to be 3.45 nm and the median AuNP core diameter (B) was determined to be 5.05 nm.

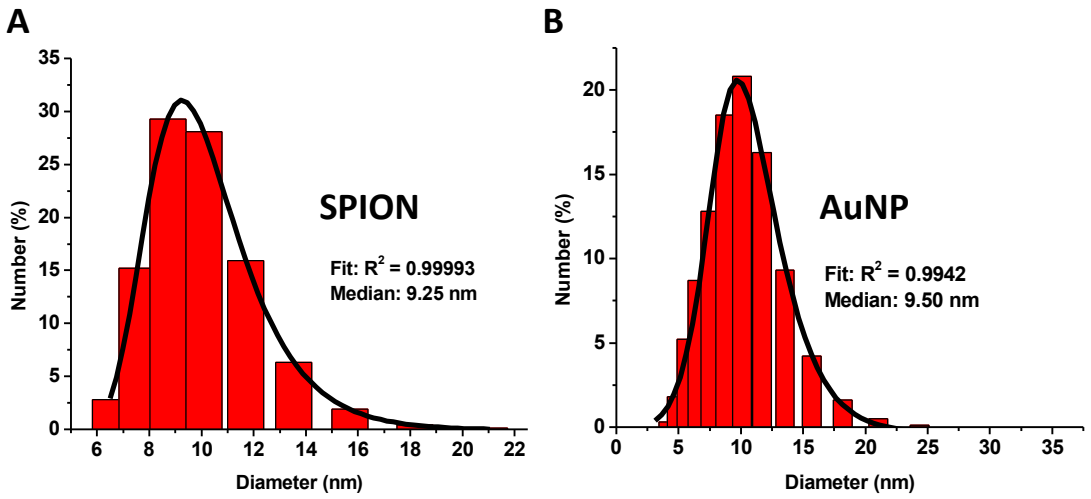

Figure 2.3: Nanoparticle-oleic acid/oleylamine diameter

The diameters of as-synthesized oleic acid/oleylamine-coated nanoparticles suspended in chloroform were measured via dynamic light scattering that provided a histogram of the diameters of the most abundant species in the sample with the bin size automatically chosen by the instruments algorithm. A peak function fit of the data for which the resulting coefficient of determination was closest to a value of 1 was used to determine a median particle size. Based on the curve fit, the median diameter of the oleic acid/oleylamine-coated SPION (A) was determined to be 9.25 nm and the median diameter of the oleic acid/oleylamine-coated AuNP (B) was determined to be 9.50 nm.

2.4.2. Nanoparticle-PL-PEG-COOH Functionalization

After encapsulation of the oleic acid/oleylamine nanoparticles with carboxy-terminated PEGylated phospholipids (PL-PEG-COOH) the median particle size now increased to 44.5 nm for SPION (Figure 2.4A) and 45.0 nm for AuNP (Figure 2.4B) as measured by DLS, a size increase that is consistent with the coating of fully extended PL-PEG-COOH (16.7 nm) and the water solvent layer (0.25 nm). See Figure 2.8 for a summary of the expected and measured size of the nanoparticles at each step in the functionalization process.

2.4.3. PHA synthase preparation

When the PHA synthase elution fraction from IMAC purification were processed via SEC, three peaks appearing at ~512 kDa, ~69 kDa, and ~6.5 kDa were observed in the chromatogram (Figure 2.5). SDS PAGE and Western blot analysis of fractions collected from each of these peaks revealed that both the ~512 kDa and ~69 kDa peaks contained PHA synthase. The ~69 kDa peak includes the His-tagged PHA synthase monomer (~67.5 kDa) while the ~512 kDa peak includes PHA synthase aggregates. PHA synthase is known to dimerize, however, these aggregates were would apparently comprised of 7-8 monomers based on molecular weight and are perhaps instead due to aggregates including endogenous PHB produced by the *Escherichia coli* host(*103*). This observation lead us to only collect the monomer peak for further processing while discarding the aggregate peak as the aggregate peak would otherwise co-elute with nanoparticle-PHA synthase conjugates during subsequent SEC steps and thus result in the possibility of not removing unconjugated PHA synthase (Figure 2.6). Separation of these aggregates ensures that no unconjugated PHA synthase is present in the sample since free PHA synthase can contribute to the formation of PHB granules devoid of nanoparticles. The collected

monomeric PHA synthase remained in its un-aggregated form for at least 24 hrs of storage in 50 mM Na phosphate buffer, pH 7 as confirmed by subsequent SEC. For two separate runs, the average amount of enzyme lost due to the discarding of aggregates during the purification process was 42% of the IMAC-purified material as determined by SDS-PAGE and densitometry.

2.4.4. Nanoparticle-PHA synthase conjugation

Functionalization of the PEG-COOH-coated nanoparticles with PHA synthase yielded particles with a median diameter of 45.2 nm for SPION (Figure 2.7A) and 46.8 nm for AuNP (Figure 2.7B) as determined via DLS. This size increase does not reflect an expected particle growth from the addition of PHA, where at 67.5 kDa and assuming a globular conformation, a PHA hydrodynamic diameter of 7.2 nm (estimate based on the Zetasizer software Protein Analysis Utility) would lead to a nanoparticle conjugates having a diameter of ~54-56 nm (Figure 2.8). A likely explanation for this discrepancy is that the number of PHA synthase per particle is not homogenous and the observed size distribution is comprised of a mixture of particles with and without conjugated PHA synthase. Similar to nanoparticle-PL-PEG-COOH, these DLS and TEM observations indicate that nanoparticle-PL-PEG-PHA synthase particles consist of individual and un-aggregated particles in solution which is an important characteristic since starting with un-aggregated nanoparticle-PHA synthase conjugates prior to polymerization allowed for studying aggregation-derived phenomena upon aggregation mediated by PHB polymerization from the conjugates as described in Chapters 3 and 4.

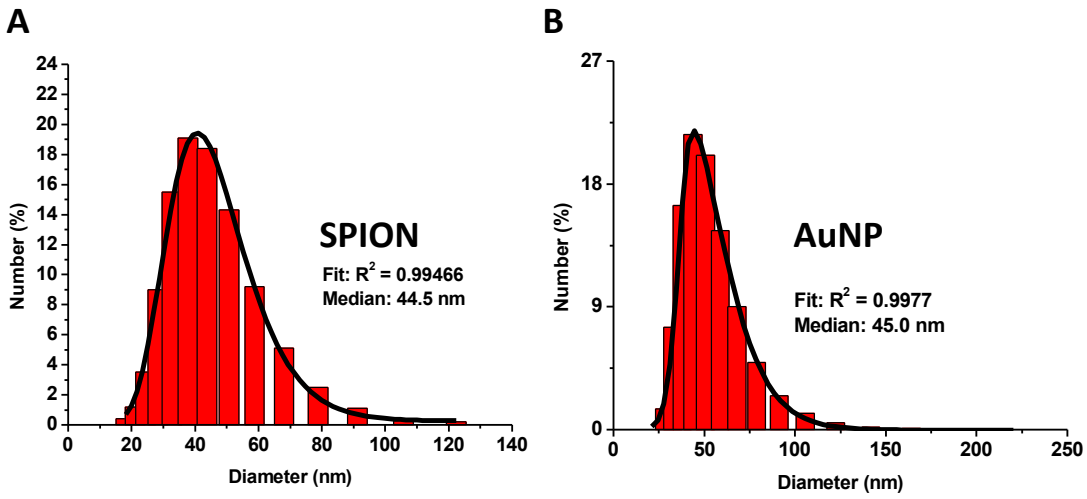

Figure 2.4: Nanoparticle-PL-PEG-COOH diameter

The diameters of carboxy-terminated PEGylated phospholipid-coated nanoparticles suspended in deionized water were measured via dynamic light scattering that provided a histogram of the diameters of the most abundant species in the sample with the bin size automatically chosen by the instruments algorithm. A peak function fit of the data for which the resulting coefficient of determination was closest to a value of 1 was used to determine a median particle size. A) The median diameter of carboxy-terminated PEGylated phospholipid-coated SPION was determined to be 44.5 nm. B) The median diameter of carboxy-terminated PEGylated phospholipid-coated AuNP was determined to be 45.0 nm.

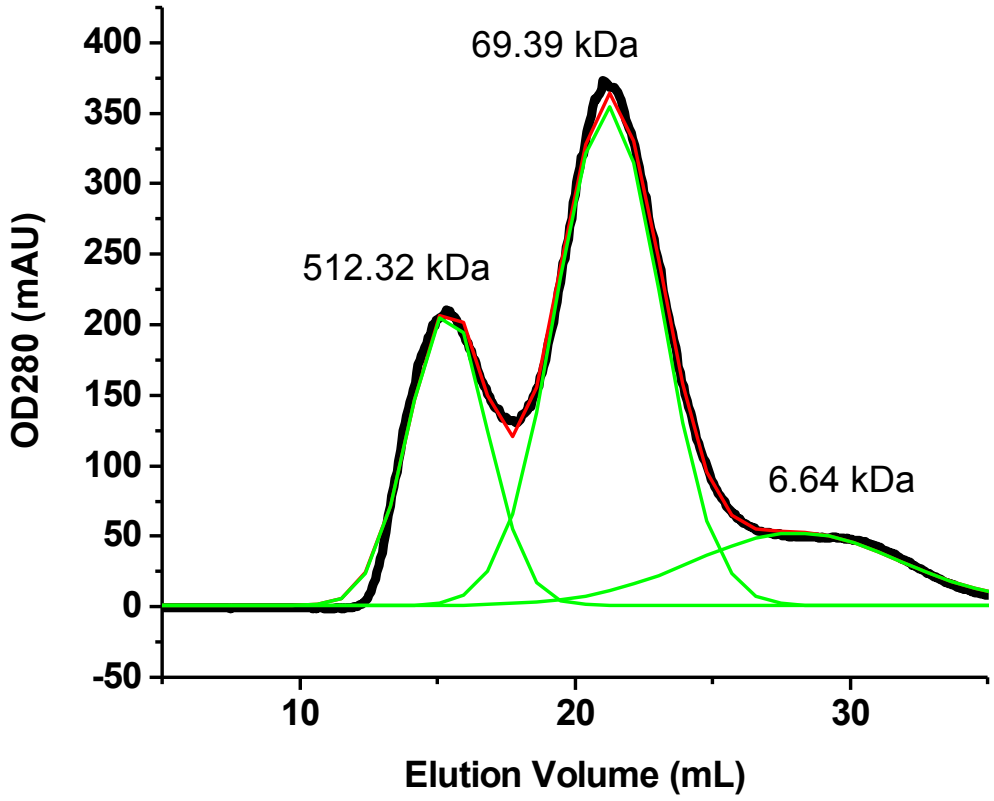

Figure 2.5: Size exclusion chromatography of IMAC-purified PHA synthase

IMAC-purified PHA synthase was processed via SEC, the chromatogram of which revealed three peaks appearing at ~512 kDa, ~69 kDa, and ~6.5 kDa based on a three-peak Gaussian fit of the chromatogram data (green and red traces, R^2 = 0.99775). Both the ~512 kDa and ~69 kDa peaks contained PHA synthase as determined by Western blot analysis of SDS PAGE processed IMAC-purified material, the smaller of which is derived from PHA synthase monomer.

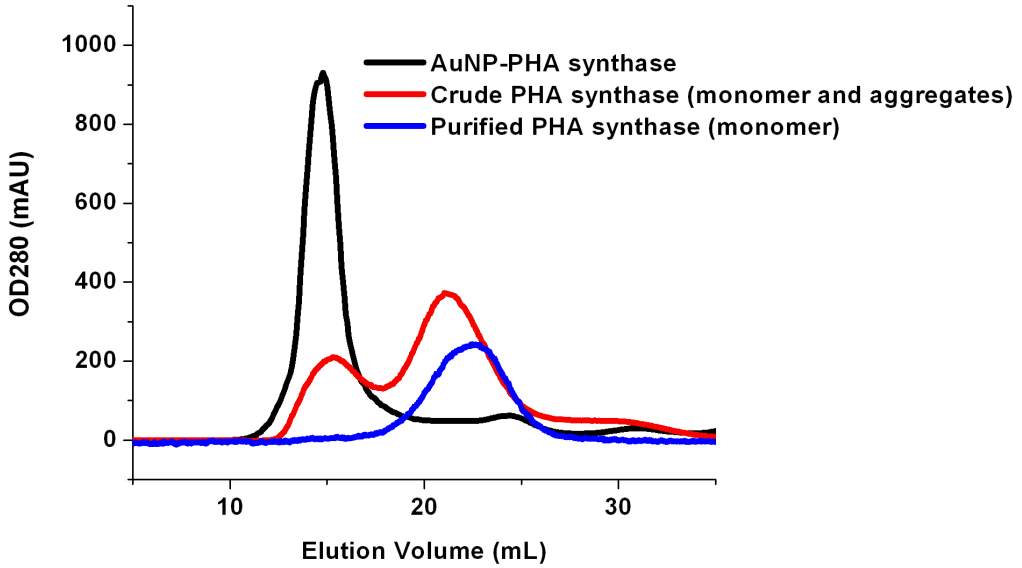

Figure 2.6: Size exclusion chromatography of PHA synthase and nanoparticles

IMAC-purified PHA synthase (red trace), PHA synthase monomer (blue trace), and nanoparticle-PHA synthase conjugates (black trace) were each processed by SEC. The figure shows each SEC chromatogram superimposed where it can be seen that PHA synthase aggregates (first peak in the red trace) co-elute with nanoparticles while PHA synthase monomer does not. In order to ensure that nanoparticle-PHA synthase conjugate material did contain un-conjugates PHA synthase, PHA synthase monomer was used in the conjugation reaction that was subsequently processed via SEC, discarding material that eluted after the nanoparticle peak.

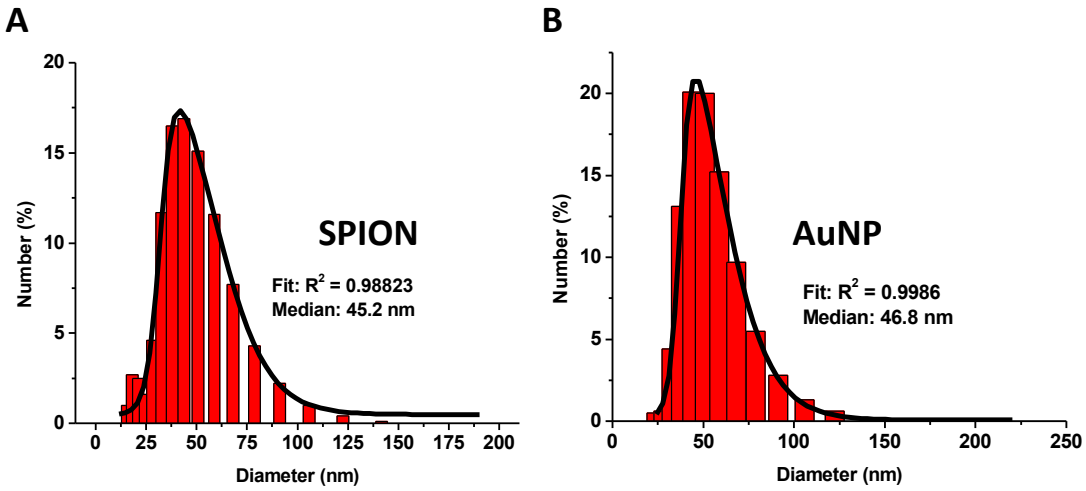

Figure 2.7: Nanoparticle-PHA synthase diameter

The diameters of PHA synthase-conjugated nanoparticles suspended in phosphate buffer were measured via dynamic light scattering that provided a histogram of the diameters of the most abundant species in the sample with the bin size automatically chosen by the instruments algorithm. A peak function fit of the data for which the resulting coefficient of determination was closest to a value of 1 was used to determine a median particle size. A) Functionalization of the PEG-COOH-coated SPION with PHA synthase yielded particles with a median diameter of 45.2 nm. B) Functionalization of the PEG-COOH-coated AuNP with PHA synthase yielded particles with a median diameter of 46.8 nm.

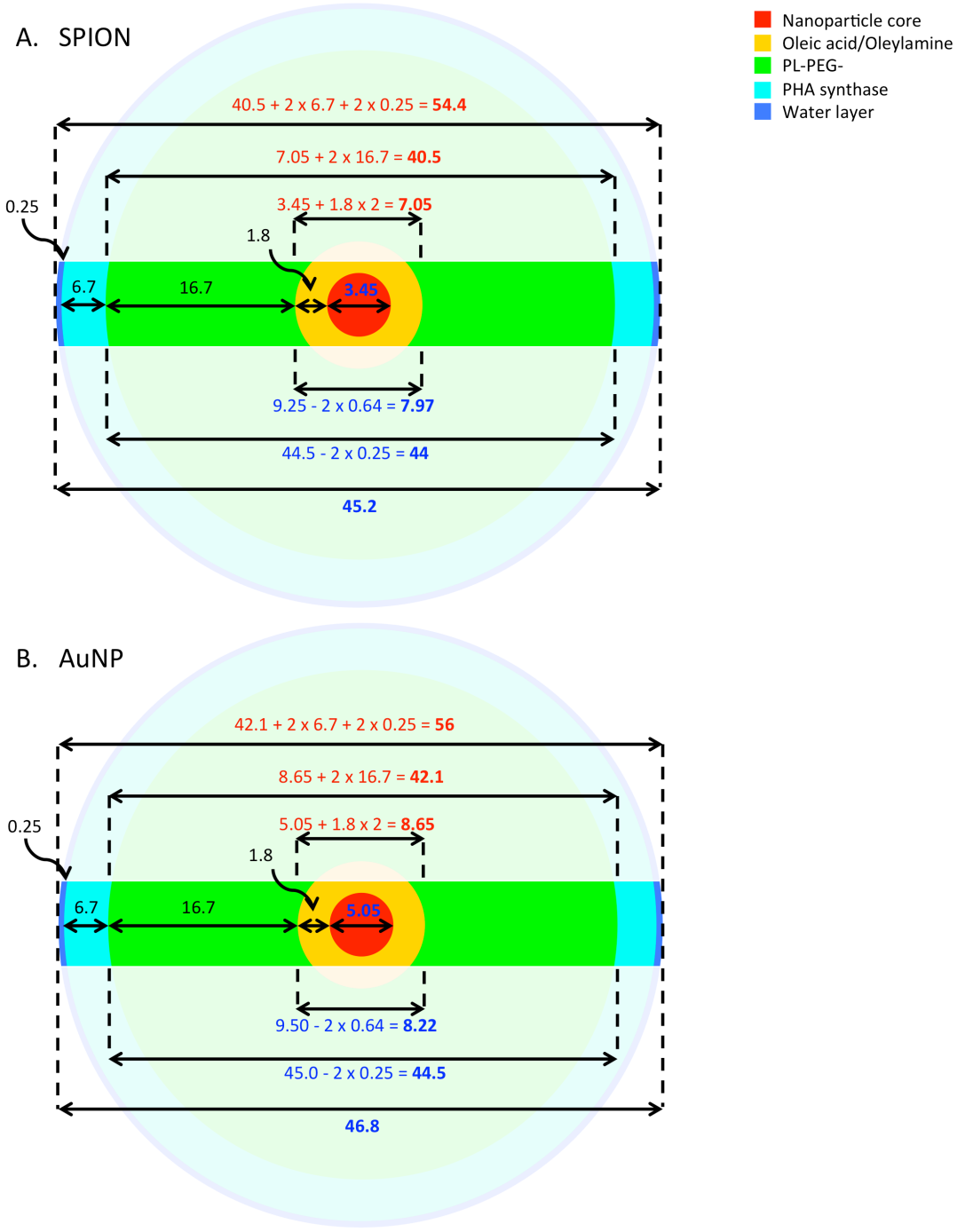

Figure 2.8: Summary of nanoparticle size analysis during functionalization

The expected (red text) and measured (blue text) diameters of the nanoparticles at each step of the functionalization process are summarized for both SPION (A) and

AuNP (B). Numbers in black text are the estimated sizes contributed by each component comprising the different materials coating the nanoparticles. All numbers are in units of nanometers. Discrepancies between expected and measured results of less than 4 nm were observed with the exception of the expected size increase after the conjugation of PHA synthase to the nanoparticles where measured results where ~10 nm smaller than expected. A likely explanation for this discrepancy is that the number of PHA synthase per particle is not homogenous and the observed size distribution is comprised of a mixture of particles with and without conjugated PHA synthase.

2.4.5. Synthesis of 3HB-CoA

The yield of 3HB-CoA synthesis from a single run was determined to be 46% as determined from Ellman's reagent assay. Under the reaction conditions, 100% of the free coenzyme A (32.6 μmoles) was expected to have reacted(*99*) thus based on the yield of 3HB-CoA, up to 54% (17.6 μmoles) of free coenzyme A remained in the product, likely due to 3HB-CoA hydrolysis during the reaction and processing or due to loss of product during the ether extraction of excess lactone. In order to minimize the loss of 3HB-CoA due to its hydrolysis(*98*), the ether extraction of excess lactone was the only purification step performed. Thus, in addition to 3HB-CoA, the final product was likely to contain up to 17.6 μmoles of free coenzyme A based on the measured yield and some amount of 4-hydroxybutanoic acid from hydrolyzed β-butyrolactone as well as 0.2 M $KHCO_3$. Of these constituents, only free coenzyme A could cause deleterious effects to PHB granule formation as it is known to inhibit PHA synthase activity(*104*). Nevertheless, the product of this reaction allowed for PHB polymerization in our studies.

2.4.6. Production and properties of nanoparticle coated PHB

Upon the addition of 3HB-CoA to nanoparticle-PHA synthase conjugates, PHB polymer was formed and grew to polydisperse spherical granules with diameters up to 1500 nm in diameter (see Figure 2.9 A-C for SPION-PHB granules and Figure 2.10 A-C for AuNP-PHB granules). As can be seen in the TEM images, these granules are coated with nanoparticles that appear as round structures with dark spots derived from electron-dense nanoparticles on their surface. The incorporation of nanoparticles within the PHB granule was not observed through our TEM analysis and it is possible that the nanoparticle-coated granules only result from a population of nanoparticle-PHA synthase conjugates that have few PHA synthase per nanoparticle;

in this case, PHA synthase would have less steric hindrance and can more easily participate in granule formation.

The presence of PHB was also confirmed through fluorescence microscopy of Nile red stained PHB (see Figure 2.9 D for SPION-PHB granules and Figure 2.10 D for AuNP-PHB granules). Nile red exhibits little fluorescence in hydrophilic mediums yet brightly fluoresces upon incorporation into hydrophobic matrices. The observation of Nile red-stained granules via fluorescence microscopy indicates that these nanoparticle-coated granules maintain a hydrophobic core as in native PHB granules. The resulting nanoparticle coating is consistent with the proposed mechanism of PHB granule formation and a possible assembly mechanism based on PHB granule formation is diagramed in Figure 2.11.

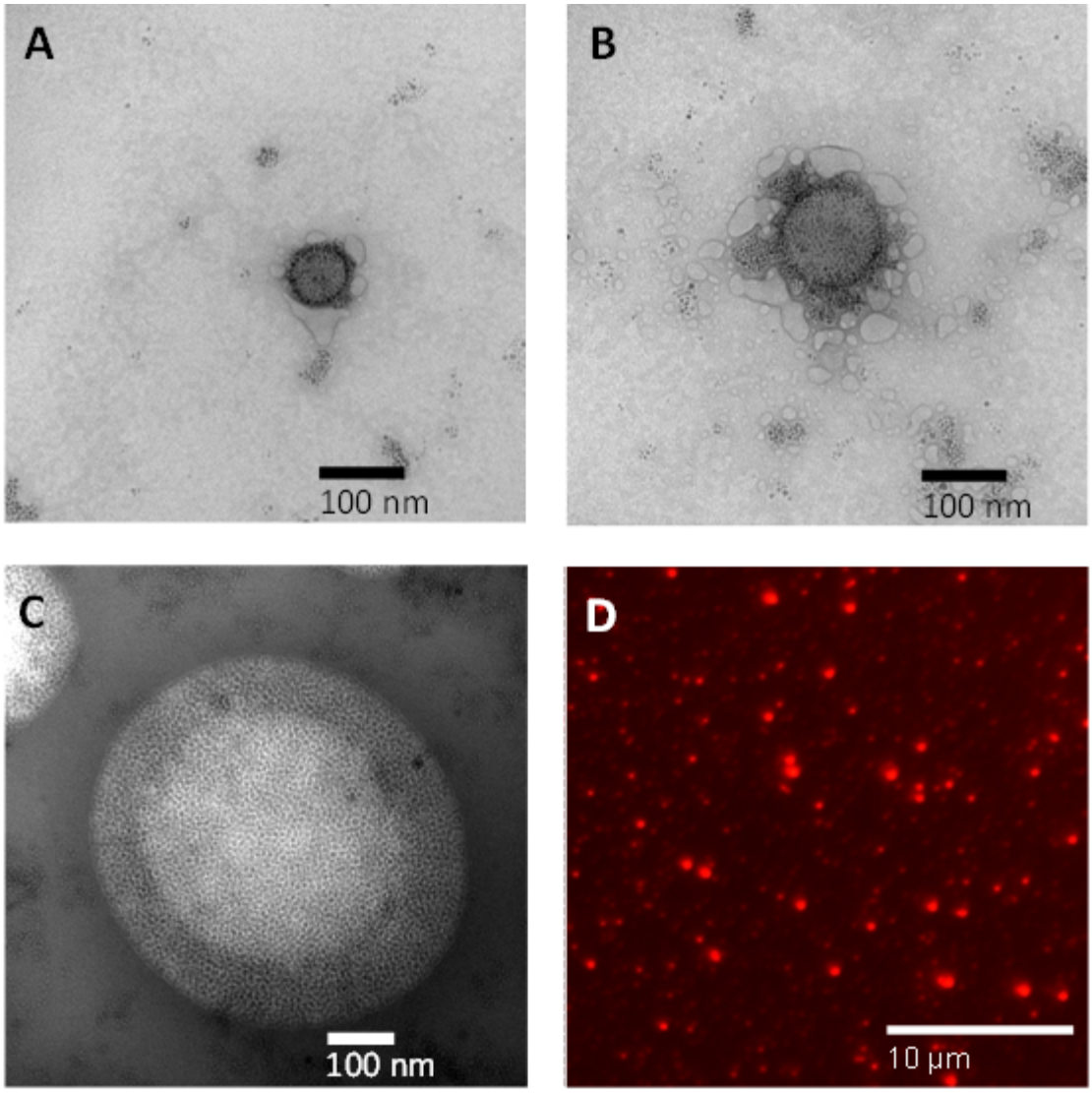

Figure 2.9: SPION-coated PHB granules

PHB polymerization from SPION-PHA synthase conjugates produced SPION-coated PHB granules. TEM analysis of polymerized material revealed SPION-coated PHB granules (Images A, B, and C) of various sizes with diameters of up to 1.5 µm. Image D shows a micrograph of Nile red-stained SPION-coated PHB granules imaged via fluorescence microscopy and indicate that the AuNP-coated granules maintain a hydrophobic core as in native PHB granules.

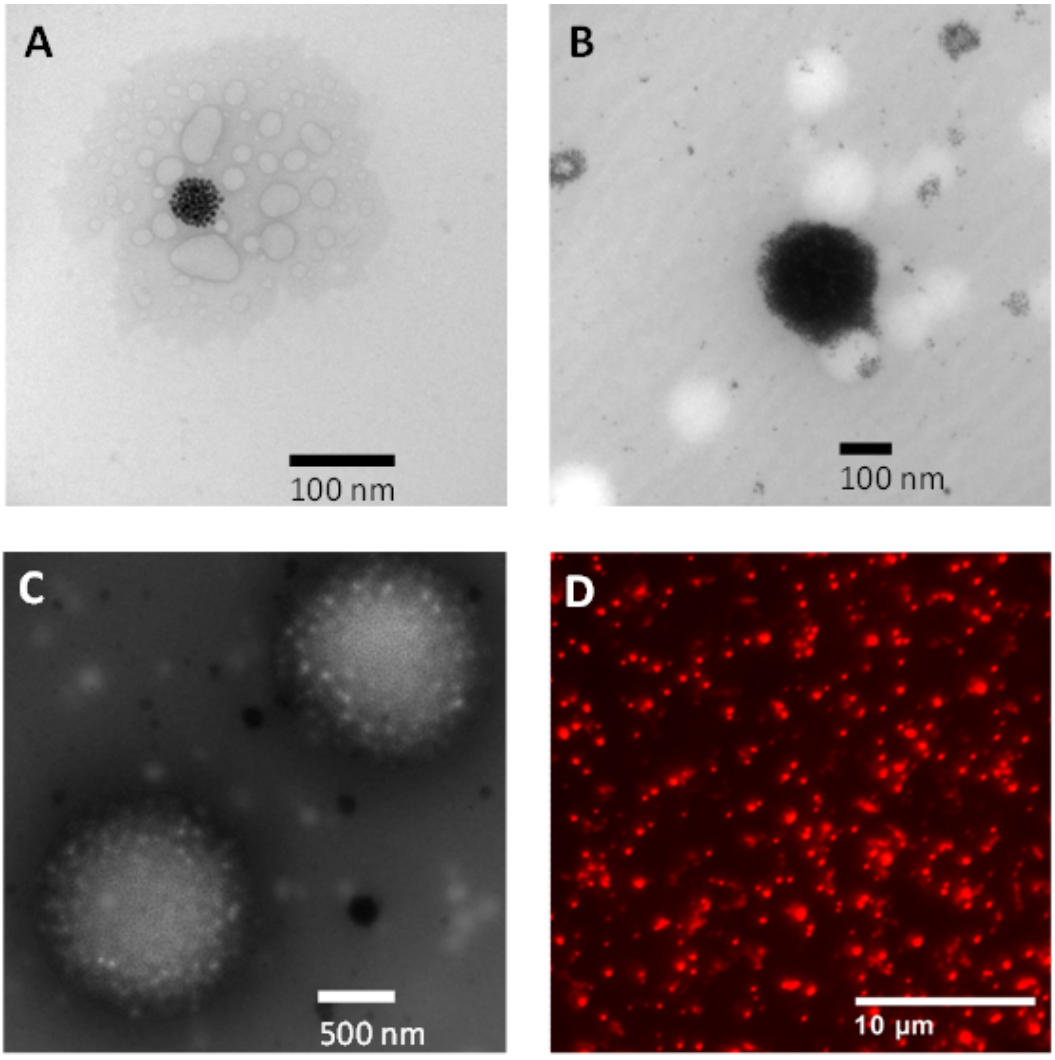

Figure 2.10: AuNP-coated PHB granules

PHB polymerization from AuNP-PHA synthase conjugates produced AuNP-coated PHB granules. TEM analysis of polymerized material revealed AuNP-coated PHB granules (Images A, B, and C) of various sizes with diameters of up to 1.5 µm. Image D show a micrograph of Nile red-stained AuNP-coated PHB granules imaged via fluorescence microscopy and indicate that the AuNP-coated granules maintain a hydrophobic core as in native PHB granules.

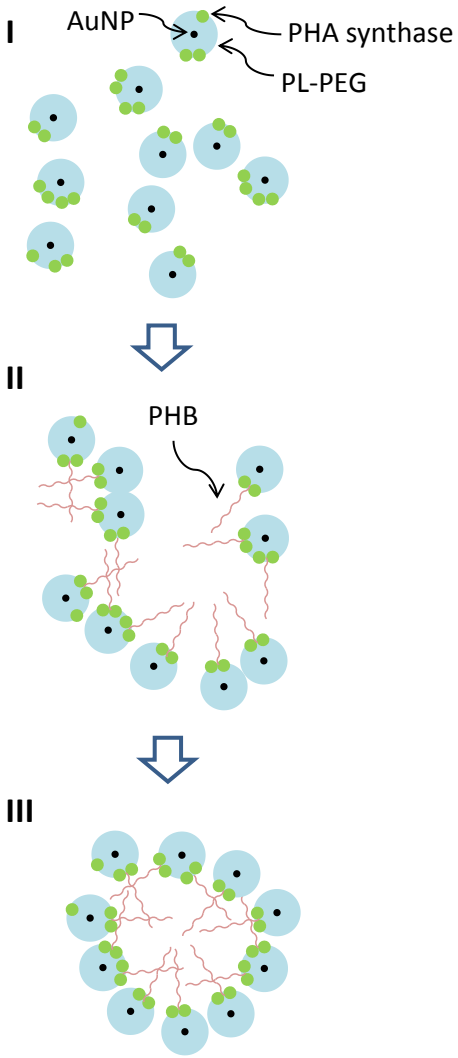

Figure 2.11: Proposed mechanism for nanoparticle-coated PHB granule formation

From PHA synthase-conjugated nanoparticles (I) PHB polymer chains may form (II) and PHB chains then begin to aggregate via hydrophobic interactions between PHB leading to the formation of PHB granules with nanoparticles remaining on their surface (III).

2.5. Conclusions

In this work, ~45 nm nanoparticle-PHA synthase conjugates were constructed with the capability of polymerizing PHB. PHB polymerization from these conjugates resulted in nanoparticle-coated PHB granules offering a new means for producing functionalized PHB particles. The resulting nanoparticle coating of PHB granules is consistent with the native *in vitro*-polymerized PHB granule structure in which PHA synthase remains on the granule surface. In an analogous manner to the formation of native PHB granules, PHB granule formation from nanoparticle-PHA synthase conjugates is likely derived from the polymerization of PHB from PHA synthase on the surface of nanoparticle-conjugates leading to the coalescence of PHB chains via hydrophobic interactions. The coalescence of polymerizing nanoparticle-conjugates leads to the formation of PHB granules with nanoparticles remaining on their surface.

A wide range of biomolecules have been immobilized on the surface of PHB granules that have allowed for using functionalized granules in applications ranging from protein purification(*42, 105*) to cancer cell targeting(*44, 52*). Of the PHB granule functionalization strategies employed to date, only one approach has allowed for coating PHB granules with inorganic materials(*45*). In these studies, *Escherichia coli* was made to express PHA synthase fused to gold- and silica-binding peptides. The formation of PHB granule inclusions within the *Escherichia coli* resulted in self-assembly of PHB granules displaying binding sites for gold or silica. These beads could then be decorated with gold or silica nanoparticles after extraction of the *in vivo*-produced granules from *Escherichia coli*.

In contrast to *in vivo* granule formation, our *in vitro* approach allows for the direct assembly of nanoparticle-coated PHB granules in a single-step process. Furthermore, *in vitro* granule formation may allow for straight-forward means of

controlling PHB granule size(*52, 106*). In contrast, *in vivo* approaches for PHB granule size control require regulation of GAP expression within the host organism – a feat that has not yet been demonstrated(*15*). On the other hand, alternative approaches to nanoparticle coating of PHB granules may be achieved via decoration of synthetically produced PHB particles with nanoparticles conjugated to GAPs other than PHA synthase. Such approaches may allow for a greater degree for size control as has been demonstrated for synthetic PHB particle production(*27*). Yet, while PHB granules with diameters of less than 1 micron may be readily produced via biosynthetic means(*52, 106*), only one synthetic approach (i.e. that does not employ PHA synthase) has demonstrated the production of nano-sized PHB particles with the majority of synthetic approaches resulting in PHB particles with diameters that are greater than 1 micron (Table 1.2).

The arrangement of nanoparticles on the PHB granule surface may result in nanoparticle-aggregation-based phenomena that may be applicable in biomedical applications. The following chapters explore the possible MRI-based applications of SPIO-coated PHB granules and the spectroscopic-based applications of AuNP-coated PHB granules.

Chapter 3 – Superparamagnetic iron oxide nanoparticle-coated PHB granules

3.1. Abstract

Polyhydroxyalkanoate (PHA) synthase attached to superparamagnetic iron oxide nanoparticles (SPION) produce poly(3-hydroxybutyrate) (PHB) upon the addition of 3-hydroxybutyrate-CoA, and then coalesce to form nano- to micron-sized SPION-coated PHB granules. The SPION-coated PHB granules that are potential MRI contrast agents with enhanced imaging capabilities afforded by PHB mediated aggregation of SPION that resulted in SPION-coated PHB that exhibited ~2-fold improvement in T2 relaxivity (168 s^{-1} $mmol^{-1}$ Fe) when compared to free SPION conjugated to PHA synthase (87.5 s^{-1} $mmol^{-1}$ Fe). Control of PHB granule size is also demonstrated via the addition of the surfactant Tween 20 allowing for producing PHB granules down to 100 nm in diameter. In addition, SPION-PHA synthase are shown to allow for controlled retention of SPION within porous matrices via PHB polymerization where *in situ* polymerization of PHB from SPION-PHA synthase within agarose gel was shown retain up to 4.2-times greater amount of SPION when compared to SPION-PHA synthase samples that did not undergo polymerization. The SPION-PHA synthase conjugates described herein could find use as advanced contrast agents with a high degree of control for their biodistribution based on the tuning of their size and the capability for their localized retention in porous matrices.

3.2. Introduction

Superparamagnetic iron oxide nanoparticles (SPION) are widely used in biomedical imaging as MRI contrast agents due to their localized shortening of spin-spin (T2) proton relaxation times(*75, 76, 107*). Early studies of SPION-based contrast agents found applicability in imaging of the liver, spleen, and bone marrow due to their sequestration by cells of the reticuloendothelial system (RES) (*108-111*). The

applicability of these initial SPION contrast agents was limited due to rapid liver uptake and short blood half-life. More recent developments modifying the physicochemical properties of SPION materials have allowed for expansion of their biodistribution, pharmacokinetics, and contrast properties(*112-114*). Nevertheless, most applications of SPION contrast agents have relied on the passive distribution that results from the physicochemical properties of the particles. Approaches that aim to instead actively control SPION biodistribution have primarily involved antigen targeting via antibodies conjugated to SPION. In addition, a recently reported alternative approach involved SPION retention in the articular cavity by external magnetic field(*115*).

Recent trends in SPION-based contrast agent development have involved nanoparticle aggregation-based approaches that have revealed further enhancements in their MRI contrast properties(*116-119*). The local T2 proton relaxivity of SPIO nanoparticles can be modified through aggregation of the SPION providing control of the ultimate nanoparticle aggregate size and magnetic properties with the end goal of their optimization for specific imaging applications(*116-118, 120*). Aggregation of superparamagnetic materials affects their transverse relaxivity by manipulating the magnetic field gradients through which water diffuses(*116*) and SPIO nanoparticle aggregates have been recently studied as MRI contrast agents as agents with enhanced properties for T2-weighted MRI(*119, 120*).

In this study, the effects of PHB-mediated aggregation of SPION from SPION-PHA synthase conjugates were examined by comparing the T2 relaxivity of SPION-coated PHB to that of SPION-PHA synthase conjugates prior polymerization. In addition, the ability to control SPION-PHB granule size is examined and the ability to control SPION retention within porous matrices is demonstrated through *in situ* polymerization of PHB within agarose gel.

3.3. Experimental

3.3.1. Controlled SPION retention

Agarose gel matrices with pore sizes of ~150 nm and ~400 nm were prepared casting the gel in square plastic dishes with a gel comb embedded in the agarose solution. Agarose solutions were prepared following Narayanan, et al.(*121*); briefly, high melt agarose powder (IBI Agarose, Shelton Scientific, Inc, Shelton, CT) was dissolved in deionized water at 0.75% and 2% (w/v) agarose concentrations and heated in an incubator oven for 30 min at 110 °C. The solutions were then stirred and sonicated for one hour and held in the oven for an additional 30 min. The hot solutions were then poured into the casting apparatus and were allowed to set while incubating at 35 °C. Based on this procedure, the gel pore sizes were expected to be in the order of 150 nm for 2% (w/v) agarose and 400 nm for 0.75% (w/v) agarose(*121*).

After the gels had solidified, the comb was removed and 5 uL of SPION-PHA synthase samples at OD_{500} = 0.25 were added to wells in the gel. The SPION-PHA synthase was then drawn into the gel by placing a magnet beneath the gel cast and placing the sample at 4 °C for 18 hrs. Next, 2 µL of 50 mM 3HB-CoA or water was added the wells allowed to incubate for 12 hrs at room temperature. Samples with and without substrate were prepared in triplicate. After incubation, the wells were excised from the bulk of the agarose gel by cutting out 1 cm^2 portions of gel from the top, each containing a well at the center of the 1 cm^2 area. Gel samples were then placed upright and photographed from the side with a digital camera. The gel samples were then submerged in 50 mM phosphate buffer, pH 7 within sealed containers and were placed on a rocking table at room temperature. At hourly intervals, the samples were: removed from the containers, photographed, replaced in the containers with fresh

buffer, and left to rock again. Photographs were then analyzed via densitometry using Image J gel analysis software.

3.3.2. T2 measurements and analysis

T2 measurements were conducted via collaborative efforts with Richard Wong, PhD Candidate in Professor Yi Wang's laboratory, at the Cornell University MRI Laboratory Group, Weill Medical College, New York, NY. PCR tubes (250 μL) were filled with serial dilutions of SPION-PHA synthase at Fe concentrations ranging from 0.00-0.33 mM having undergone and not undergone polymerization. Imaging was conducted at 3 Tesla (GE Signa Excite, GE Healthcare, Uppsala, Sweden) and the imaging protocol consisted of a T2-weighted spin-echo sequence (TR 3000 ms, variable TE: 14, 25, 50, 75, 100, 150, 200, 250, 300 ms, 9 individual scans). The slice thickness was 5 mm with a field of view (FOV) of 8 cm, Frequency x Phase of 256 x 256, Phase FOV of 0.5, and 1 number of excitations (NEX). The MR images obtained at various echo times (TE's) were cropped to the contents of the PCR tubes and processed to obtain R2 (1/T2) maps and the experiment was repeated four times. Figure 3.1 shows a representative MRI image from which T2 analysis was conducted.

Determination of iron concentration of SPION samples was conducted by third party services provided by M.A. Rutzke, PhD, Cornell University, Department of Food Science, Ithaca, NY(*122-125*). Briefly, samples were digested with concentrated nitric acid at 120 °C until dry followed by a 50/50 mixture of concentrated nitric acid and perchloric acid that was heated at 220 °C until again dry. After cooling, the resulting ash was dissolved with concentrated HCl, diluted with 5% HNO_3 and analyzed with an axially viewed inductively coupled plasma (ICP) trace analyzer emission spectrometer (ICAP 61E trace analyzer, Thermo Electron, Waltham, Ma) with the replacement of the transfer optics with a short depth of field transfer optics to

reduce matrix effects. With these measurements, an OD vs Fe molarity plot was obtained and used to determine the Fe molar concentration via OD measurements.

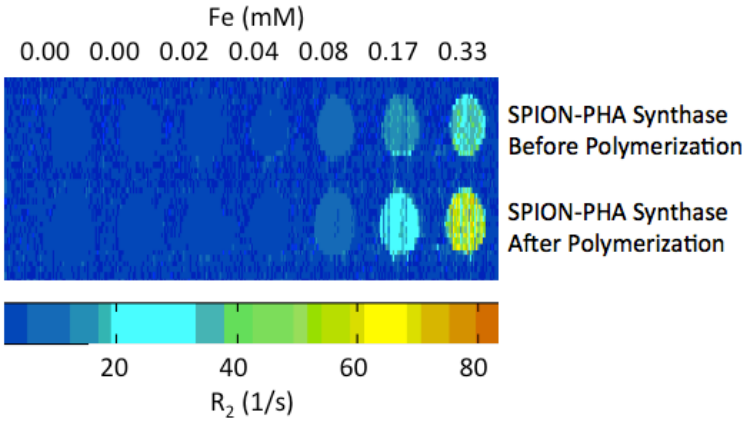

Figure 3.1: MRI analysis of SPION-PHA synthase before vs. after polymerization

The T2 relaxivity of SPION-PHA synthase and SPION-coated PHB was derived by MRI analysis of serial dilutions of each of the materials. PCR tubes were filled with serial dilutions of SPION-PHA synthase (top row) and SPION-PHA synthase with the addition of 3HB-CoA (bottom row). The tubes were then imaged via MRI using an imaging protocol that consisted of a T2-weighted spin-echo sequence. The figure shows that T2 (1/R2) decrease more rapidly with increasing Fe concentration for SPION-coated PHB granules vs. SPION-PHA synthase conjugates thus exhibiting an improvement in T2 relaxivity of SPION-coated PHB granules over SPION-PHA synthase.

3.3.3. PHB granule size control

Samples of PHA synthase (0.1 mg/mL) were prepared with the addition of the surfactant polyoxyethylene sorbitan monolaurate (Tween 20) at concentrations of 0%, 0.025%, 0.05%, 0.1% v/v (Tween 20 Enzyme Grade, Thermo Fisher Scientific, Rockford, IL). 2.5 mM of 3HB-CoA was then added to each sample and PHB granule growth was monitored via DLS (Malvern Zetasizer Nano, Malvern Instruments, Worcestershire, United Kingdom) at 25 °C. To examine the effect of Tween 20 on SPION-PHB granule formation, samples of 0.1 mg/mL SPION-PHA synthase (based on protein concentration) were prepared with the addition of Tween 20 at 0%, 0.025%, and 0.1% v/v and the subsequent addition of 5 mM 3HB-CoA. Samples were then imaged via TEM after 1 hr of incubation at room temperature.

3.4.Results and Discussion

3.4.1. PHB-mediated controlled SPION retention

In order to examine the potential for controlled retention of SPIO in porous matrices, SPION-PHA synthase conjugates were magnetically driven into 2% and 0.75% agarose gel matrices corresponding to ~150 nm and ~400 nm-diameter pore sizes, respectively, and representing a range of possible tissue pore dimensions(*121*). After 156 hrs, samples subjected to *in situ* polymerization within the gel resulted in 3.6-times greater retention of SPION in 2% agarose and 4.2-times greater retention in 0.75% agarose when compared to un-polymerized SPION-PHA synthase. A biphasic release of SPION was observed with a more rapid release of SPION over the first 40 hrs and 60 hrs for 2% (Figure 3.2) and 0.75% (Figure 3.3) agarose, respectively, followed by a slower rate of release. Two phase exponential decay fits of the data revealed that the half-life of the earlier and later decays were 1.5 and 1.2-fold longer,

respectively, for samples that had undergone polymerization in 0.75% agarose and 1.9 and 1.5-fold longer, respectively, for samples that had undergone polymerization in 2% agarose. The observed biphasic release profile may be due to an initial more rapid release of SPION not associated with PHB followed by a slower release of aggregated particles.

This PHB-mediated controlled retention of SPION in porous matrices may allow for site-specific sustained dosage of SPION in tissue systems. SPION-PHA synthase, which are 50 nm in diameter (Figure 2.8), may be able to penetrate into biological tissues with pores of suitable dimensions and then SPION could be entrapped in the tissue via *in situ* polymerization within the tissue. This mechanism might be suitable for application within capillaries that possess holes or 'fenestrae' (~50-100 nm diameter) predominantly on their venous limbs or in the interstitial tissue where the mean diameters of pores in the muscle and intestine are on the order of 60-120 nm(*126*).

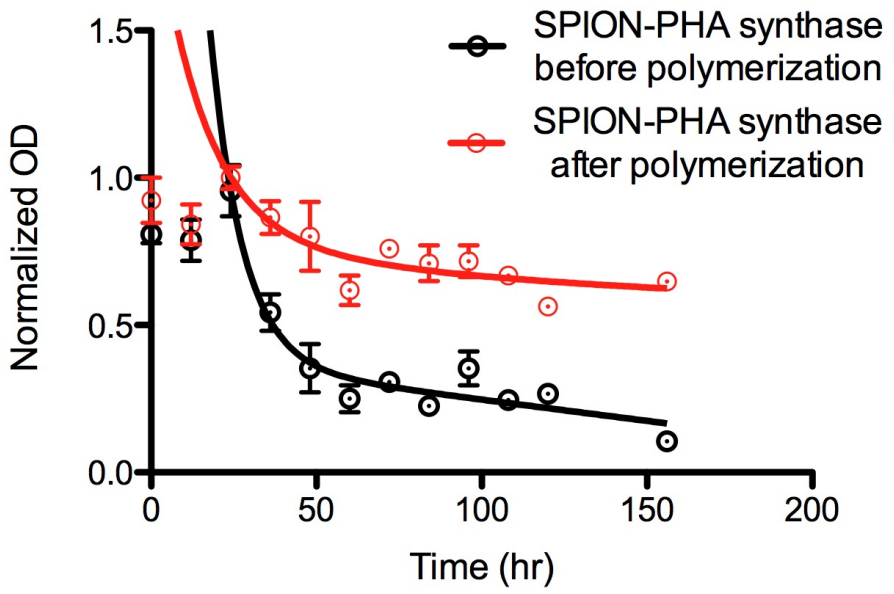

Figure 3.2: *In situ* PHB polymerization-mediated SPION retention in 0.75% agarose

SPION-PHA synthase conjugates were magnetically driven into 0.75% agarose gel corresponding to ~400 nm-diameter pore size and the subsequent diffusion of SPION out of the gel was examined via densitometry of gel images. A biphasic release of SPION was observed when comparing the optical density of samples having undergone in situ polymerization of PHB within the gel (red) to that of samples that did not undergo polymerization (black) and two phase exponential decay fits of the data during the later phase of release were used to determine and compare SPION retention and rates of release. The half-life of the earlier and later decays were 1.5 and 1.2-fold longer, respectively, for samples that had undergone polymerization and after 156 hrs, samples subjected to in situ polymerization within the gel resulted in 4.2-times greater retention when compared to un-polymerized SPION-PHA synthase.

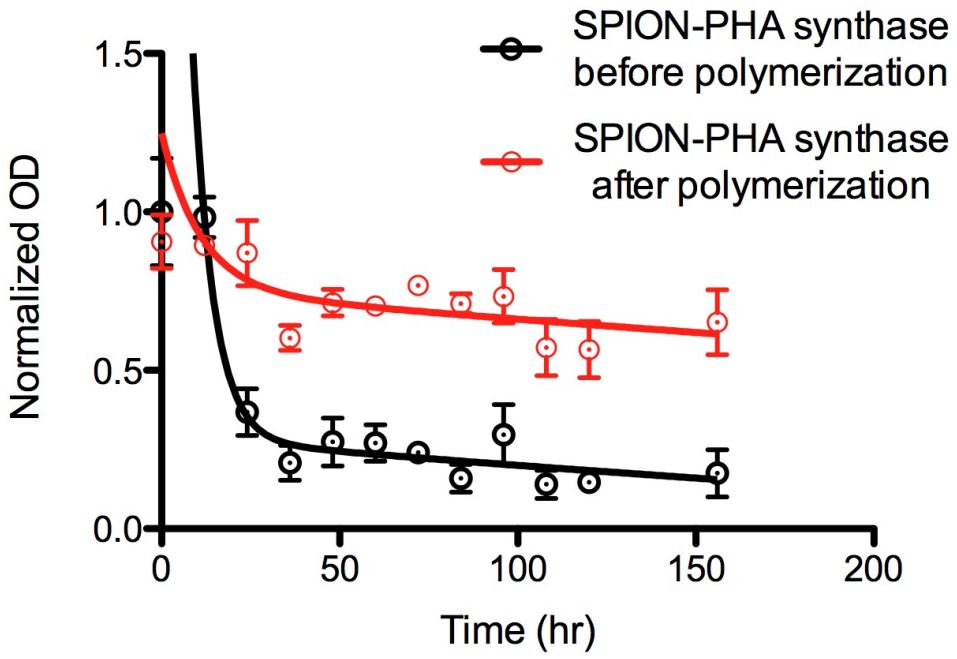

Figure 3.3: *In situ* PHB polymerization-mediated SPION retention in 2% agarose

SPION-PHA synthase conjugates were magnetically driven into 2% agarose gel corresponding to ~150 nm-diameter pore size and the subsequent diffusion of SPION out of the gel was examined via densitometry of gel images. A biphasic release of SPION was observed when comparing the optical density of samples having undergone in situ polymerization of PHB within the gel (red) to that of samples that did not undergo polymerization (black) and two phase exponential decay fits of the data during the later phase of release were used to determine and compare SPION retention and rates of release. The half-life of the earlier and later decays were 1.9 and 1.5-fold longer, respectively, for samples that had undergone polymerization and after 156 hrs, samples subjected to in situ polymerization within the gel resulted in 3.6-times greater retention when compared to un-polymerized SPION-PHA synthase.

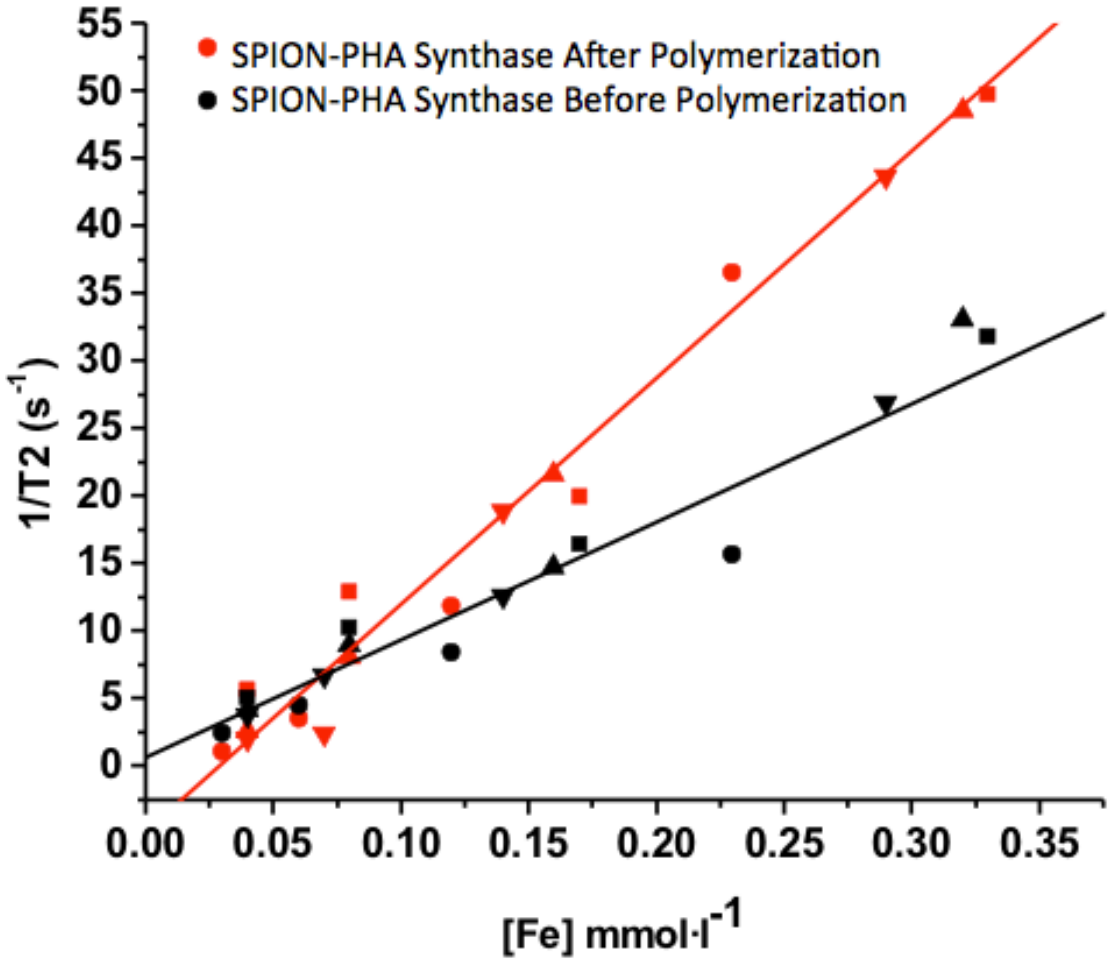

Figure 3.4: Relaxivity of SPION-PHA synthase before vs. after polymerization

Based on MRI measurements as depicted in Figure 3.1, R2 (1/T2) values at varying SPION-PHA synthase concentrations with (red) and without (black) the addition of 3HB-CoA were used to plot R2 values vs. iron concentration from four different sets of experiments. The lines on the plot are the averages of linear fits of the data for each experiment and whose slopes were used to determine the T2 relaxivity of each material. SPION-coated PHB granules exhibited 1.92 ± 0.178-fold higher T2 relaxivity than SPION-PHA synthase.

3.4.2. Enhanced T2 relaxivity of SPION-coated PHB granules

The T2 relaxivity of SPION-PHA Synthase were analyzed with and without PHB polymerization (Figure 3.4). Increasing concentrations of nanoparticles were imaged via MRI (Figure 3.1) in order to calculate R2 maps. Figure 3.4 shows the R2 (1/T2) values plotted versus iron concentration.

The relaxivity was determined from linear fits of the data and resulted in 168 ± 29.1 s^{-1} $mmol^{-1}$ Fe for polymerized samples vs. 87.5 ± 3.49 s^{-1} $mmol^{-1}$ Fe for SPION-PHA synthase without polymerization, comparing favorably with FDA approved SPIO-based contrast agents among which the highest relaxivity is 160 s^{-1} $mmol^{-1}$ (*127*). The SPION-coated PHB thus exhibited a 1.92 ± 0.178-fold improvement in T2 relaxivity when compared to SPION-PHA synthase.

Contrast enhancement due to SPION aggregation has been extensively studied in the context of compact clusters(*116-118, 120*) and it has been shown that compact clusters of SPION induce relaxation equivalent to similarly sized single particles(*128*). The SPION-PHB granules form a SPION-shell rather than compact clusters and while several studies have described similar structures(*129-132*), none have examined the specific effects of a magnetic shell structure on T2 relaxivity. Nevertheless, similar shell structures have been found to exhibit a single dipole with behavior similar to single larger magnetic particles when exposed to external magnetic fields(*132*). Interestingly, magnetic shell structures composed of SPION have also been shown to deform under external magnetic fields(*129*). If this phenomenon is also exhibited by SPION-PHB granules, this may allow for controlled release of encapsulated material within the PHB core thereby providing a means for magnetically-triggered drug delivery.

3.4.3. Size control

The addition the surfactant Tween 20 allowed for controlling PHB granule size (Figure 3.5). When analyzing the granule size vs. Tween 20 concentration, increasing the Tween 20 concentration during polymerization resulted in decreased granule size following a first order exponential decay ($R^2 = 0.997$) (Figure 3.6). Under the conditions of the experiment, the PHB granule diameter could thus be controlled down to ~100 nm. Based on these results, SPION-PHA synthase samples were incubated with 3HB-CoA and increasing amounts of Tween 20 in order to generate SPION-coated PHB granules of varying sizes. Similarly, a decreasing SPION-coated PHB granule size was observed (Figure 3.9) with increasing Tween 20 concentrations.

The mechanism by which Tween 20 is able to regulate PHB granule size is likely to be analogous to that of the GAP phasin. Phasins are amphiphilic proteins that serve to stabilize the granules and prevent their coalescence as well as the nonspecific binding to their milieu(*54*). Their hydrophobic region associates with the outer surface of the growing PHB granule thus reducing the available sites for additional the binding of PHA synthase and restricting the granule's growth. Phasins have been shown to influence granule size both *in vivo* and *in vitro*(*106, 133-136*). Overproduction of PhaP leads to the formation of many small granules(*137*) *in vivo* and, conversely, strains unable to produce any phasin protein accumulate only one single large PHA granule(*138*).

Control of particle size is an important aspect of nanoparticle development for *in vivo* applications(*139*) yet thus far only one aggregation-based methodology for SPION contrast agent optimization has demonstrated(*118*). Separately, the majority of studies involving PHB particle size control have been conducted with solvent-based methodologies for PHB particle synthesis(*27, 57*) and of these, only one study describes a method for the synthesis of sub-micron diameter PHB particles(*57*). On

the other hand, while *in vivo* produced PHB granules are typically sub-micron due to size restrictions of the host organism, size control of *in vivo*-produced granules has not yet been characterized(*15*). Nevertheless, methodologies for size control of *in vitro* enzyme-produced granules have been described where the addition of phasins, the GAP GA24 of *R. eutrophus*, and BSA have been shown to reduce PHB granule size(*106*). Another approach for *in vitro* biosynthesized PHB granule size control has been achieved via modulation of the substrate:enzyme ratio(*52*). The results in this study demonstrate that the surfactant Tween 20 offers an additional avenue for biosynthetic PHB granule size control and is the first such example that does not require the use of GAPs for controlling granule size.

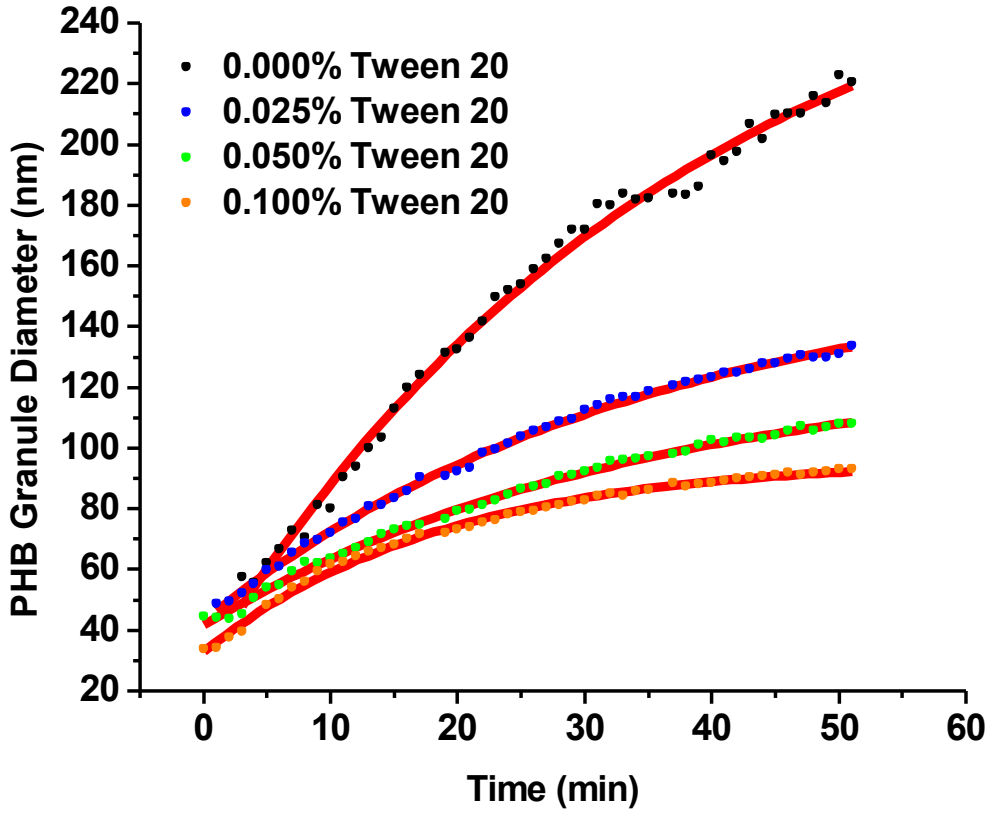

Figure 3.5: PHB granule size control

The growth of PHB granules in the presence of various amounts of Tween 20 (% v/v) was monitored via DLS. PHA synthase and 3HB-CoA were mixed at time zero and in the presence of increasing amounts of Tween 20 then the mixture was analyzed via DLS over time. The data was fit to first order exponential decays all of which exhibited an $R^2 > 0.99$ and it was observed that increasing the Tween 20 concentration resulted in a decrease in PHB granule size.

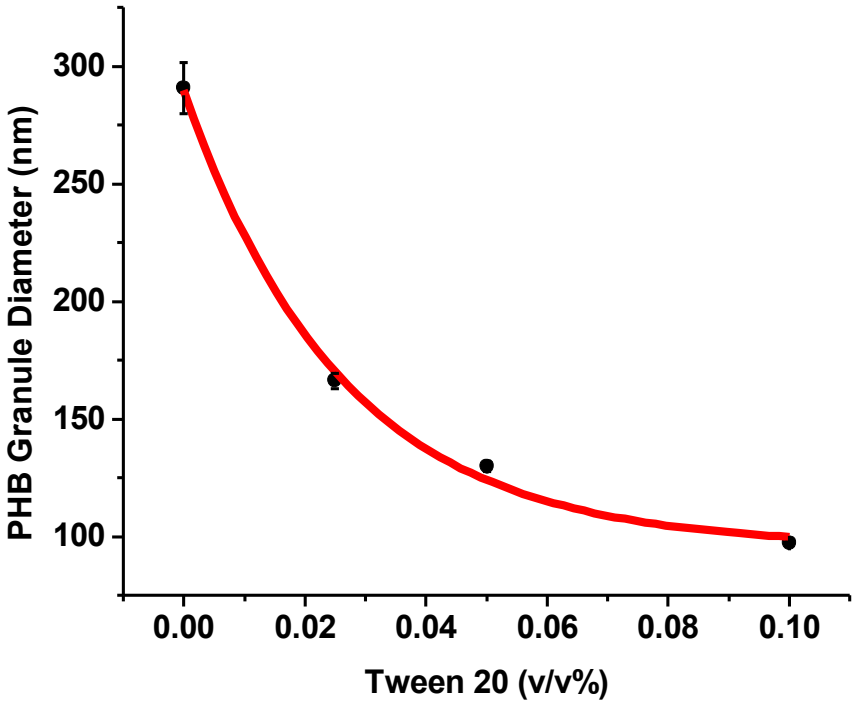

Figure 3.6: PHB granule size vs. Tween 20 concentration

In order to determine the relationship between Tween 20 concentration and steady-state PHB granule size, the asymptotes from each exponential decay fit shown in Figure 3.5 were plotted vs. Tween 20 concentration. Increasing the Tween 20 concentration during PHB polymerization resulted in decreasing PHB granule size following a first order exponential decay in PHB granule diameter vs. Tween 20 concentration (R^2 = 0.99744) with a minimum granule diameter approaching 100 nm at concentrations of Tween 20 greater than 0.10% (v/v). The mechanism underlying this observed relationship is likely analogous to that of the amphiphilic GAP phasin that serves to stabilize in vivo-produced granules via the association of their hydrophobic region with the outer surface of PHB granules thus reducing the available sites for additional the binding of PHA synthase and restricting the granule's growth.

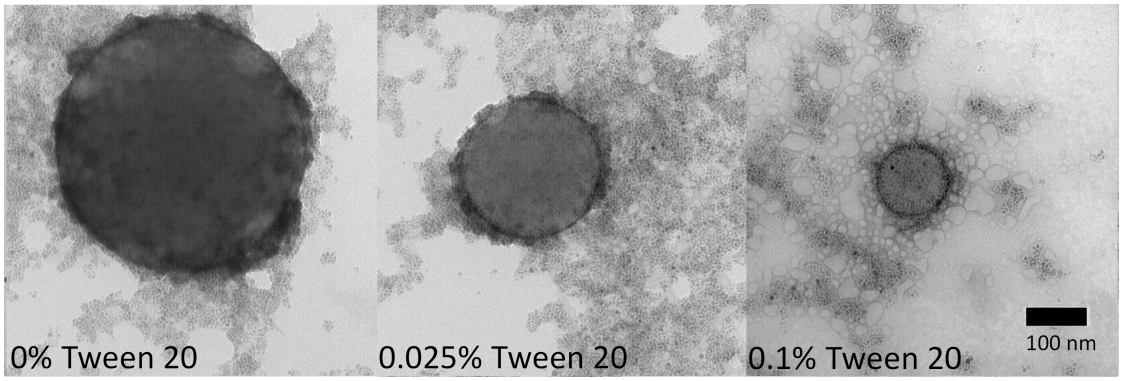

Figure 3.7: SPION-coated PHB granule size control

SPION-coated PHB granules were grown to various sizes by varying the concentration of Tween 20 present during PHB polymerization. SPION-PHA synthase conjugates were mixed with 3HB-CoA in the presence of Tween 20 at 0, 0.025, and 0.1% (v/v). The figure shows TEM images SPION-coated PHB granules formed in the presence of the varying concentrations of Tween 20. SPION-coated PHB granules of decreasing diameter were observed with increasing Tween 20 concentrations.

3.5.Conclusions

In situ PHB polymerization from SPION-PHA synthase conjugates within agarose gel resulted in increased SPION retention within the gel when compared to un-polymerized SPION-PHA synthase. This PHB-mediated controlled retention of SPION in porous matrices may allow for site-specific sustained dosage of SPION in tissue systems. When compared to SPION-PHA synthase, SPION-coated PHB granules exhibited enhanced T2 relaxivity properties reaching 168 s^{-1} $mmol^{-1}$, comparing favorably with FDA approved SPIO-based contrast agents among which the highest relaxivity is 160 s^{-1} $mmol^{-1}$ [*127*]. Finally, the addition of Tween 20 during *in vitro* PHB polymerization resulted in a decrease in PHB granule diameter allowing for control of the granule size.

Thus far only one aggregation-based methodology for SPION contrast agent size control has demonstrated(*118*). In addition, few studies have investigated means of controlling the size of *in vitro*-produced biosynthetic PHB granules(*52, 106*). While the studies described in this chapter offer an additional means of controlling SPION-aggregate and PHB granule size, this system requires further characterization in order to determine aspects such as the size polydispersity of the resulting PHB granules. The surfactant-based size control methodology described herein deviates from the more 'bio-friendly' biomolecule-based reaction conditions that differentiate biosynthetic means of PHB granule production from synthetic means that employ organic solvents, nevertheless, Tween 20 is known to be nontoxic and is employed in the food processing and pharmaceutical industries(*140*). Furthermore, the use of Tween 20 as opposed to GAPs for controlling PHB granule size is advantageous given that the surfactant is commercially available.

Aggregation-based methodologies for the development of SPION-based enhanced contrast agents have shown promise in broadening the applicability of such materials(*116-120*) and the PHB polymerization-mediated aggregation capabilities described herein may allow for optimization of the SPION-PHB granules in specific imaging applications. *In situ* polymerization of locally injected SPION-PHA synthase and the size-control of SPION-coated PHB granules for use in systemic administration could offer two separate avenues for controlling biodistribution and clearance based on PHB polymerization-mediated SPION aggregation. With regard to *in situ* polymerization-mediated SPION retention, an advantage of this system when compared to SPION retention from the application of localized magnetic fields(*115*) is that there is no need for equipment that would need to be constantly applied for causing SPION retention. On the other hand, while it may be feasible to systemically administer SPION and cause their site-specific accumulation via external magnetic field, our polymerization-mediated retention approach may be limited to simultaneous local injection of SPION-PHA synthase and 3HB-CoA since the substrate would need to be applied locally and would quickly diffuse from the injection site.

With regard to size-control of SPION-coated PHB granules for systemic administration, a particular advantage of SPION-coated PHB granules may lie in the nanoparticle coating. PEGylated particles have generally resulted in longer circulation times due to their prevention of nonspecific interactions with proteins through the hydrophilicity and steric repulsion effects provided by PEG resulting in reduced opsonization and complement activation(*141-144*). Nevertheless, smaller PEGylated nanoparticles (< 100 nm) have been shown to have longer clearance than larger PEGylated nanoparticles (100 nm < x < 500 nm); an effect that has been attributed to increased PEG packing density on smaller nanoparticles(*144, 145*). In light of these observations, since SPION-coated PHB granules are coated with individually

PEGylated ~45 nm SPION, the PEG packing density that coats PHB granules is expected to stay constant with varying PHB granule size. This effect may hold an advantage when compared to other PEGylated particles of varying sizes in that the prevention of opsonization may facilitate hepatocyte-mediated rather than Kupffer cell-mediated clearance of the grnaules(*146*). In this case, the granules would follow a more direct elimination route via excretion into the bile rather than sequestration within Kupffer cells that retain foreign materials until it can be eliminated via intracellular degradation.

Chapter 4 – Gold nanoparticle-coated PHB granules

4.1. Abstract

Polyhydroxyalkanoate (PHA) synthase attached to gold nanoparticles (AuNP) produce poly(3-hydroxybutyrate) (PHB) upon the addition of 3-hydroxybutyrate-CoA, and then coalesce to form nano- to micron-sized AuNP-coated PHB granules. These AuNP-coated PHB granules are potential theranostic agents that have enhanced imaging capabilities and are also capable of heating upon near-infrared (NIR) laser irradiation. The AuNP-coated PHB exhibited 11-fold enhancement in surface-enhanced Raman scattering over particles prior polymerization. Stained AuNP-coated PHB exhibited a 6-fold enhancement in fluorescence intensity as well as a 1.3-fold decrease in photobleaching rate when compared to PHB granules alone. The granules were also shown to emit heat when illuminated at 808 nm with a 3.9-fold increase in heating rate when compared to AuNP-PHA synthase alone. In addition, NIR laser illumination of fluorescent doxorubicin-loaded AuNP-PHB granules resulted in loss of fluorescence possibly due to destruction of the PHB granule structure, providing a potential means of burst drug delivery from AuNP-PHB granules.

4.2. Introduction

Gold nanoparticles have been employed in a variety of diagnostic and therapeutic applications. Radioactive conjugates of colloidal gold have been used in the treatment of human cancers since the 1940s(*147*) where systemic administration of colloidal 'radiogold' was first used in the treatment of leukemias and lymphomas. These particles were naturally taken up by the RES cells in the liver, the spleen, and the bone marrow(*147, 148*) and their toxicity was attributed to radiation effects and not to the gold particles(*147, 148*). In more recent studies, RES clearance of gold particles has been shown to be mediated via uptake by Kupffer cells in the liver(*149,*

150). Long-term safety data and observed clearance routes make gold nanoparticles a good candidate for *in vivo* diagnostic and therapeutic applications(*151*).

4.2.1. SERS-based applications

The surface plasmon resonance of AuNPs is sensitive to the surrounding environment of the particle and is strongly dependent on the proximity to other particles(*152*). Due to significant enhancements of Raman signal strengths from the molecules in the vicinity of the surface plasmon resonance (SPR) of gold nanostructures, gold nanoparticles have been applied as surface enhanced Raman scattering (SERS)-based 'nanosensors' for local chemical probing of native biological molecules inside living cells(*153-160*). SERS provides structure-specific vibrational spectra of analytes with extremely high sensitivity resulting in many advantages over predominant fluorescence-based techniques. When compared to NIR-emitting quantum dots, *in vivo* mouse studies targeting tumor cells using SERS probes have resulted in two orders of magnitude brighter signal with broader multiplexing capabilities(*161, 162*).

4.2.2. Enhanced fluorescence applications

Enhanced fluorescence due to interactions between an excited fluorophore and plasmons of noble metal nanoparticles increase the quantum yield and photostability of the fluorophore(*85-88*). Silver nanoparticles conjugated to fluorophores have been employed in live cell studies where cell images were monitored via emission intensity and fluorophore lifetime(*163-165*). In these studies, emission signals from the metal probes could be isolated and counted on the cell images allowing for the quantification of target molecules on the cell surface at the single cell level. Other enhanced fluorescence applications have included their use in immunoassays where up to 66-

fold improvements in limits of detection have been reported when compared to their conventional counterparts(*166-171*).

4.2.3. Photothermal applications

Photothermal applications gold nanoparticles are currently undergoing clinical trials(*172-174*). Systemically administered of AuNPs have been shown to accumulate in tumors, where they have been irradiated with NIR laser light causing heating of the tumor tissue. Healthy tissue without associated nanoparticles is unaffected by the NIR laser light since at these wavelengths (600-1100 nm), there is lack of efficient endogenous absorbers allowing for high light penetration depth and decreased laser damage to non-target tissue(*96, 97*). On the hand, cancer cells in close proximity to AuNPs undergo hyperthermia and death, resulting in tumor remission(*172, 175, 176*).

4.2.4. Drug delivery

The interactions between photons and AuNP may allow for an additional therapeutic modality in AuNP-PHB granules in which drug release from drug-loaded granules could be triggered via local heating of AuNP on the PHB granule surface. Light-triggered release of substances from hydrogels has been previously described where light-induced structural changes such as contraction of the hydrogel causes the release of preloaded substances within the gel(*177*). The possibility for AuNP-mediated structural changes to PHB granules may allow for applying this unique means of delivery to the AuNP-PHB system.

Here we describe the aggregation-mediated plasmon-induced properties of AuNP-coated PHB granules. AuNP-coated PHB granules are shown to exhibit enhanced SERS and fluorescence as well as the capability of emitting heat from NIR illumination. These properties may allow for the use of these granules as theranostic

agents that may be followed via SERS and fluorescence and may deliver therapeutic payloads in the form of heat and as a PHB-mediated drug-delivery agent(*51, 52, 178, 179*).

4.3. Experimental

4.3.1. Raman spectroscopy

SERS analysis was performed using a Renishaw InVia microRaman system (Renishaw Plc, Gloucestershire, United Kingdom) equipped with a 785 nm solid-state laser. Three different compounds for Raman reporting including phenyl disulfide, benzyl disulfide, and 2-mercaptopyridine (all purchased from Sigma Aldrich, St. Louis, MO) were prepared at 1 mM in 50 mM sodium phosphate buffer, pH 7. To test the molecular specificity of the functionalized nanoparticles, as-synthesized gold particles coated with oleic-acid/oleylamine, functionalized gold particles coated with PL-PEG-COOH, and 5 nm citrate-stabilized gold particles (Product # G1402, Lot # 026K6112, Sigma Aldrich, St. Louis, MO) were used to prepare films of gold nanoparticle aggregates by drying 5 μL of particle solutions (optical density at 520 nm of 0.08) on a silicon substrate. Five microliters of each of the Raman reporter molecule solutions were then added to separate dried preparations of each of the nanoparticle samples and were then allowed to dry before scanning with the Raman spectrometer between 600 and 2000 cm^{-1} at 10% laser power with a 10 second exposure time. Raman data was processed by first subtracting the Raman spectra of the silicon background and then subtracting an end-weighted baseline using OriginPro 7.5 graphing software (OriginLab Corporation, Northampton, MA).

To measure the effect of PHB polymerization from AuNP-PHA synthase conjugates on SERS activity, a sample of AuNP-PHA synthase at an optical density at 520 nm of 0.08 was divided into two equal aliquots. 3HB-CoA was added to one

aliquot at a final concentration of 2.5 mM with the other aliquot diluted accordingly with water. The samples were allowed to stand at room temperature for two hours then a solution of phenyl disulfide in 50 mM sodium phosphate buffer, pH 7 was added to each sample at a final phenyl disulfide concentration of 1 mM. These solutions were then diluted 1/2, 1/5, and 1/10-fold and 5 μL of each of the dilutions were dried on a silicon substrate before scanning with the Raman spectrometer between 975 and 1125 cm^{-1} at 10% laser power with a 10 second exposure time. Five measurements were taken for each sample and the data was processed by first subtracting the Raman spectra of the silicon background and then subtracting an end-weighted baseline using OriginPro 7.5 graphing software (OriginLab Corporation, Northampton, MA).

4.3.2. Fluorescence measurements and analysis

The nanoparticle absorption spectra where acquired using a Shimadzu Mpc-3100 UV-VIS-NIR Scanning Spectrophotometer (Shimadzu Corporation, Kyoto, Japan). Fluorescence spectra were obtained using a Perkin Elmer LS-50B Luminescence Spectrometer (Perkin Elmer, Waltham, MA). To analyze AuNP-caused quenching of Nile red, samples with and without AuNP-PHA synthase and containing 1 μg/mL of Nile red and 0.1 mg/mL of PL-PEG-COOH were compared. Since Nile red only exhibits appreciable fluorescence when in hydrophobic environments, PL-PEG-COOH was included in these samples in order to measure Nile red fluorescence in samples prior to the addition of AuNP-PHA synthase. PL-PEG-COOH forms micelles in the aqueous solution and upon the addition of AuNP-PHA synthase (final OD_{520} = 0.025), Nile red equilibrates its distribution between PL-PEG-COOH micelles and the hydrophobic layer in AuNP-PHA synthase. For both absorption and fluoresce measurements, samples were placed in 3 mm path length special optical glass fluorometer cells (Starna Cells, Inc. Atascadero, CA).

For enhanced fluorescence and photobleaching experiments, AuNP-coated PHB granules were prepared by mixing AuNP-PHA synthase (0.1 mg/mL based on protein concentration) with 3HB-CoA (5 mM) in 50 mM phosphate buffer, pH 7 and allowed to incubate at room temperature for 2 hrs. Uncoated PHB granules were prepared by mixing PHA synthase (0.1 mg/mL) with 3HB-CoA (5 mM) in 50 mM phosphate buffer, pH 7 and allowed to incubate at room temperature for 2 hrs. Samples were then stained with Nile red at a 1 μg/mL working concentration. Fluorescence measurements were conducted with an inverted fluorescence microscope (Model IX51, Olympus Corporation, Tokyo, Japan), equipped with a 560 nm/645 nm excitation/emission filter cube (Chroma Technology Inc, Bellows Falls, VT), a 100X Olympus objective lens, and an Olympus DP70 CCD camera. Images were captured at 1 second intervals for 30 sec using Image Pro Plus (Media Cybernetics, Inc, Bethesda, MD). Image analysis was performed with Image Pro Plus by first setting a fixed threshold across all images based on the software's edge detection algorithm that delineated individual fluorescent spots, then analyzing the diameter and intensity of individual fluorescent spots with a roundness value of 1, defined as the following: roundness = perimeter^2 / (4 π area); a roundness value of 1 indicates a perfect circle and as the value approaches infinity, it indicates the shape is a line segment. This roundness value was chosen in order to only analyze individual PHB granules and to avoid aggregates. 246 granules were analyzed for each sample.

4.3.3. Heating

Heating experiments were conducted using a 1.2 watt, 808 nm continuous wave diode laser (SDL-2360-C, JDL Uniphase, Milpitas, CA) culminated to 0.5 mm diameter with temperature measurements conducted with a fiber optic temperature sensor (Reflex Signal Conditioner, Neoptix, Québec, Canada). A sample of AuNP-PHA synthase at an optical density at 520 nm of 0.9 was divided into two equal

aliquots. 3HB-CoA was added to one aliquot at a final concentration of 2.5 mM with the other aliquot diluted accordingly with water. The samples were allowed to stand at room temperature for two hours and thirty microliters of AuNP-PHA synthase samples prior and after polymerization were placed inside PCR tubes with the temperature probe positioned away from incident laser light. Samples were illuminated at 3 W/mm^2 and their temperature was monitored over a period of 2 min. Measurements were conducted in triplicate and referenced to measurements on 50 mM sodium phosphate buffer, pH 7.

4.3.4. Laser-triggered AuNP-PHB-based drug delivery

Doxorubicin (Dox) (Sigma Aldrich, St. Louis, MO) was loaded into AuNP-PHB granules by mixing AuNP-PHA synthase (0.1 mg/mL based on protein concentration) with Dox (5 μg/mL) in 50 mM phosphate buffer, pH 7.5, then subsequently adding 3HB-CoA (5 mM) and allowing the sample to incubate at room temperature for 2 hrs. Control samples included Dox loaded PHB granules, prepared as described above but with PHA synthase (0.1 mg/mL) instead of AuNP-PHA synthase, and samples containing AuNP-PHA synthase and Dox but no 3HB-CoA (i.e. prior to polymerization of PHB). The fluorescence intensity of the samples was then measured using a fluorometer (Perkin Elmer LS 50 B scanning fluorometer, Perkin Elmer, Waltham, MA) prior and after laser irradiation at 3 W/mm^2 for 2 min (1.2 watt, 808 nm continuous-wave diode laser culminated to a 0.5 mm diameter). Subsequent fluorescence measurements were again preformed 10 min and 12 hrs after irradiation. Samples were prepared in triplicate.

4.4. Results and discussion

4.4.1. Selectivity of AuNP-PL-PEG-COOH towards non-polar SERS reporters

Of the two non-polar molecules (phenyl disulfide, phenyl disulfide) and one polar molecule (2-mercaptopyridine) examined as possible Raman reporters, phenyl disulfide and benzyl disulfide but not for 2-mercaptopyridine exhibited SERS with AuNP-PL-PEG-COOH particles (Figure 4.1). This specificity towards hydrophobic compounds is thought to result from the hydrophobic layer coating at the junction between oleic acid/oleylamine and phospholipid tails of PL-PEG-COOH that prevented access for polar compounds to the gold particle surface. To test this, each of the Raman reporter molecules were added to dried nanoparticle suspensions of as-synthesized gold particles coated with oleic-acid/oleylamine, functionalized gold particles coated with PL-PEG-COOH, and commercially available 5 nm citrate-stabilized gold particles. SERS spectra were observed from all of the Raman reporter molecules on as-synthesized oleic-acid/oleylamine and commercially available 5 nm citrate-stabilized gold particles while SERS spectra from PL-PEG-COOH particles was only observed from the hydrophobic benzyl disulfide and phenyl disulfide (Figure 3.1, data shown for PL-PEG-COOH and citrate-stabilized particles with phenyl disulfide). Given this data, it seems that all of the compounds are able to displace citrate and bind to the gold particle surface – thiols and disulfides readily bind to gold to give stable monolayers(*180*). Similarly, all of the compounds have access to the as-synthesized oleic acid/oleylamine gold particles, yet only the hydrophobic compounds are able to penetrate the oleic acid/oleylamine-phospholipid layer surrounding the PL-PEG-COOH functionalized particles.

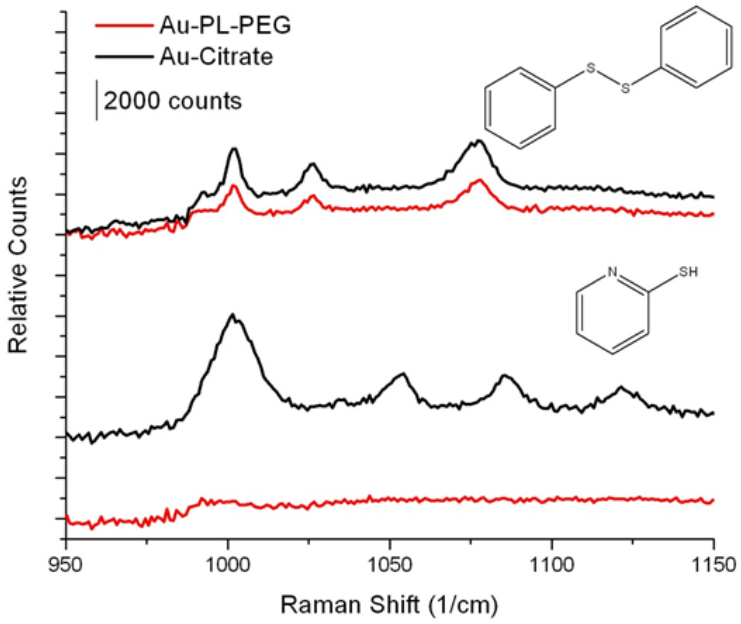

Figure 4.1: Selectivity of PEGylated phospholipid-coated AuNP for nonpolar Raman reporters

Phenyl disulfide and 2-mercaptopyridine were mixed with AuNP-PL-PEG-COOH and citrate coated AuNP in order to determine the molecular specificity of the AuNP to these Raman reporters based on the different nanoparticle coatings. AuNP-PL-PEG-COOH particles (red trace) exhibited SERS for non-polar molecules such as phenyl disulfide (top) but not for polar molecules such as 2-mercaptopyridine (bottom). Citrate-stabilized gold particles (black trace) instead exhibited SERS activity for both polar and non-polar molecules. Both polar and non-polar compounds are able to displace citrate and bind to the gold particle surface via thiol and disulfide groups in these compounds, yet only the hydrophobic compounds are able to penetrate the oleic acid/oleylamine-phospholipid layer surrounding the PL-PEG-COOH functionalized particles.

4.4.2. Surface Enhanced Raman Scattering

AuNP-coated PHB granules exhibited enhanced SERS over AuNP-PHA synthase particles. When comparing the 1000 cm^{-1} (benzene ring vibration(*181*)) Raman band intensity of phenyl disulfide on AuNP-PHA synthase and AuNP-coated PHB granules, at the lowest dilution (based on the OD_{520} of each sample) at which AuNP-PHA synthase produced an observable signal over background, signal derived from AuNP-coated PHB granules exhibited an average Raman intensity of 3983 counts over background signal (Figure 4.2). The average relative enhancement factor ranged from 3 ± 0.2 to 11 ± 0.81 across the dilutions tested with the highest enhancement observed at the lowest dilution where AuNP-PHA synthase produced an observable signal over baseline (Figure 4.3).

It is thought that the organization of gold nanoparticles around PHB granules gives rise to the observed SERS enhancement effects. AuNP-PHB samples contain both AuNP-coated PHB as well as AuNP not associated with PHB granules and in the Raman measurements, both AuNP-PHB and AuNP-PHA synthase were dried resulting in both samples containing aggregated AuNP due to drying. Thus, the observed enhancement in SERS from AuNP-coated PHB was in reference to that of SERS from aggregated AuNP-PHA synthase. This observation indicates that enhancement in SERS is mediated by PHB polymerization that results in an enhancement factor over that of AuNP aggregation caused by the drying of AuNP-PHA synthase samples. The interparticle interactions on the PHB granule surface are likely to produce electromagnetic 'hot spots' and this is thought to provide the dominant form of SERS enhancement(*79, 80*). Furthermore, the shell structure that is formed by the nanoparticle coating may also contribute to the observed enhancement as similar metallic shell structures have been shown to increase both the effective

volume in which molecules are affected by the enhanced electric field and the Raman gain averaged over this volume(*182*).

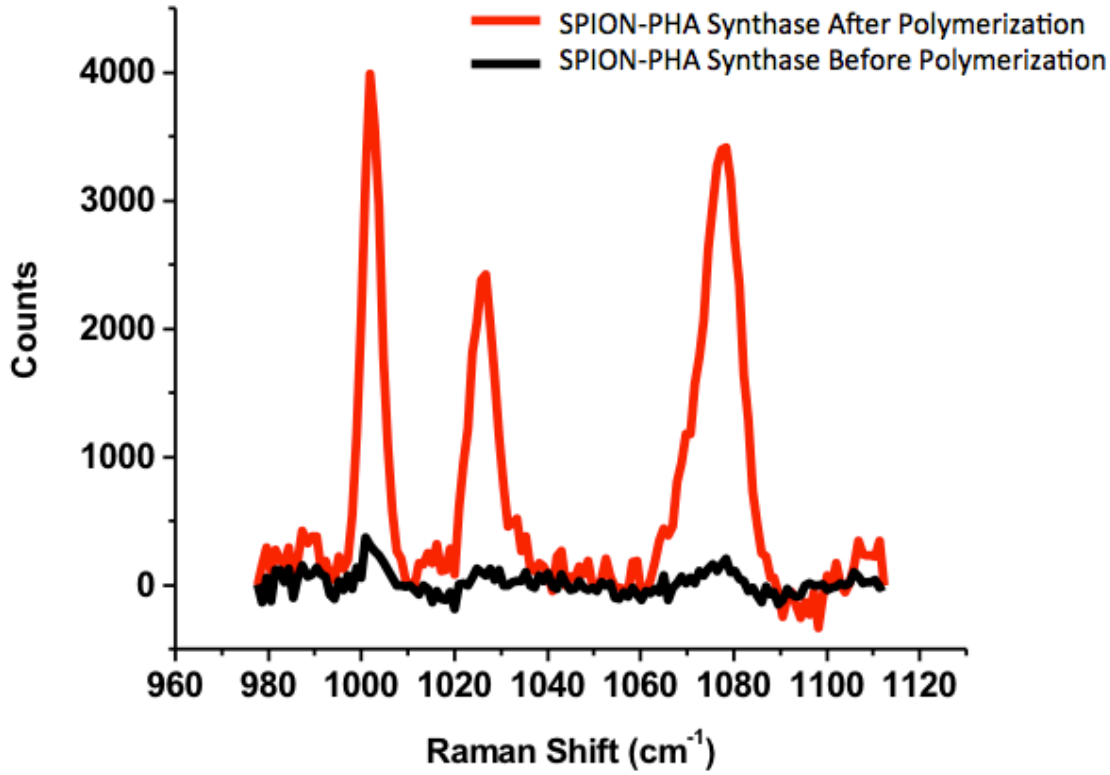

Figure 4.2: Enhanced SERS from AuNP-PHA Synthase before vs. after polymerization

Material containing AuNP-coated PHB granules exhibited enhanced SERS when compared to SERS derived from AuNP-PHA synthase conjugates. The Raman spectra of phenyl disulfide added to AuNP-PHA synthase and AuNP-coated PHB granules was compared from samples diluted such that those containing AuNP-PHA synthase produced signal close to background. Under these conditions, an equal amount of AuNP from samples containing AuNP-coated PHB granules exhibited an average Raman intensity of 3983 counts over background signal.

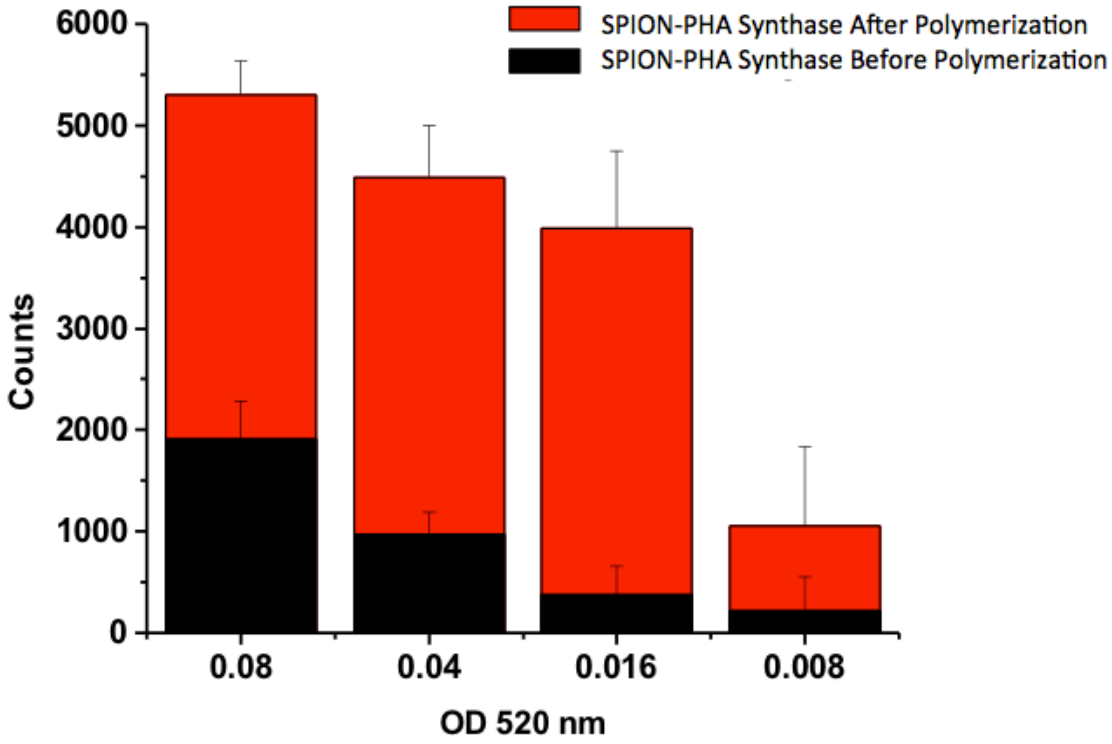

Figure 4.3: Raman limit of detection of phenyl disulfide on AuNP-PHA synthase before vs. after polymerization

Based on measurements as depicted in Figure 4.2, when comparing the 1000 cm^{-1} (benzene ring vibration(181)) Raman band intensity of phenyl disulfide added to samples containing varying dilutions of AuNP-PHA synthase and AuNP-coated PHB granules based on the OD_{520} of the samples, the average relative enhancement factor for AuNP-coated PHB ranged from 3 ± 0.2 to 11 ± 0.81 across the dilutions tested with the highest enhancement observed at the dilution when AuNP-PHA synthase reached the limit of detection.

4.4.3. Fluorescence Enhancement

When comparing AuNP-coated and uncoated Nile red-stained PHB granules, coated granules exhibited increased fluorescence intensity per unit area of the imaged granules with an average enhancement factor of 6.01 ± 1.47. A concern during these measurements was that a larger granule size would contribute to the appearance of fluorescence enhancement simply due to a larger Nile red loading capacity. In fact, plotting the fluorescent spot intensity vs. size of fluorescently imaged granules reveals a linear increase in fluorescence intensity with increasing unit area. Nevertheless, enhancement in fluorescence intensity comparing nanoparticle-coated and uncoated granules is evident (Figure 4.4).

To examine the photobleaching characteristics of coated and uncoated Nile red granules, the same individual fluorescent spots analyzed for fluorescence enhancement were tracked and analyzed for fluorescence intensity per unit area in subsequent image sequences taken during continuous illumination by the microscope excitation source. Indeed, an increase in photo stability of Nile red was observed (Figure 4.5) with a 1.3 ± 0.21-fold decrease in the fluorescence intensity decay rate for Au-coated PHB (0.16 ± 0.030 s^{-1}) compared to PHB alone (0.20 ± 0.015 s^{-1}). In addition, based on fitting of the photo bleaching data, once bleaching has reached steady-state, AuNP-coated PHB granules would remain 4.73 ± 1.11-times more intense than PHB granules alone.

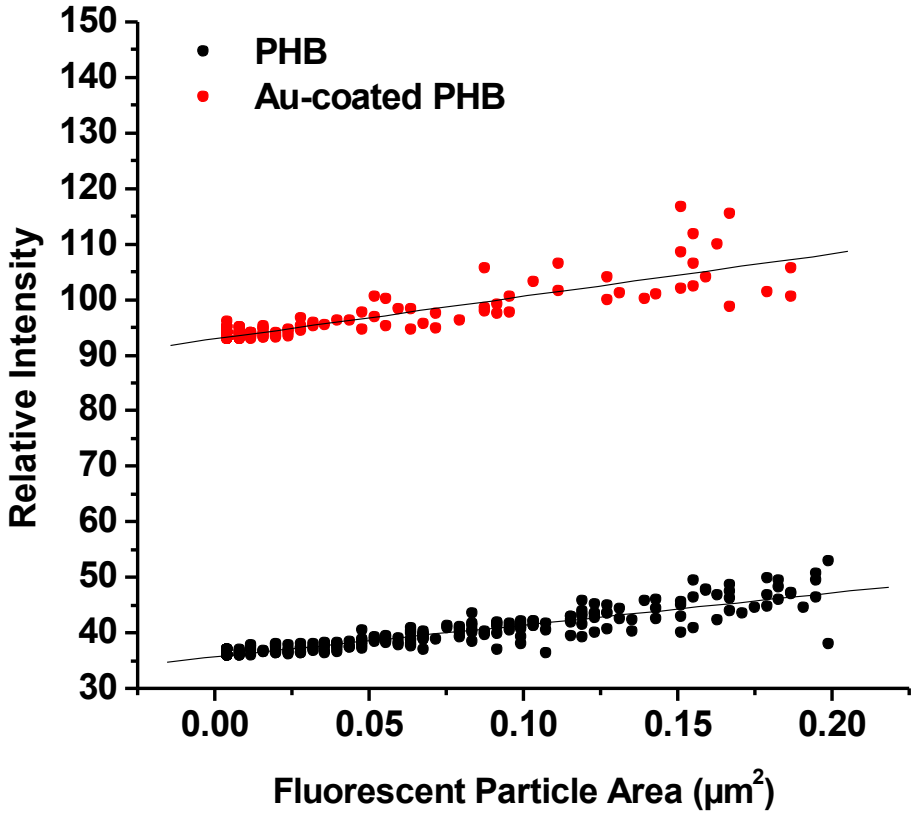

Figure 4.4: Enhanced fluorescence from stained AuNP-coated PHB granules

The fluorescence intensity of Nile red-stained PHB granules (black) and Nile red-stained AuNP-coated PHB granules (red) was plotted vs. granule size ad determined from fluorescence microscopy. A linear increase in fluorescence intensity with increasing granule unit area was observed for both samples in addition to a fluorescence intensity per unit area enhancement factor of 6.01 ± 1.47 when comparing AuNP-coated and uncoated Nile red-stained PHB granules.

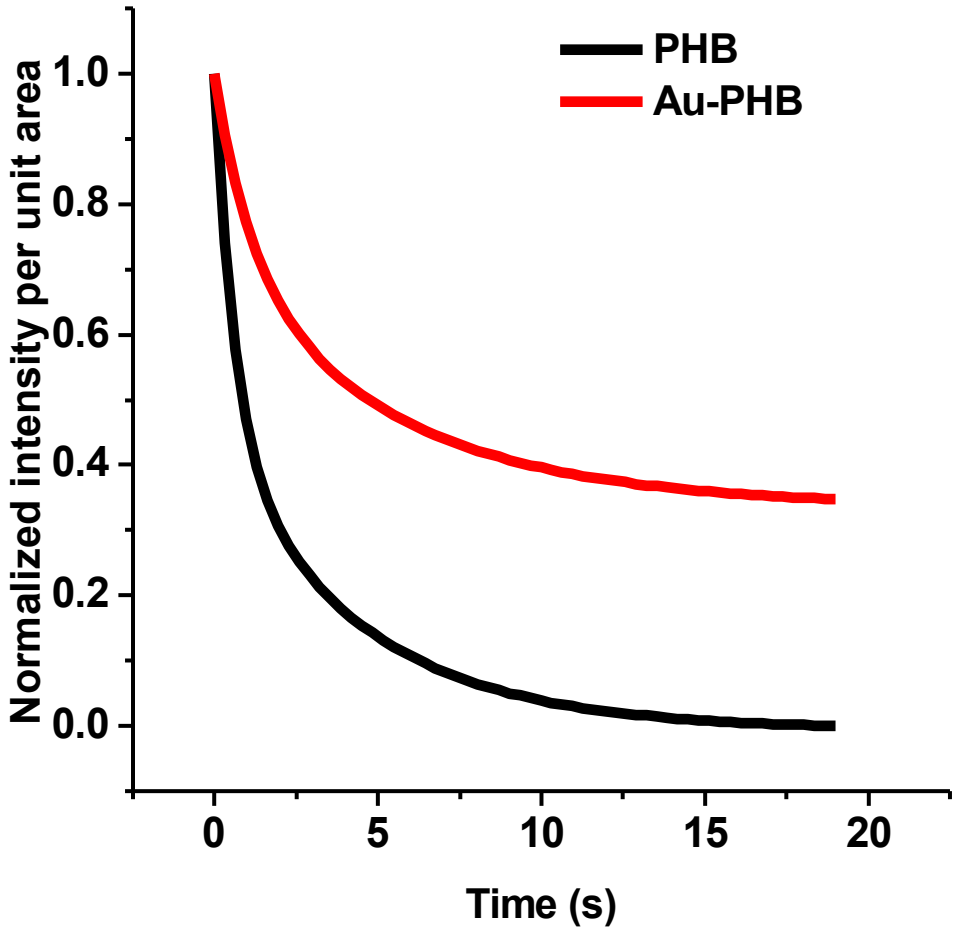

Figure 4.5: Increased photo stability of stained AuNP-coated PHB granules

The individual fluorescent PHB granules (black) and AuNP-coated PHB granules (red) were analyzed for fluorescence intensity through image sequences taken during continuous illumination by the fluorescence microscope. The plot shows second order exponential decay fits ($R^2 > 0.99$) of the average intensity per unit area vs. time for each sample. When comparing the rate constants of the fitted data, a 1.3 ± 0.21-fold decrease in the fluorescence intensity decay rate was observed for Au-coated PHB (0.16 ± 0.030 s^{-1}) compared to PHB alone (0.20 ± 0.015 s^{-1}). In addition, AuNP-coated PHB granules remained 4.73 ± 1.11-times more intense than PHB granules alone at steady state.

The AuNP particle coating and their arrangement on the PHB granule surface reveal the likely source of fluorescent enhancement. Figure 4.6 depicts the possible AuNP-coated PHB granule geometry with regard to SERS and enhanced fluorescence. In the diagram, yellow stars represent Nile red that is shown to be incorporated in the hydrophobic PHB core as well as the hydrophobic layer comprised of the interface between the phospholipid tails of PL-PEG and oleic acid/oleylamine surrounding the AuNP. The blue stars represent a Raman reporter molecule that similarly can become incorporated in these hydrophobic regions and which can also bind to the gold nanoparticle surface via its disulfide group(*180*). When a fluorophore is localized to metal particles or surfaces at less than ~5 nm, its emission is quenched by energy transfer to the metal(*82*). However, at further distances from the metal (between 5 and 70 nm), increases in fluorescence can be observed(*82-85*). While Nile red stains the PHB granule, it may also stain the hydrophobic layer around the AuNPs formed by the oleic acid/oleylamine and phospholipid tails surrounding the particles. This layer, however, is less than 5 nm thick given our DLS particle size data and judging by the molecular dimensions of oleic acid, oleylamine, and the phospholipid (Figure 2.5). We have observed that Nile red within this layer is quenched by the gold nanoparticles (Figure 4.7)(*82*). Quenching is expected due to the proximity of Nile red to the gold nanoparticle surface and since there is appreciable overlap between the extinction of the gold particles and the Nile red fluorescence spectrum(*183*). Conversely, given DLS measurements and the molecular dimensions of the nanoparticle coating (Figure 2.7), Nile red absorbed within the PHB granule is at a distance of at most ~25 nm to the gold particle (Figure 4.6). Fluorescence enhancement has been observed between 5 nm and 70 nm away from nanostructured metallic surfaces, thus due to the configuration of AuNP-coated PHB granules, Nile red within the PHB granule is within a distance where enhanced fluorescence is possible(*183*).

Since Nile red was always included in excess in these experiments, another possibility that could explain the observed phenomenon may be instead that stained native PHB granules actually exhibit less than optimal fluorescence due to auto-quenching of excess Nile red or high labeling density and that a fundamental difference in PHB core structure of AuNP-coated PHB could have resulted the incorporation of relatively less Nile red or lower labeling density in these structures leading to less auto-quenching. Nevertheless, this scenario does not take into account the observed decrease in photobleaching in samples containing AuNP-coated PHB granules since a less degree of photobleaching would be expected from quenched molecules.

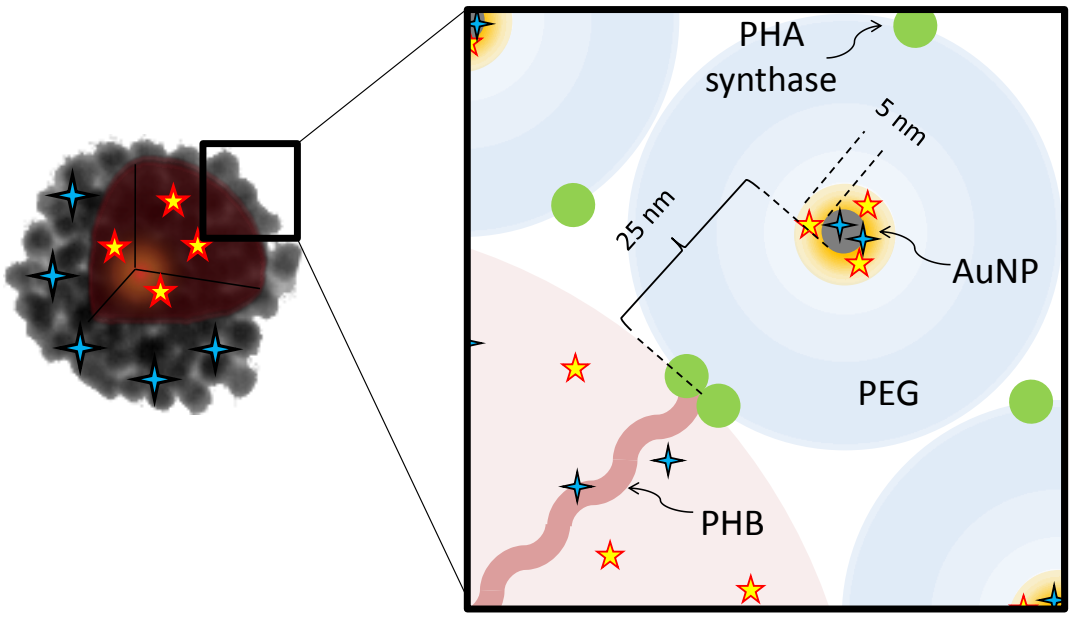

Figure 4.6: AuNP-coated PHB granule structure

The figure depicts the possible AuNP-coated PHB granule geometry with regard to SERS and enhanced fluorescence. Yellow stars represent Nile red that is shown incorporated in the hydrophobic PHB core as well as the hydrophobic layer comprised of the interface between the phospholipid tails of PL-PEG and oleic acid/oleylamine surrounding the AuNP. The blue stars represent a Raman reporter molecule that similarly can become incorporated in these hydrophobic regions and which can also bind to the gold nanoparticle surface via its disulfide group.

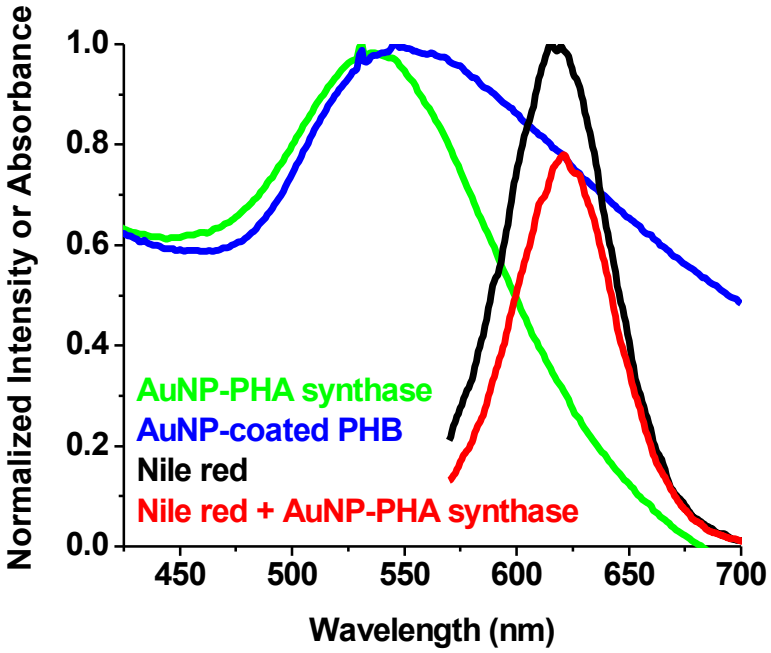

Figure 4.7: AuNP-PHA synthase and AuNP-PHB absorption spectra and Nile red quenching

The figure shows absorption spectra of AuNP-PHA synthase and AuNP-coated PHB superimposed on the emission spectra of Nile red fluorescence and quenched Nile red fluorescence due to the addition of AuNP-PHA synthase. Due to the aggregation of the gold nanoparticles on the PHB granule surface, broadening in the plasmon resonance of the AuNP-coated PHB granules over AuNP-PHA synthase was observed. When AuNP-PHA synthase conjugates are added to solutions containing PL-PEG-COOH and Nile red, quenching is observed. Quenching is likely due to Nile red staining of the hydrophobic region formed by the interface between oleic acid/oleylamine and phospholipid tails surrounding gold nanoparticles; at this location, Nile red is within 5 nm of the gold nanoparticle surface where its emission may be quenched by the particle.

Furthermore, two phenomena can contribute to fluorescent enhancement including surface enhanced fluorescence (SEF) in which the metal particles concentrate the local excitation intensity and metal enhanced fluorescence (MEF) in which the electric field felt by a fluorophore is affected by interaction of the fluorophore oscillating dipole with the metal surface(*85-88*). In MEF, an increase in the radiative rate is expected, resulting in an increased intensity and decrease in photobleaching since the fluorophore spends less time in the excited state for each excitation. Our observation of increased photo stability points to the possibility that the nanoparticle coating causes a decrease in the radiative decay rate of the Nile red, indicating that MEF contributes to fluorescence enhancement in the system.

4.4.4. ***NIR Heating***

NIR-induced heating of AuNP-PHA synthase and AuNP-coated PHB granules resulted in a linear temperature increase for each sample with all measurements exhibiting an R^2 value greater than 0.997 for linear fits of the data. The 808 nm NIR laser illumination of AuNP-coated PHB granules resulted in a 3.9 ± 0.69 increase in the heating rate when compared to AuNP-PHA synthase prior to polymerization (Figure 4.8), as determined from the slopes of the fitted temperature vs. time plots. Due to the aggregation of the gold nanoparticles on the PHB granule surface, broadening in the plasmon resonance of the AuNP-coated PHB granules over AuNP-PHA synthase was observed (Figure 4.7) and the increase in heating rate is likely due to increased overlap between the 808 nm laser source and the plasmon of the AuNP-coated PHB granules(*184, 185*).

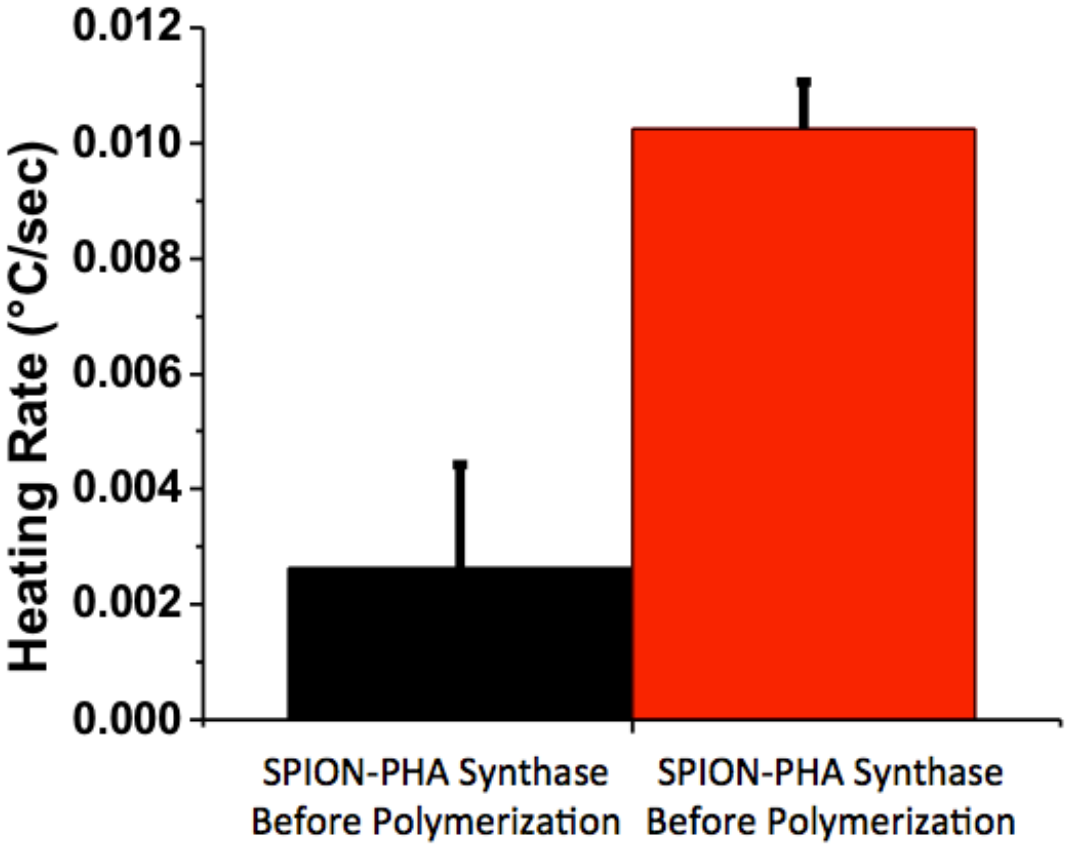

Figure 4.8: Enhanced NIR heating of AuNP-coated PHB granules

Samples of AuNP-PHA synthase conjugates and AuNP-coated PHB granules each containing equivalent amounts of AuNP based on their optical density at 520 nm were irradiated with an 808 nm NIR laser and while monitoring the temperature of each sample. The temperature of each sample increased linearly over irradiation time and the slope of linear fits of the data was used to determine the heating rate for each sample. The figure shows the average heating rate and standard deviation of AuNP-PHA synthase vs. AuNP-coated PHB upon NIR illumination. Irradiation of AuNP-coated PHB granules with 808 nm NIR laser illumination resulted in a 3.9 ± 0.69 increase in the heating rate when compared to irradiation of AuNP-PHA synthase prior to polymerization.

4.4.5. Laser-triggered AuNP-PHB-based drug delivery

Upon loading of Dox to AuNP-coated PHB, the fluorescence intensity of Dox increased 5.03 ± 0.248 units over background (Figure 4.9). This increase is consistent with the observed AuNP-induced fluorescence enhancement of Nile red loaded PHB granules. After NIR irradiation, the fluorescence intensity of the sample then dropped to an average of 1.99 ± 0.433 units over background levels and the fluorescence intensity did not reappear after subsequent measurements of the same sample 10 minutes and 12 hours after irradiation. Fluorescence microscopy of Dox-loaded AuNP-coated PHB samples before and after irradiation show a decrease in fluorescent granules after irradiation (Figure 4.10). Control experiments confirmed that an increase in fluorescence intensity is only observed upon the addition of Dox to AuNP-coated PHB and not AuNP-PHA synthase indicating that enhancement is caused by Dox loading into coated PHB and not simply due to AuNP alone. Further control experiments showed that laser-induced loss of fluorescence intensity was only observed in Dox-loaded AuNP-PHB samples and not for Dox-loaded PHB alone or AuNP-PHA synthase samples including Dox.

It is thought that the loss in fluorescence of Dox-loaded AuNP-PHB granules is due to destruction of the PHB granule due to local heating of its AuNP coating upon laser irradiation. The decrease in fluorescent granules after laser irradiation observed through fluorescence microscopy indicates a loss in granule structure. This is supported by the observation that the loss in fluorescence was not regained after prolonged incubation of the sample. In these samples, the Dox concentration was in excess with respect to granule loading capacity and the loss in fluorescence intensity would have been expected to be regained in the case that Dox was released while the granule remained intact.

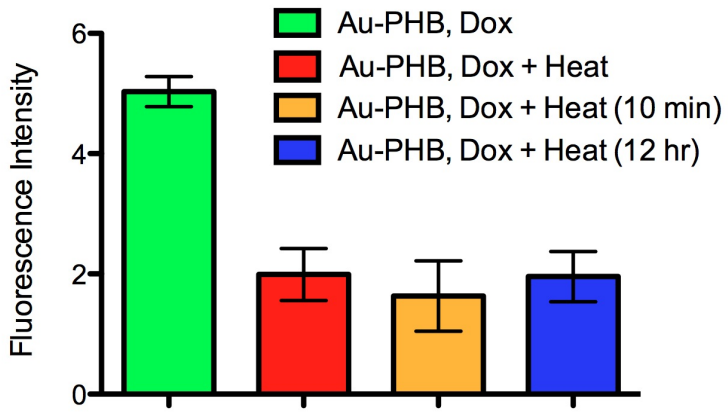

Figure 4.9: NIR illumination-triggered Dox release from AuNP-coated PHB granules

Dox was added to samples of AuNP-PHA synthase conjugates and AuNP-coated PHB. The figure shows the Dox fluorescence intensity in various samples relative to background fluorescence exhibited from samples containing Dox and AuNP-PHA synthase. Samples containing AuNP-coated PHB exhibited fluorescence at 5.0 ± 0.25 units over background due to the loading of Dox into PHB granules and as a result of enhanced fluorescence via AuNP-coating on the granules. Samples where then irradiated with an 808 nm NIR laser and their fluorescence was monitored. Measurements were taken prior to NIR laser illumination (green) and immediately after NIR laser illumination (red) as well as 10 min (orange) and 12 hr (blue) after laser irradiation. After NIR irradiation, the fluorescence intensity of the samples dropped to an average of ~2 units over background and the fluorescence intensity did not reappear after subsequent measurements of the same sample 10 minutes and 12 hours after irradiation. The loss of fluorescence intensity after NIR laser irradiation may be due to the destruction of AuNP-coated PHB granules.

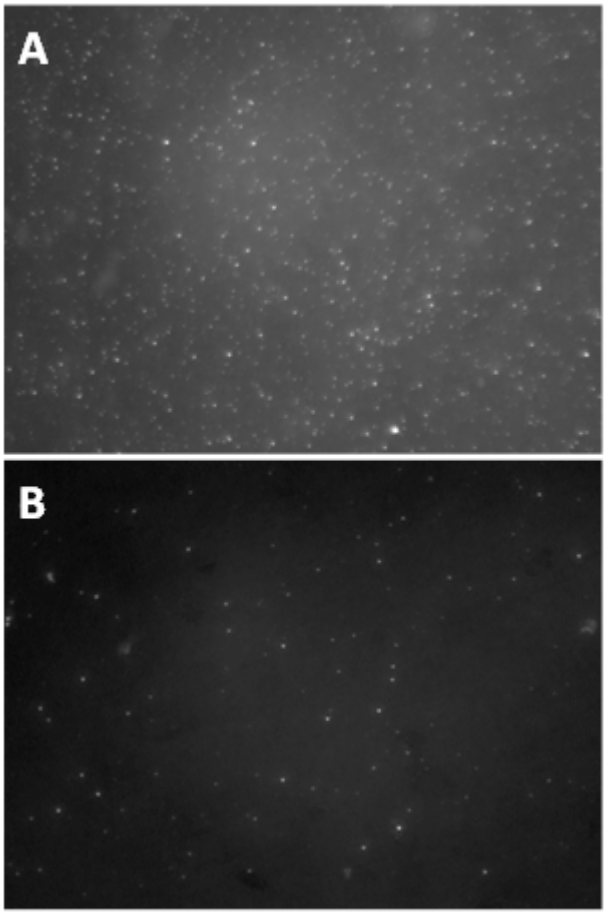

Figure 4.10: Fluorescence image of Dox-loaded AuNP-coated PHB granules before and after NIR laser illumination

Dox-loaded AuNP-PHB granules were imaged at 100x magnification via fluorescence microscopy before (A) and after (B) NIR laser illumination revealing a decrease in fluorescent granules after irradiation possibly due to the destruction of AuNP-coated PHB granules.

4.5. Conclusions

When compared to AuNP-PHA synthase conjugates, AuNP-coated PHB granules exhibited enhancement in SERS properties as well as increased heating rate upon NIR illumination. Nile red-stained AuNP-coated PHB granules also exhibited enhanced fluorescence and decreased photobleaching when compared to uncoated PHB granules. NIR irradiation of Dox-loaded PHB granules resulted in loss of Dox fluorescence due to destruction of PHB granules providing a potential means of triggered drug release from AuNP-PHB granules. Given the advances in utilizing PHB as a matrix for drug-delivery, our AuNP-PHA synthase conjugates may serve as multimodal imaging/drug delivery vehicles in which gold nanoparticle-coated PHB granules carrying a drug and/or fluorophore may be tracked via fluorescence or SERS and may be heated via NIR illumination(*52, 178, 179, 186, 187*).

Multimodal particles exhibiting various imaging and therapeutic characteristics are emerging as promising platforms in biomedical applications. In particular, the applicability of dual SERS/MEF particles in multiplexed immunoassays was recently shown(*188*). Furthermore, several studies have demonstrated the utility of gold nanoparticle-based SERS imaging *in vivo*, highlighting the advantages of high signal strength as well as the use of these materials as dual imaging and photothermal agents(*162, 186, 187, 189-191*). In comparison to previously described dual SERS/MEF particles that were constructed via layer-by-layer deposition of polyelectrolyte coatings on silica cores, AuNP-coated PHB offer a facile self-assembly approach for particle formation(*188*). Furthermore, the PEGylated AuNP coating around PHB granules may facilitate their application *in vivo* when compared to currently employed gold-nanoparticle based theranostic agents among which 100 nm gold nanoshells with silica cores are the best studied and are currently undergoing

clinical trials(*172-174, 186*). Upon their systemic administration, these nanoshells are cleared from the blood stream within 24 hours and accumulate in the liver and spleen where they are retained by the body for months(*186*). The retention of the nanoshells is likely due to their opsonization by serum proteins and subsequent uptake by the RES where they are retained within Kupffer cells(*146*). The Kupffer cells eventually can begin to eliminate the nanoparticles via cell turnover – a process that may take up to six months resulting long-term nanoparticle retention in the body(*192*). In contrast to these nanoshells, AuNP-coated PHB granules may result in an alternate clearance pathway from their potential for decreased opsonization due to the densely-packed PEG coating on the AuNP that cover the PHB granule(*144, 145*). As a result, AuNP-coated PHB would instead be cleared via hepatocytes that excrete nanoparticles into the bile resulting in the elimination of nanoparticles from the body in weeks rather than months(*146*).

Chapter 5 – Conclusions and future directions

5.1. Future studies

Future studies should move towards demonstrating diagnostic and therapeutic applications of AuNP- and SPION-coated PHB including the investigation of the biodistribution, cytotoxicity and biocompatibility of the materials. Due to the biocompatible nature of each of the major components that make up our nanoparticle-coated granules (AuNP, SPION, PEG, and PHB), the nanoparticle-coated granules are expected to exhibit low toxicity in cell culture and *in vivo* applications. Furthermore, the densely-packed nature of PEG coating the nanoparticles that cover the PHB granules may improve the biodistribution and clearance of nanoparticle-coated granules when compared to PEGylated particles of similar size to the PHB granules.

Some of the unique advantages of PHB-based nanoparticles for biomedical applications are derived from the biodegradability and biocompatibility of the biopolymer in combination with their biosynthetic means of production. PHB implants have been shown to degrade over periods greater than 1 year(*193-195*). When prolonged stability is desired, this offers a potential advantage over other available biodegradable polymers such as poly(lactic acid) or poly(glycolic acid) which degrade *in vivo* over a period of 1-2 months(*27*). Nevertheless, in cases where prolonged stability is not desired, the degradation rate of the polymer can be increased via modification of the chemical composition of PHB through the selection of monomers that render the polymer more susceptible to hydrolysis or enzymatic attack. Monomers that have been used for this purpose include glycolic acid, lactic acid, and 2-hydroxyethoxy acetic acid which modulate the reactivity of the ester linkage(*195*). In this manner, the *in vivo* degradation of PHB-based materials has been reduced to months(*195*). In addition, biosynthetic production of PHB granules has been highlighted as a means of avoiding the use of organic solvents in particle

production(*27, 63*), nevertheless, since PHA synthase is derived from bacterial sources, the need for pyrogen removal is an unexplored concern(*15*).

5.2. Conclusions

PHB is proving to be a promising class of biodegradable and biocompatible polymer for biomedical applications. The recent recognition of PHB granules as nanoparticles(*15, 196*) that can be functionalized to suit various applications is resulting in exciting diagnostic and therapeutic studies that employ PHB granules.

The studies in this dissertation describe a novel means of producing nanoparticle-coated PHB granules that expands the capabilities of functionalized PHB granules through harnessing versatile properties of inorganic nanoparticles. The properties of AuNP- and SPION-coated PHB granules outlined in Chapters 3 and 4 show that the materials are promising candidates for use in various biomedical applications. In general, both of these materials may be suitable as multifunctional theranostic agents as summarized in Figures 5.1 and 5.2. SPION-coated PHB granules exhibit enhanced MRI contrast and can be loaded with fluorescent dyes and/or drugs. These particles are thus multifunctional theranostic agents with imaging (MRI, fluorescence) and therapeutic (drug encapsulation) capabilities. Upon laser illumination, AuNP-coated PHB granules can exhibit enhanced SERS and fluorescence in addition to heating and drug release. These particles are thus multifunctional theranostic agents with imaging (SERS, fluorescence) and therapeutic (heat, triggered drug release) capabilities.

In conclusion, the work outlined in this thesis offers a novel means of PHB granule decoration with inorganic nanoparticles expanding the capabilities of functionalized PHB granules through harnessing versatile properties of provided by inorganic nanoparticles.

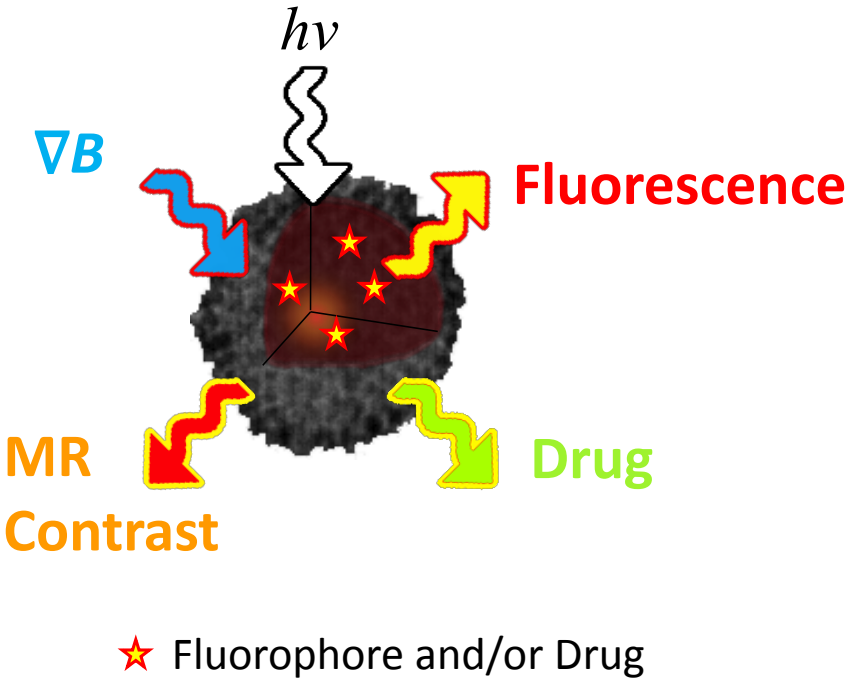

Figure 5.1: Multifunctional properties of SPION-coated PHB granules

SPION-coated PHB granules exhibit enhanced MRI contrast (MRI is denoted by ∇B) and can be loaded with fluorescent dyes and/or drugs. These particles are thus multifunctional theranostic agents with imaging (MRI, fluorescence) and therapeutic (drug encapsulation) capabilities.

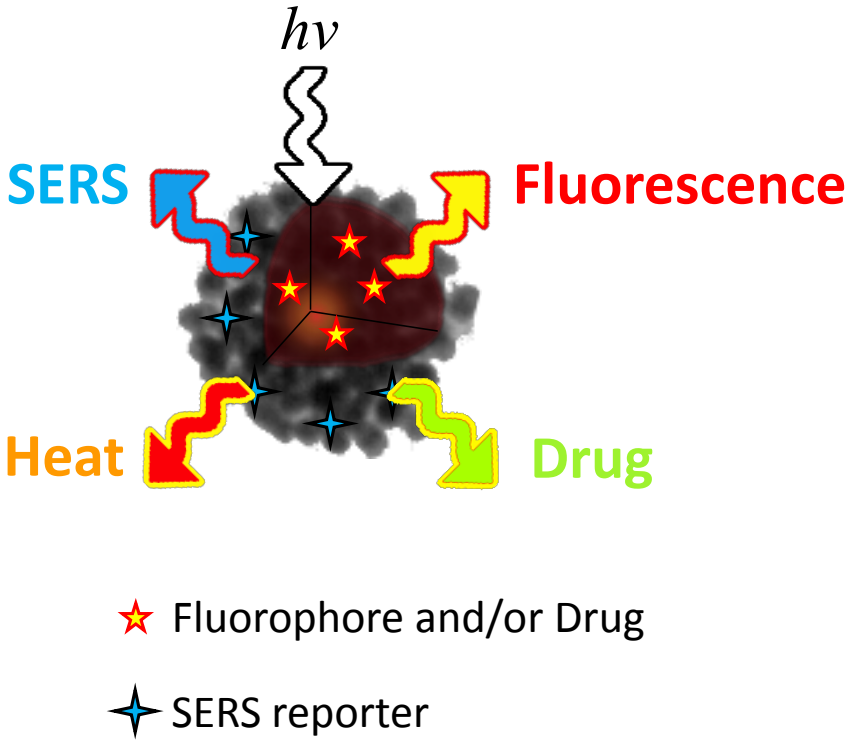

Figure 5.2: Multifunctional properties of AuNP-coated PHB granules

Upon laser illumination, AuNP-coated PHB granules can exhibit enhanced SERS and fluorescence in addition to heating and drug release. These particles are thus multifunctional theranostic agents with imaging (SERS, fluorescence) and therapeutic (heat, triggered drug release) capabilities.

References

1. H. G. Brandl, R.A.; Lenz, R.W.; Fuller, R.C., Pseudomonas oleovorans as a Source of Poly(β-Hydroxyalkanoates) for Potential Applications as Biodegradable Polyesters. *Appl. Environ. Microbiol.* **54**, 1977 (1988).
2. J. Han, Q. Lu, L. Zhou, J. Zhou, H. Xiang, Molecular Characterization of the phaECHm Genes, Required for Biosynthesis of Poly(3-Hydroxybutyrate) in the Extremely Halophilic Archaeon Haloarcula marismortui. *Appl. Environ. Microbiol.* **73**, 6058 (October 1, 2007, 2007).
3. F. F. Hezayen, B. H. A. Rehm, R. Eberhardt, A. Steinbüchel, Polymer production by two newly isolated extremely halophilic archaea: application of a novel corrosion-resistant bioreactor. *Appl. Microbiol. Biotechnol.* **54**, 319 (2000).
4. F. F. S. Hezayen, A.; Rehm, B.H.A., Biochemical and enzymological properties of the polyhydroxybutyrate synthase from the extremely halophilic archaeon strain 56. *Arch. Biochem. Biophys.* **403**, 284 (2002).
5. F. F. T. Hezayen, B.J.; Steinbüchel, A.; Rehm, B.H.A. , Characterization of a novel halophilic archaeon Halobiforma haloterrestre gen. nov., sp. nov., and transfer of Natronobacterium nitratireducens to Halobiforma nitratireducens comb. nov. *Int. J. Syst. Evol. Bacteriol.* **52**, 2271 (2002).
6. Q. Lu, J. Han, L. Zhou, J. Zhou, H. Xiang, Genetic and Biochemical Characterization of the Poly(3-Hydroxybutyrate-co-3-Hydroxyvalerate) Synthase in Haloferax mediterranei. *J. Bacteriol.* **190**, 4173 (June 15, 2008, 2008).

7. N. Hoffmann, B. H. A. Rehm, Nitrogen-dependent regulation of medium-chain length polyhydroxyalkanoate biosynthesis genes in pseudomonads. *Biotechnol. Lett.* **27**, 279 (2005).

8. Y. Kim *et al.*, Real-Time Analysis of Enzymatic Surface-Initiated Polymerization Using Surface Plasmon Resonance (SPR). *Macromol. Biosci.* **6**, 145 (2006).

9. K. Kuchta, L. Chi, H. Fuchs, M. Potter, A. Steinbuchel, Studies on the Influence of Phasins on Accumulation and Degradation of PHB and Nanostructure of PHB Granules in Ralstonia eutropha H16. *Biomacromolecules* **8**, 657 (2007).

10. J. T. Ou, R. L. Reim, F- mating materials able to generate a mating signal in mating with HfrH dnaB(Ts) cells. *J. Bacteriol.* **133**, 442 (January 1, 1978, 1978).

11. A. M. Dai Gao, Tsuneo Yamane, Shunsaku Ueda, Identification of the intracellular polyhydroxyalkanoate depolymerase gene of Paracoccus denitrificans and some properties of the gene product. *FEMS Microbiol. Lett.* **196**, 159 (2001).

12. R. Handrick, S. Reinhardt, D. Jendrossek, Mobilization of Poly(3-Hydroxybutyrate) in Ralstonia eutropha. *J. Bacteriol.* **182**, 5916 (October 15, 2000, 2000).

13. L. L. Madison, G. W. Huisman, Metabolic Engineering of Poly(3-Hydroxyalkanoates): From DNA to Plastic. *Microbiol. Mol. Biol. Rev.* **63**, 21 (March 1, 1999, 1999).

14. J. Stubbe, J. Tian, Polyhydroxyalkanoate (PHA) homeostasis: the role of the PHA synthase. *Nat. Prod. Rep.* **20**, 445 (2003).

15. K. Grage *et al.*, Bacterial Polyhydroxyalkanoate Granules: Biogenesis, Structure, and Potential Use as Nano-/Micro-Beads in Biotechnological and Biomedical Applications. *Biomacromolecules* **10**, 660 (2009).

16. M. Potter, A. Steinbuchel, Poly(3-hydroxybutyrate) Granule-Associated Proteins: Impacts on Poly(3-hydroxybutyrate) Synthesis and Degradation&#x2020. *Biomacromolecules* **6**, 552 (2005).

17. A. Steinbuchel, H. E. Valentin, Diversity of bacterial polyhydroxyalkanoic acids. *FEMS Microbiol. Lett.* **128**, 219 (1995).

18. Y. Poirier, C. Nawrath, C. Somerville, Production Of Polyhydroxyalkanoates, A Family Of Biodegradable Plastics And Elastomers, In Bacteria And Plants. *Bio-Technology* **13**, 142 (Feb, 1995).

19. T. U. Gerngross, D. P. Martin, Enzyme-catalyzed synthesis of poly[(R)-(-)-3-hydroxybutyrate]: formation of macroscopic granules in vitro. *Proc. Natl. Acad. Sci. U. S. A.* **92**, 6279 (1995).

20. X. H. Zou, G. Q. Chen, Metabolic engineering for microbial production and applications of copolyesters consisting of 3-hydroxybutyrate and medium-chain-length 3-hydroxyalkanoates. *Macromol. Biosci.* **7**, 174 (Feb, 2007).

21. I. S. Aldor, J. D. Keasling, Process design for microbial plastic factories: metabolic engineering of polyhydroxyalkanoates. *Curr. Opin. Biotechnol.* **14**, 475 (2003).

22. R. Bhatt, D. Shah, K. C. Patel, U. Trivedi. (Elsevier Sci Ltd, 2008), pp. 4615-4620.

23. E. V. D. Gomes, C. M. F. Oliveira, M. L. Dias, Blends of Poly(Hydroxybutyrate) and Oligomeric Polyester. *Int. J. Polym. Anal. Charact.* **14**, 68 (2009).

24. J. Ziegler, in *Bloomberg.com*. (2009).

25. J. C. Knowles, G. W. Hastings, In vitro degradation of a phb/phv copolymer and a new technique for monitoring early surface changes. *Biomaterials* **12**, 210 (1991).

26. D. Behrend, Michalik, I., Kramp, B., Haubold, A,, and Schmitz, K. P., in *23rd Meeting of rhe Society for Biomaterials*. (New Orleans, LA, 1997).

27. G. A. R. Nobes, R. H. Marchessault, D. Maysinger, Polyhydroxyalkanoates: Materials for delivery systems. *Drug Deliv.* **5**, 167 (1998).

28. G. L. S. Pawan, S. J. G. Semple, Effect of 3-hydroxybutyrate in obese subjects on very-low-energy diets and during therapeutic starvation. *Lancet* **i**, 15 (1983).

29. R. N. Reusch, A. W. Sparrow, J. Gardiner, Transport of poly-beta-hydroxybutyrate in human plasma. *Biochim. Biophys. Acta* **1123**, 33 (Jan, 1992).

30. C. Doyle, E. T. Tanner, W. Bonfield, In vitro and in vivo evaluation of polyhydroxybutyrate and of polyhydroxybutyrate reinforced with hydroxyapatite. *Biomaterials* **12**, 841 (Nov, 1991).

31. S. Gogolewski, M. Jovanovic, S. M. Perren, J. G. Dillon, M. K. Hughes, Tissue-response and in-vivo degradation of selected polyhydroxyacids - polylactides (pla), poly(3-hydroxybutyrate) (phb), and poly(3-hydroxybutyrate-co-3-hydroxyvalerate) (phb/va). *J. Biomed. Mater. Res.* **27**, 1135 (Sep, 1993).

32. E. I. Shishatskaya, T. G. Volova, A comparative investigation of biodegradable polyhydroxyalkanoate films as matrices for in vitro cell cultures. *Journal of Materials Science-Materials in Medicine* **15**, 915 (Aug, 2004).

33. N. Niamsiri, Cornell University (2007).

34. D. P. Martin, S. F. Williams, Medical applications of poly-4-hydroxybutyrate: a strong flexible absorbable biomaterial. *Biochem. Eng. J.* **16**, 97 (2003).

35. D. P. Martin. (National Institute of Biomedical Imaging and Biomedical Engineering, 2007).

36. T. U. G. D. W. W. Mahmoud Reza Banki, Novel and economical purification of recombinant proteins: Intein-mediated protein purification using in vivo polyhydroxybutyrate (PHB) matrix association. *Protein Science* **14**, 1387 (2005).

37. G. C. Barnard, J. D. McCool, D. W. Wood, T. U. Gerngross, Integrated Recombinant Protein Expression and Purification Platform Based on Ralstonia eutropha. *Appl. Environ. Microbiol.* **71**, 5735 (October 1, 2005, 2005).

38. J. Atwood, B. Rehm, Protein engineering towards biotechnological production of bifunctional polyester beads. *Biotechnol. Lett.* **31**, 131 (2009).

39. V. Peters, B. H. A. Rehm, In vivo monitoring of PHA granule formation using GFP-labeled PHA synthases. *FEMS Microbiol. Lett.* **248**, 93 (2005).

40. V. Peters, B. H. A. Rehm, In Vivo Enzyme Immobilization by Use of Engineered Polyhydroxyalkanoate Synthase. *Appl. Environ. Microbiol.* **72**, 1777 (March 1, 2006, 2006).

41. V. Peters, B. H. A. Rehm, Protein engineering of streptavidin for in vivo assembly of streptavidin beads. *J. Biotechnol.* **134**, 266 (2008).

42. J. A. Brockelbank, V. Peters, B. H. A. Rehm, Recombinant Escherichia coli Strain Produces a ZZ Domain Displaying Biopolyester Granules Suitable for Immunoglobulin G Purification. *Appl. Environ. Microbiol.* **72**, 7394 (November 1, 2006, 2006).

43. K. Grage, B. H. A. Rehm, In Vivo Production of scFv-Displaying Biopolymer Beads Using a Self-Assembly-Promoting Fusion Partner. *Bioconj. Chem.* **19**, 254 (2008).

44. B. T. Backstrom, J. Brockelbank, B. Rehm, Recombinant Escherichia coli produces tailor-made biopolyester granules for applications in fluorescence activated cell sorting: functional display of the mouse interleukin-2 and myelin oligodendrocyte glycoprotein. *BMC Biotechnol.* **7**, 3 (2007).

45. A. C. Jahns, R. G. Haverkamp, B. H. A. Rehm, Multifunctional Inorganic-Binding Beads Self-Assembled Inside Engineered Bacteria. *Bioconj. Chem.* **19**, 2072 (2008).

46. Z. W. Wang, H.;Chen, J.; Zhang, J.; Yao, Y.; Chen, G. , A novel self-cleaving phasin tag for purification of recombinant proteins based on hydrophobic polyhydroxyalkanoate nanoparticles. *Lab Chip* **8**, 1957 (2008).

47. C. Moldes, P. Garcia, J. L. Garcia, M. A. Prieto, In Vivo Immobilization of Fusion Proteins on Bioplastics by the Novel Tag BioF. *Appl. Environ. Microbiol.* **70**, 3205 (June 1, 2004, 2004).

48. S. J. Lee *et al.*, Selective Immobilization of Fusion Proteins on Poly(hydroxyalkanoate) Microbeads. *Anal. Chem.* **77**, 5755 (2005).

49. J. Ihssen, D. Magnani, L. ThoÌˆny-Meyer, Q. Ren, Use of Extracellular Medium Chain Length Polyhydroxyalkanoate Depolymerase for Targeted Binding of Proteins to Artificial Poly[(3-hydroxyoctanoate)-co-(3-hydroxyhexanoate)] Granules. *Biomacromolecules* **0**.

50. J. Sparks, C. Scholz, Synthesis and Characterization of a Cationic Poly(β-hydroxyalkanoate). *Biomacromolecules* **9**, 2091 (2008).

51. J. Sparks, C. Scholz, Evaluation of a Cationic Poly(β-hydroxyalkanoate) as a Plasmid DNA Delivery System. *Biomacromolecules* **10**, 1715 (2009).

52. J. L. Han-Nah Kim, Hae-Yeong Kim and Young-Rok Kim, Enzymatic synthesis of a drug delivery system based on polyhydroxyalkanoate-protein block copolymers. *Chem. Commun.*, 7104 (2009).

53. J. Lee *et al.*, Tumor-specific hybrid polyhydroxybutyrate nanoparticle: Surface modification of nanoparticle by enzymatically synthesized functional block copolymer. *Bioorganic & Medicinal Chemistry Letters* **21**, 2941 (2011).

54. L. Neumann *et al.*, Binding of the Major Phasin, PhaP1, from Ralstonia eutropha H16 to Poly(3-Hydroxybutyrate) Granules. *J. Bacteriol.* **190**, 2911 (April 15, 2008, 2008).

55. R. N. Reusch, Low-molecular-weight complexed poly(3-hydroxybutyrate) - a dynamic and versatile molecule in-vivo. *Can. J. Microbiol.* **41**, 50 (1995).

56. J. L. Maia, M. H. A. Santana, M. I. Ré, The effect of some processing conditions on the characteristics of biodegradable microspheres obtained by an emulsion solvent evaporation process. *Brazilian Journal of Chemical Engineering* **21**, 01 (2004).

57. C. Errico, C. Bartoli, F. Chiellini, E. Chiellini, Poly(hydroxyalkanoates)-Based Polymeric Nanoparticles for Drug Delivery. *Journal of Biomedicine & Biotechnology*, Article No.: 571702 (2009).

58. M.-C. Bissery, Valeriote, E, and Thies, C., in *Microspheres and drug therapy: Pharmaceutical, immunological and medical aspects,* L. I. S. S. Davis, J. G. McVie, and E. Tomlinson, Ed. (Elsevier Science, New York, 1984), pp. 217-227.

59. K. Juni, M. Nakano, M. Kubota, Controlled release of aclarubicin an anticancer antibiotic from poly-beta-hydroxybutyric-acid microspheres. *J. Controlled Release* **4**, 25 (1986).

60. T. Kawaguchi *et al.*, Control of drug release with a combination of prodrug and polymer matrix - antitumor-activity and release profiles of 2',3'-diacyl-5-fluoro-2'-deoxyuridine from poly(3-hydroxybutyrate) microspheres. *J. Pharm. Sci.* **81**, 508 (1992).

61. N. Gangrade, J. C. Price, Poly(hydroxybutyrate-hydroxyvalerate) microspheres containing progesterone - preparation, morphology and release properties. *J. Microencaps.* **8**, 185 (1991).

62. M. R. Brophy, P. B. Deasy, Invitro and invivo studies on biodegradable polyester microparticles containing sulfamethizole. *Int. J. Pharm.* **29**, 223 (1986).

63. R. H. Marchessault, D. Maysinger, G. A. R. Nobes. (McGill University (Montreal, CA), USA, 1998).

64. I. Gursel, V. Hasirci, Properties and drug release behaviour of poly(3-hydroxybutyric acid) and various poly(3-hydroxybutyrate-hydroxyvalerate) copolymer microcapsules. *J. Microencaps.* **12**, 185 (1995).

65. A. Omri, M. Ravaoarinoro, M. Poisson, Incorporation, release and in-vitro antibacterial activity of liposomal aminoglycosides against pseudomonas-aeruginosa. *J. Antimicrob. Chemother.* **36**, 631 (1995).

66. H. Abe, Y. Doi, Y. Yamamoto, Controlled release of lastet, an anticancer drug, from poly(3-hydroxybutyrate) microspheres containing acylglycerols. *Journal of Macromolecular Science-Pure and Applied Chemistry* **29**, 229 (1992).

67. J. H. Eldridge *et al.*, Controlled vaccine release in the gut-associated lymphoid-tissues.1: Orally-administered biodegradable microspheres target the peyers patches. *J. Controlled Release* **11**, 205 (1990).

68. I. Guersel, V. Hasirci, Properties and drug release behaviour of poly(3-hydroxybutyric acid) and various poly(3-hydroxybutyrate-hydroxyvalerate) copolymer microcapsules. *J. Microencaps.* **12**, 185 (1995).

69. Y. P. Kim, H.; Ober, C. K.; Coates, G. W.; Batt, C. A., Enzymatic surface-initiated polymerization: A novel approach for the in situ solid-phase synthesis of biocompatible polymer poly(3-hydroxybutyrate). *Biomacromolecules* **5**, 889 (2004).

70. Y.-R. Kim, Paik, H-j, Ober, CK, Batt, CA., Enzymatic Surface-initiated Polymerization Of 3-(r)-hydroxybutyryl-coenzyme A: Surface Modification Of A Solid Substrate With A Biodegradable And Biocompatible Polymer: Poly(3-hydroxybutyrate). *Polym. Prepr.* **43**, 706 (2002).

71. Y.-R. Kim, H.-j. Paik, C. K. Ober, G. W. Coates, C. A. Batt, Enzymatic surface-initiated polymerization of 3-(R)-hydroxybutyryl-CoA: Surface modification of a solid substrate with a biodegradable and biocompatible polymer. *Abstracts of Papers American Chemical Society* **223**, POLY 231 (2002, 2002).

72. N. Niamsiri *et al.*, Insight in the role of bovine serum albumin for promoting the in situ surface growth of polyhydroxybutyrate (PHB) on patterned surfaces via enzymatic surface-initiated polymerization. *Colloids and Surfaces B-Biointerfaces* **60**, 68 (Oct, 2007).

73. H. J. Paik *et al.*, End-functionalization of poly(3-hydroxybutyrate) via genetic engineering for solid surface modification. *Chem. Commun.*, 1956 (Apr, 2005).

74. A. D. Elster, *Magnetic Resonance Imaging*. F. R. J., Ed., (S. Louis, 1994).

75. E. A. Waters, S. A. Wickline, Contrast agents for MRI. *Basic Res. Cardiol.* **103**, 114 (2008).

76. H. Z. S Sun, Size-Controlled Synthesis of Magnetite Nanoparticles. *J. Am. Chem. Soc.* **124**, 8204 (2002).

77. K. Kneipp, H. Kneipp, I. Itzkan, R. R. Dasari, M. S. Feld, Ultrasensitive chemical analysis by Raman spectroscopy. *Chem. Rev.* **99**, 2957 (Oct, 1999).

78. P. J. H. a. A. J. M. Martin Fleischmann, Raman spectra from electrode surfaces. *J. Chem. Soc., Chem. Commun.*, 80 (1973).

79. G. Braun *et al.*, Chemically patterned microspheres for controlled nanoparticle assembly in the construction of SERS hot spots. *J. Am. Chem. Soc.* **129**, 7760 (Jun, 2007).

80. S. Basu, S. Pande, S. Jana, S. Bolisetty, T. Pal, Controlled interparticle spacing for surface-modified gold nanoparticle aggregates. *Langmuir* **24**, 5562 (May, 2008).

81. P. K. Jain, K. S. Lee, I. H. El-Sayed, M. A. El-Sayed, Calculated Absorption and Scattering Properties of Gold Nanoparticles of Different Size, Shape, and Composition:â€‰ Applications in Biological Imaging and Biomedicine. *The Journal of Physical Chemistry B* **110**, 7238 (2006).

82. J. Kummerlen, A. Leitner, H. Brunner, F. R. Aussenegg, A. Wokaun, Enhanced Dye Fluorescence Over Silver Island Films - Analysis Of The Distance Dependence. *Mol. Phys.* **80**, 1031 (Dec, 1993).

83. A. M. Glass, P. F. Liao, J. G. Bergman, D. H. Olson, Interaction Of Metal Particles With Absorbed Dye Molecules - Absorption And Luminescence. *Opt. Lett.* **5**, 368 (1980).

84. A. Campion, A. R. Gallo, C. B. Harris, H. J. Robota, P. M. Whitmore, Electronic-energy Transfer To Metal-surfaces - A Test Of Classical Image Dipole Theory At Short Distances. *Chem. Phys. Lett.* **73**, 447 (1980).

85. K. Sokolov, G. Chumanov, T. M. Cotton, Enhancement of molecular fluorescence near the surface of colloidal metal films. *Anal. Chem.* **70**, 3898 (Sep, 1998).

86. T. Hayakawa, S. T. Selvan, M. Nogami, Field enhancement effect of small Ag particles on the fluorescence from Eu3+-doped SiO2 glass. *Appl. Phys. Lett.* **74**, 1513 (Mar, 1999).

87. S. T. Selvan, T. Hayakawa, M. Nogami, Remarkable influence of silver islands on the enhancement of fluorescence from Eu3+ ion-doped silica gels. *J. Phys. Chem. B* **103**, 7064 (Aug, 1999).

88. J. R. Lakowicz, Radiative decay engineering: Biophysical and biomedical applications. *Anal. Biochem.* **298**, 1 (Nov, 2001).

89. P. K. Jain, X. Huang, I. H. El-Sayed, M. A. El-Sayed, Noble Metals on the Nanoscale: Optical and Photothermal Properties and Some Applications in Imaging, Sensing, Biology, and Medicine. *Acc. Chem. Res.* **41**, 1578 (2008).

90. M. A. El-Sayed, Some Interesting Properties of Metals Confined in Time and Nanometer Space of Different Shapes. *Acc. Chem. Res.* **34**, 257 (2001).

91. S. Link, M. A. El-Sayed, Spectral Properties and Relaxation Dynamics of Surface Plasmon Electronic Oscillations in Gold and Silver Nanodots and Nanorods. *The Journal of Physical Chemistry B* **103**, 8410 (1999).

92. S. Link, M. A. El-Sayed, Shape and size dependence of radiative, non-radiative and photothermal properties of gold nanocrystals. *Int. Rev. Phys. Chem.* **19**, 409 (2000).

93. S. Link, M. A. El-Sayed, Optical properties and ultrafast dynamics of metallic nanocrystals. *Annu. Rev. Phys. Chem.* **54**, 331 (2003).

94. P. Jain, X. Huang, I. El-Sayed, M. El-Sayed, Review of Some Interesting Surface Plasmon Resonance-enhanced Properties of Noble Metal

Nanoparticles and Their Applications to Biosystems. *Plasmonics* **2**, 107 (2007).

95. D. P. O'Neal, L. R. Hirsch, N. J. Halas, J. D. Payne, J. L. West, Photo-thermal tumor ablation in mice using near infrared-absorbing nanoparticles. *Cancer Lett.* **209**, 171 (2004).

96. K. König, Multiphoton microscopy in life sciences. *J. Microsc.* **200**, 83 (2000).

97. C. R. Simpson, et al., Near-infrared optical properties of ex vivo human skin and subcutaneous tissues measured using the Monte Carlo inversion technique. *Phys. Med. Biol.* **43**, 2465 (1998).

98. D. S. EJ Simon, The Preparation of S-Succinyl Coenzyme A. *J. Am. Chem. Soc.* **72**, 2520 (1953).

99. S. Z. JJ Song, RW Lenz, S Goodwin, In Vitro Polymerization and Copolymerization of 3-Hydroxypropionyl-CoA with the PHB Synthase from Ralstonia eutropha. *Biomacromolecules* **1**, 433 (2000).

100. P. d. l. Presa, M. Multigner, J. d. l. Venta, M. A. Garcia, M. L. Ruiz-Gonzalez, Structural and magnetic characterization of oleic acid and oleylamine-capped gold nanoparticles. *J. Appl. Phys.* **100**, 123915 (2006).

101. P. S. B Dubertret, DJ Norris, V Noireaux, AH Brivanlou, A Libchaber, In Vivo Imaging of Quantum Dots Encapsulated in Phospholipid Micelles. *Science* **298**, 1759 (2002).

102. H. Shimazaki. (2010), pp. Online tool that generates an optmized histogram of input data.

103. R. P. Huang, R. N. Reusch, Poly(3-hydroxybutyrate) is associated with specific proteins in the cytoplasm and membranes of Escherichia coli. *J. Biol. Chem.* **271**, 22196 (1996).

104. B. H. A. Rehm, Polyester synthases: natural catalysts for plastics. *Biochem. J.* **376**, 15 (2003).

105. M. Banki, T. Gerngross, D. Wood, Novel and economical purification of recombinant proteins: Intein-mediated protein purification using in vivo polyhydroxybutyrate (PHB) matrix association. *Protein Sci.* **14**, 1387 (2005).

106. R. Jossek, R. Reichelt, A. Steinbüchel, In vitro biosynthesis of poly(3-hydroxybutyric acid) by using purified poly(hydroxyalkanoic acid) synthase of Chromatium vinosum. *Appl. Microbiol. Biotechnol.* **49**, 258 (1998).

107. J. S. Weinstein *et al.*, Superparamagnetic iron oxide nanoparticles: diagnostic magnetic resonance imaging and potential therapeutic applications in neurooncology and central nervous system inflammatory pathologies, a review. *J. Cereb. Blood Flow Metab.* **30**, 15 (2010).

108. M. H. M. Dias, C. L. Paul, Ferromagnetic particles as contrast agents for magnetic resonance imaging of liver and spleen. *Magn. Reson. Med.* **3**, 328 (1986).

109. F. R. Perry, S. O. Charles, C. M. Alan, G. F. Terrence, S. L. John, Jr., Ferromagnetic contrast agents: A new approach. *Magn. Reson. Med.* **3**, 217 (1986).

110. A. Hemmingsson *et al.*, Relaxation enhancement of the dog liver and spleen by biodegradable superparamagnetic particles in proton magnetic-resonance imaging. *Acta Radiol.* **28**, 703 (1987).

111. S. Saini *et al.*, Ferrite particles - a superparamagnetic mr contrast agent for enhanced detection of liver-carcinoma. *Radiology* **162**, 217 (1987).

112. Y. X. J. Wang, S. M. Hussain, G. P. Krestin, Superparamagnetic iron oxide contrast agents: physicochemical characteristics and applications in MR imaging. *Eur. Radiol.* **11**, 2319 (2001).

113. R. Weissleder, A. Bogdanov, E. A. Neuwelt, M. Papisov, Long-circulating iron-oxides for mr-imaging. *Adv. Drug Del. Rev.* **16**, 321 (1995).

114. R. W. a. M. Papisov, Pharmaceutical iron oxides for MR imaging. *Rev. Magn. Reson. Med* **4**, 1 (1993).

115. N. Butoescu *et al.*, Dexamethasone-containing biodegradable superparamagnetic microparticles for intra-articular administration: Physicochemical and magnetic properties, in vitro and in vivo drug release. *Eur. J. Pharm. Biopharm.* **72**, 529 (2009).

116. K. M. Bennett, E. M. Shapiro, C. H. Sotak, A. P. Koretsky, Controlled aggregation of ferritin to modulate MRI relaxivity. *Biophys. J.* **95**, 342 (Jul, 2008).

117. E. R. Cintra *et al.*, Nanoparticle agglomerates in magnetoliposomes. *Nanotechnology* **20**, 45103 (2009).

118. B. A. Larsen, M. A. Haag, N. J. Serkova, K. R. Shroyer, C. R. Stoldt, Controlled aggregation of superparamagnetic iron oxide nanoparticles for the development of molecular magnetic resonance imaging probes. *Nanotechnology* **19**, 7 (Jul, 2008).

119. B. A. Moffat *et al.*, A novel polyacrylamide magnetic nanoparticle contrast agent for molecular imaging using MRI. *Mol Imaging* **2**, 324 (2003).

120. J. F. Berret *et al.*, Controlled clustering of superparamagnetic nanoparticles using block copolymers: Design of new contrast agents for magnetic resonance imaging. *J. Am. Chem. Soc.* **128**, 1755 (2006).

121. N. Janaky, et al., Determination of agarose gel pore size: Absorbance measurements vis a vis other techniques. *Journal of Physics: Conference Series* **28**, 83 (2006).

122. M. Rustem. (2000).

123. M. A. Rutzke, in *Pittsburgh Conference*. (Orlando Florida, 1999).

124. M. A. Rutzke, in *24th Annual Conference of the Federation of Analytical Chemistry and Spectroscopy Societies*. (Providence, Rhode Island, 1997).

125. M. A. Rutzke, Cornell University (2002).

126. J. R. Casleysmith, Functional fine-structure. *Experientia* **32**, 818 (1976).

127. FDA Approved SPIO Contrast Agents

Feridex®/Endorem™ - Dextran-coated iron oxide nanoparticles (~50nm),
Relaxivity: 160 mmol l-1 s-1
Developed by: AMAG Pharmaceuticals, Inc.
Approved and for sale in the US by Bayer HealthCare Pharmaceuticals

GastroMARK®/Lumirem® - Silicon coated iron oxide nanoparticles (~50nm),
Relaxivity: 3.8 mmol l-1 s-1
Developed by: AMAG Pharmaceuticals, Inc. and Guerbet S.A.
Approved and for sale in the US by Mallinckrodt Inc.

Resovist® - carboxydextran coated iron oxide nanoparticles (~50nm),
Relaxivity: 151 mmol l-1 s-1
Developed by: Bayer Schering Pharma AG
In Phase III Clinical Trials in the US, Approved and for sale in Europe by Bayer Schering Pharma AG.

128. Y. Matsumoto, A. Jasanoff, T-2 relaxation induced by clusters of superparamagnetic nanoparticles: Monte Carlo simulations. *Magn. Reson. Imaging* **26**, 994 (2008).

129. A. Schlachter, M. E. Gruner, M. Spasova, M. Farle, P. Entel, Preparation and properties of nanostructured magnetic hollow microspheres: experiment and simulation. *Phase Transitions* **78**, 741 (2005).

130. S. Lecommandoux, O. Sandre, F. Checot, R. Perzynski, Smart hybrid magnetic self-assembled micelles and hollow capsules. *Prog. Solid State Chem.* **34**, 171 (2006).

131. C. Y. Wang, C. J. Zhang, Y. Li, Y. H. Chen, Z. Tong, Facile fabrication of nanocomposite microspheres with polymer cores and magnetic shells by Pickering suspension polymerization. *Reactive & Functional Polymers* **69**, 750 (2009).

132. E. L. Bizdoaca, M. Spasova, M. Farle, M. Hilgendorff, F. Caruso, Magnetically directed self-assembly of submicron spheres with a Fe3O4 nanoparticle shell. *J. Magn. Magn. Mater.* **240**, 44 (2002).

133. L. Jurasek, R. H. Marchessault, Polyhydroxyalkanoate (PHA) granule formation in Ralstonia eutropha cells: a computer simulation. *Appl. Microbiol. Biotechnol.* **64**, 611 (2004).

134. M.-C. Seo, H.-D. Shin, Y.-H. Lee, Transcription level of granule-associated phaP and phaR genes and granular morphogenesis of poly-β-hydroxyalkanoate granules in Ralstonia eutropha. *Biotechnol. Lett.* **26**, 617 (2004).

135. U. Pieperfurst, M. H. Madkour, F. Mayer, A. Steinbuchel, Identification of the region of a 14-kilodalton protein of rhodococcus ruber that is responsible for the binding of this phasin to polyhydroxyalkanoic acid granules. *J. Bacteriol.* **177**, 2513 (1995).

136. D. Schultheiss, R. Handrick, D. Jendrossek, M. Hanzlik, D. Schuler, The presumptive magnetosome protein Mms16 is a poly(3-hydroxybutyrate)

granule-bound protein (phasin) in Magnetospirillum gyphiswaldense. *J. Bacteriol.* **187**, 2416 (2005).

137. M. Poetter, M. H. Madkour, F. Mayer, A. Steinbuechel, Regulation of phasin expression and polyhydroxyalkanoate (PHA) granule formation in Ralstonia eutropha H16. *Microbiology (Reading)* **148**, 2413 (2002).

138. R. Wieczorek, A. Pries, A. Steinbuchel, F. Mayer, Analysis of a 24-kilodalton protein associated with the polyhydroxyalkanoic acid granules in alcaligenes-eutrophus. *J. Bacteriol.* **177**, 2425 (1995).

139. E. Shishatskaya, O. Voinova, A. Goreva, O. Mogilnaya, T. Volova, Biocompatibility of polyhydroxybutyrate microspheres: in vitro and in vivo evaluation. *J. Mater. Sci. Mater. Med.* **19**, 2493 (2008).

140. in *Joint FAO/WHO Expert Committee on Food Additives*. (World Health Organization, 1974), vol. WHO Food Additives Series No. 5.

141. M. T. Peracchia *et al.*, Visualization of in vitro protein-rejecting properties of PEGylated stealth® polycyanoacrylate nanoparticles. *Biomaterials* **20**, 1269 (1999).

142. R. Gref *et al.*, `Stealth' corona-core nanoparticles surface modified by polyethylene glycol (PEG): influences of the corona (PEG chain length and surface density) and of the core composition on phagocytic uptake and plasma protein adsorption. *Colloids Surf. B. Biointerfaces* **18**, 301 (2000).

143. M. D. Scott, K. L. Murad, Cellular camouflage: Fooling the immune system with polymers. *Curr. Pharm. Des.* **4**, 423 (1998).

144. C. Fang *et al.*, In vivo tumor targeting of tumor necrosis factor-[alpha]-loaded stealth nanoparticles: Effect of MePEG molecular weight and particle size. *Eur. J. Pharm. Sci.* **27**, 27 (2006).

145. F. Alexis, E. Pridgen, L. K. Molnar, O. C. Farokhzad, Factors Affecting the Clearance and Biodistribution of Polymeric Nanoparticles. *Mol. Pharm.* **5**, 505 (2008).

146. M. Longmire, P. L. Choyke, H. Kobayashi, Clearance properties of nano-sized particles and molecules as imaging agents: considerations and caveats. *Nanomedicine* **3**, 703 (2008).

147. P. Rubin, S. H. Levitt, The response of disseminated reticulum cell sarcoma to the intravenous injection of colloidal radioactive gold. *J. Nucl. Med.* **5**, 581 (1964).

148. S. W. Root, G. A. Andrews, R. M. Kniseley, M. P. Tyor, The distribution and radiation effects of intravenously administered colloidal au-198 in man. *Cancer* **7**, 856 (1954).

149. M. J. Hardonk, G. Harms, J. Koudstaal, Zonal heterogeneity of rat hepatocytes in the in vivo uptake of 17 nm colloidal gold granules. *Histochem. Cell Biol.* **83**, 473 (1985).

150. R. Guy, L. H. Robert, J. H. Richard, Hepatic metabolism of colloidal gold-low-density lipoprotein complexes in the rat: Evidence for bulk excretion of lysosomal contents into bile. *Hepatology* **9**, 380 (1989).

151. A. C. Powell, G. F. Paciotti, S. K. Libutti, in *Cancer Nanotechnology: Methods and Protocols*. (2010), vol. 624, pp. 375-384.

152. S. S. Agasti *et al.*, Nanoparticles for detection and diagnosis. *Adv. Drug Del. Rev.* **62**, 316 (2010).

153. J. Kneipp, H. Kneipp, B. Wittig, K. Kneipp, Novel optical nanosensors for probing and imaging live cells. *Nanomed. Nanotechnol. Biol. Med.* **6**, 214.

154. K. Kneipp, H. Kneipp, I. Itzkan, R. R. Dasari, M. S. Feld, Surface-enhanced Raman scattering and biophysics. *Journal of Physics-Condensed Matter* **14**, R597 (2002).

155. J. Kneipp, Nanosensors based on SERS for applications in living cells. *Surface-Enhanced Raman Scattering: Physics and Applications* **103**, 335 (2006).

156. K. Kneipp *et al.*, Surface-enhanced Raman Spectroscopy in single living cells using gold nanoparticles. *Appl. Spectrosc.* **56**, 150 (2002).

157. J. Kneipp, H. Kneipp, K. Kneipp, SERS-a single-molecule and nanoscale tool for bioanalytics. *Chem. Soc. Rev.* **37**, 1052 (2008).

158. W. R. Premasiri *et al.*, Characterization of the Surface Enhanced Raman Scattering (SERS) of Bacteria. *The Journal of Physical Chemistry B* **109**, 312 (2004).

159. J. Kneipp, H. Kneipp, W. L. Rice, K. Kneipp, Optical Probes for Biological Applications Based on Surface-Enhanced Raman Scattering from Indocyanine Green on Gold Nanoparticles. *Anal. Chem.* **77**, 2381 (2005).

160. I. Chourpa, F. H. Lei, P. Dubois, M. Manfait, G. D. Sockalingum, Intracellular applications of analytical SERS spectroscopy and multispectral imaging. *Chem. Soc. Rev.* **37**, 993 (2008).

161. S. Kim *et al.*, Near-infrared fluorescent type II quantum dots for sentinel lymph node mapping. *Nat Biotech* **22**, 93 (2004).

162. X. M. Qian *et al.*, In vivo tumor targeting and spectroscopic detection with surface-enhanced Raman nanoparticle tags. *Nat. Biotechnol.* **26**, 83 (2008).

163. J. Zhang, Y. Fu, D. Liang, R. Y. Zhao, J. R. Lakowicz, Fluorescent Avidin-Bound Silver Particle: A Strategy for Single Target Molecule Detection on a Cell Membrane. *Anal. Chem.* **81**, 883 (2008).

164. J. Zhang, Y. Fu, J. R. Lakowicz, Single Cell Fluorescence Imaging Using Metal Plasmon-Coupled Probe. *Bioconj. Chem.* **18**, 800 (2007).

165. J. Zhang *et al.*, Single-Cell Fluorescence Imaging Using Metal Plasmon-Coupled Probe 2: Single-Molecule Counting on Lifetime Image. *Nano Lett.* **8**, 1179 (2008).

166. E. G. Matveeva, Z. Gryczynski, J. R. Lakowicz, Myoglobin immunoassay based on metal particle-enhanced fluorescence. *J. Immunol. Methods* **302**, 26 (2005).

167. N. Lochner *et al.*, Silver nanoparticle enhanced immunoassays: one step real time kinetic assay for insulin in serum. *Eur. J. Pharm. Biopharm.* **56**, 469 (2003).

168. E. Matveeva, Z. Gryczynski, J. Malicka, I. Gryczynski, J. R. Lakowicz, Metal-enhanced fluorescence immunoassays using total internal reflection and silver island-coated surfaces. *Anal. Biochem.* **334**, 303 (2004).

169. S. Henryk *et al.*, A novel method for monitoring monoclonal antibody production during cell culture. *Biotechnol. Bioeng.* **100**, 448 (2008).

170. T. Yamaguchi, T. Kaya, H. Takei, Characterization of cap-shaped silver particles for surface-enhanced fluorescence effects. *Anal. Biochem.* **364**, 171 (2007).

171. R. Nooney *et al.*, Enhancing the analytical performance of immunoassays that employ metal-enhanced fluorescence. *Anal. Bioanal. Chem.* **396**, 1127.

172. E. B. Dickerson *et al.*, Gold nanorod assisted near-infrared plasmonic photothermal therapy (PPTT) of squamous cell carcinoma in mice. *Cancer Lett.* **269**, 57 (2008).

173. L. R. Hirsch *et al.*, Nanoshell-mediated near-infrared thermal therapy of tumors under magnetic resonance guidance. *Proc. Natl. Acad. Sci. U. S. A.* **100**, 13549 (2003).

174. X. Huang, P. Jain, I. El-Sayed, M. El-Sayed, Plasmonic photothermal therapy (PPTT) using gold nanoparticles. *Lasers in Medical Science* **23**, 217 (2008).

175. C. Loo, A. Lowery, N. Halas, J. West, R. Drezek, Immunotargeted Nanoshells for Integrated Cancer Imaging and Therapy. *Nano Lett.* **5**, 709 (2005).

176. J. R. Cole, N. A. Mirin, M. W. Knight, G. P. Goodrich, N. J. Halas, Photothermal Efficiencies of Nanoshells and Nanorods for Clinical Therapeutic Applications. *The Journal of Physical Chemistry C* **113**, 12090 (2009).

177. A. Rosenthal, J. J. Barry, R. Sahatjian. (Scimed Life Systems, Inc., 1995).

178. C. W. Pouton, S. Akhtar, Biosynthetic polyhydroxyalkanoates and their potential in drug delivery. *Adv. Drug Del. Rev.* **18**, 133 (Jan, 1996).

179. Y. C. Xiong, Y. C. Yao, X. Y. Zhan, G. Q. Chen, Application of Polyhydroxyalkanoates Nanoparticles as Intracellular Sustained Drug-Release Vectors. *Journal of Biomaterials Science-Polymer Edition* **21**, 127 (2010).

180. J. J. Hickman *et al.*, Selective Functionalization Of Gold Microstructures With Ferrocenyl Derivatives Via Reaction With Thiols Or Disulfides - Characterization By Electrochemistry And Auger-electron Spectroscopy. *J. Am. Chem. Soc.* **113**, 1128 (Feb, 1991).

181. Q. P. Dai, C. C. Xue, G. Xue, L. X. Jiang, Fourier-transform Surface-enhanced Raman-scattering Studies Of Molecular Self-assembly Of Disulfides On Metals And The Application In Adhesion Promotion. *J. Adhes. Sci. Technol.* **9**, 1465 (1995).

182. C. R. Simovski, Surface-enhanced Raman scattering from silica core particles covered with silver nanoparticles. *Physical Review B* **79**, 5 (Jun, 2009).

183. J. R. Lakowicz, *Principles of Fluorescence Spectroscopy*. (Springer Science+Business Media, LLC, New York, 2006).

184. S. Phadtare *et al.*, Direct assembly of gold nanoparticle "shells" on polyurethane microsphere "cores" and their application as enzyme immobilization templates. *Chem. Mater.* **15**, 1944 (2003).

185. T. Ji, Y. Avny, D. Davidov, Preparation and Optical Properties of Au-shell Submicron Polystyrene Particles. *Materials Research Society Symposium Proceedings* **636**, (2001).

186. S. Lal, S. E. Clare, N. J. Halas, Nanoshell-Enabled Photothermal Cancer Therapy: Impending Clinical Impact. *Acc. Chem. Res.* **41**, 1842 (2008).

187. D. K. Kirui, D. A. Rey, C. A. Batt, Gold hybrid nanoparticles for targeted phototherapy and cancer imaging. *Nanotechnology* **21**, 105105 (2010).

188. K. Kim, Y. M. Lee, H. B. Lee, K. S. Shin, Silver-Coated Silica Beads Applicable as Core Materials of Dual-Tagging Sensors Operating via SERS and MEF. *ACS Applied Materials & Interfaces*, (2009).

189. M. Geoffrey von *et al.*, SERS-Coded Gold Nanorods as a Multifunctional Platform for Densely Multiplexed Near-Infrared Imaging and Photothermal Heating. *Adv. Mater.* **21**, 3175 (2009).

190. M. Xiao *et al.*, Gold nanotags for combined multi-colored Raman spectroscopy and x-ray computed tomography. *Nanotechnology* **21**, 035101 (2010).

191. C. L. Zavaleta *et al.*, Multiplexed imaging of surface enhanced Raman scattering nanotags in living mice using noninvasive Raman spectroscopy. *Proc. Natl. Acad. Sci. U. S. A.* **106**, 13511 (2009).

192. E. Sadauskas *et al.*, Protracted elimination of gold nanoparticles from mouse liver. *Nanomed. Nanotechnol. Biol. Med.* **5**, 162 (2009).

193. O. Duvernoy, T. Malm, J. Ramstrom, S. Bowald, A biodegradable patch used as a pericardial substitute after cardiac-surgery - 6-month and 24-month evaluation with CT. *Thorac. Cardiovasc. Surg.* **43**, 271 (1995).

194. T. Malm, S. Bowald, A. Bylock, C. Busch, Prevention of postoperative pericardial adhesions by closure of the pericardium with absorbable polymer patches - an experimental-study. *J. Thorac. Cardiovasc. Surg.* **104**, 600 (1992).

195. D. P. Martin, F. Skraly, S. F. Williams. (Metabolix, Inc., 2004).

196. B. H. A. Rehm, Biogenesis of microbial polyhydroxyalkanoate granules: a platform technology for the production of tailor-made bioparticles. *Curr. Issues Mol. Biol.* **9**, 41 (2007).